Crustal Structure and Marine Gas Hydrate Studies near Vancouver Island using Seismic Tomography

by

Ranjan Kumar Dash

B.Sc., Ravenshaw College, Cuttack, India, 1998
M.Tech., Indian Institute of Technology, Roorkee, India 2001

A Dissertation Submitted in Partial Fulfillment of the
Requirements for the Degree of

DOCTOR OF PHILOSOPHY

in the

SCHOOL OF EARTH AND OCEAN SCIENCES

Crustal Structure and Marine Gas Hydrate Studies near Vancouver Island using Seismic Tomography

by

Ranjan Kumar Dash

B.Sc., Ravenshaw College, Cuttack, India, 1998
M.Tech., Indian Institute of Technology, Roorkee, India 2001

Supervisory Committee

Dr. George D. Spence, Supervisor (School of Earth and Ocean Sciences)

Dr. Roy D. Hyndman, Member (School of Earth and Ocean Sciences)

Dr. Stan E. Dosso, Member (School of Earth and Ocean Sciences)

Dr. Ian J. Walker, Outside Member (Department of Geography)

Dr. S. Kodaira, External Examiner (IFREE, JAMSTEC)

Supervisory Committee

Dr. George D. Spence, Supervisor (School of Earth and Ocean Sciences)

Dr. Roy D. Hyndman, Member (School of Earth and Ocean Sciences)

Dr. Stan E. Dosso, Member (School of Earth and Ocean Sciences)

Dr. Ian J. Walker, Outside Member (Department of Geography)

Dr. S. Kodaira, External Examiner (IFREE, JAMSTEC)

Abstract

This dissertation work applies seismic tomographic inversion methods to two different datasets - one to address the earthquake hazard within the Strait of Georgia and the other to estimate hydrate concentration and distribution in the continental slope off Vancouver Island. In the first part of the study, seismic refraction/wide-angle reflection data from onshore-offshore experiments in 1998 and 2002 were inverted for a smooth three-dimensional (3D) velocity structure down to depths of 6-7 km beneath the Strait of Georgia, a seismically active region where an earthquake swarm (with magnitude up to 5) occurred in 1995-1997. The objectives were to map structures that contribute to seismic hazard evaluation in the Georgia Basin. The main structural features obtained from the inversion are: a northeast-southwest trending hinge line at the location of the earthquake swarm, where the basin deepens rapidly to the southeast; a northwest-southeast trending

velocity discontinuity that correlates well with the surface expression of the shallow Outer Island fault; sediment thickening from north to south; and basement uplift at the San Juan Islands, possibly caused by a thrust fault.

In the second part of the dissertation, seismic single channel and wide-angle reflection data collected in September 2005 were analyzed for a 2D profile of ocean bottom seismometers (OBSs) on the continental slope region off Vancouver Island, near ODP Site 889 and IODP Site 1327. The objectives were to determine the shallow sediment velocity structure associated with marine gas hydrates and to estimate the hydrate concentration in the sediment pore space. Combined inversion of single channel and OBS data produced a P-wave velocity model down to the depth of the BSR at 230 m below seafloor. Strong attenuation of P-waves below the BSR indicates the presence of free gas. To investigate structures below the BSR, forward modelling of S-waves was carried out using the data from the OBS horizontal components. Both the P- and S-wave models match very well with the sonic log data from ODP Site 889 and IODP Site 1327. The increase in P-wave velocity of the hydrate bearing sediments relative to the background no-hydrate velocity was utilized to estimate the hydrate concentration by using a simple porosity-reduction equation. An average concentration of 15% was estimated from the P-wave velocity model.

Prestack depth migration was applied to the OBS data to image the structure along the 2D profile containing the OBSs. The primary and multiple arrivals were migrated separately. Conventional migration of the primary arrivals produced an image with a very narrow illumination and the shallow subsurface layers including the seabottom were not imaged. However, migration of the OBS multiples, using a mirror imaging technique, produced a continuous structural image of the subsurface including the shallowest layers. The lateral illumination is much wider with a quality comparable to that of vertical incidence reflection data.

Table of Contents

List of Tables

List of Figures

Acknowledgements

First of all, I would like to thank my supervisor Dr. George Spence for his generous support and wise guidance during this dissertation work. I am thankful to my committee members Dr. Roy Hyndman, Dr. Stan Dosso and Dr. Ian Walker for their helpful suggestions. Special thanks to Stan for many helpful discussions on inverse theory. I sincerely thank Tom Brocher for many helpful discussions on the Georgia Basin tomography project. I thank Kumar Ramachandran for explaining to me the technical details of the 3-D tomography code. I also thank Matrin Scherwath for his help during the initial days of my work. Thanks to the captain and the crew of C.C.G.S. J.P. Tully for their efforts in collecting excellent datasets.

A part of this work was done during my internship with CGGVeritas, Houston. Thanks to Ross Haacke for his brilliant ideas and efforts to initiate the project. I am grateful to Shuki Ronen for letting me work in his group and use the company resources. I thank Sergio Grion, Yi Wang, Mark Cartwright and Bruce Mattocks who willingly lent me their time and expertise throughout the project.

I would also like to thank my friends in E-Hut, especially Tao, Marc, Caroll and Iulia for the wonderful time in the Seismology lab. Finally, I want to thank my family for all their emotional support throughout this work.

To

My Mother

"We learn geology the morning after the earthquake"

Ralph Waldo Emerson
American Poet, Lecturer and Essayist
(1803-1882)

Chapter 1

Introduction

This dissertation presents analysis of seismic data from the Strait of Georgia and the continental slope offshore Vancouver Island to image the shallow crustal structure of Georgia Basin and the accretionary prism respectively. In the first part of the dissertation, tomographic inversion of two wide-angle seismic traveltime datasets is used to construct a seismic velocity model of Georgia Basin and to investigate the shallow crustal faults within the basin that may help in future hazard assessments. In the second part, wide-angle and normal-incidence seismic reflection data collected on the mid-continental slope offshore Vancouver Island are analyzed to determine the shallow sediment velocity structure associated with gas hydrates. Hydrate concentration within the sediments is estimated from the seismic velocity model and compared with downhole log interpretations from drilling sites adjacent to the seismic lines.

1.1 Motivation

Vancouver Island is situated over the Cascadia subduction zone, which is characterized by the subduction of the Juan de Fuca plate beneath the North American plate (Fig.

1.1). Active subduction of the oceanic Juan de Fuca plate produces earthquakes, making the Vancouver Island margin one of the most seismically active regions of Canada. The region experiences three distinct types of earthquakes with origins at different parts of the subduction zone: shallow, small to moderate mid-crustal earthquakes, which occur within the continental crust of the overriding North American plate; deeper earthquakes within the subducting plate; and large, megathrust earthquakes at the boundary between the subducting plate and the overriding plate (*Rogers* 1994, 1998, *Cassidy et al.* 2000). Of these, the shallow crustal earthquakes occur most frequently and are believed to be driven by a margin parallel, north-northwest oriented compressive stress (*Rogers* 1994, *Mazzotti et al.* 2002, 2003). Within Georgia Basin, numerous small to moderate earthquakes have occurred in close proximity to the urban population centres of Vancouver, Victoria and Seattle (Fig. 1.2). Beneath the Strait of Georgia recent examples include events (*e.g.,* M = 4.6 in 1997 and M = 5 in 1975) located 30 km west of Vancouver. However, for many such events within the basin there is no obvious correlation with the mapped crustal faults. Moreover, if the seismic statistics of the adjoining areas (*e.g.,* M = 6.7 in 2001 in Puget Sound) are taken into account, the possibility of a bigger earthquake within Georgia Basin cannot be ruled out and yet the response of the basin to a major earthquake remains largely unknown. To identify potential geohazards and to refine assessments of potential earthquake ground surface response, a detailed structural map of the basin is necessary. To address this objective, the first part of this dissertation presents the interpretation of two seismic wide-angle experiments carried out in the Strait of Georgia and the surrounding areas - the 1998 Seismic Hazards Investigation in Puget Sound (SHIPS) and the 2002 Georgia Basin Geohazards Initiative (GBGI).

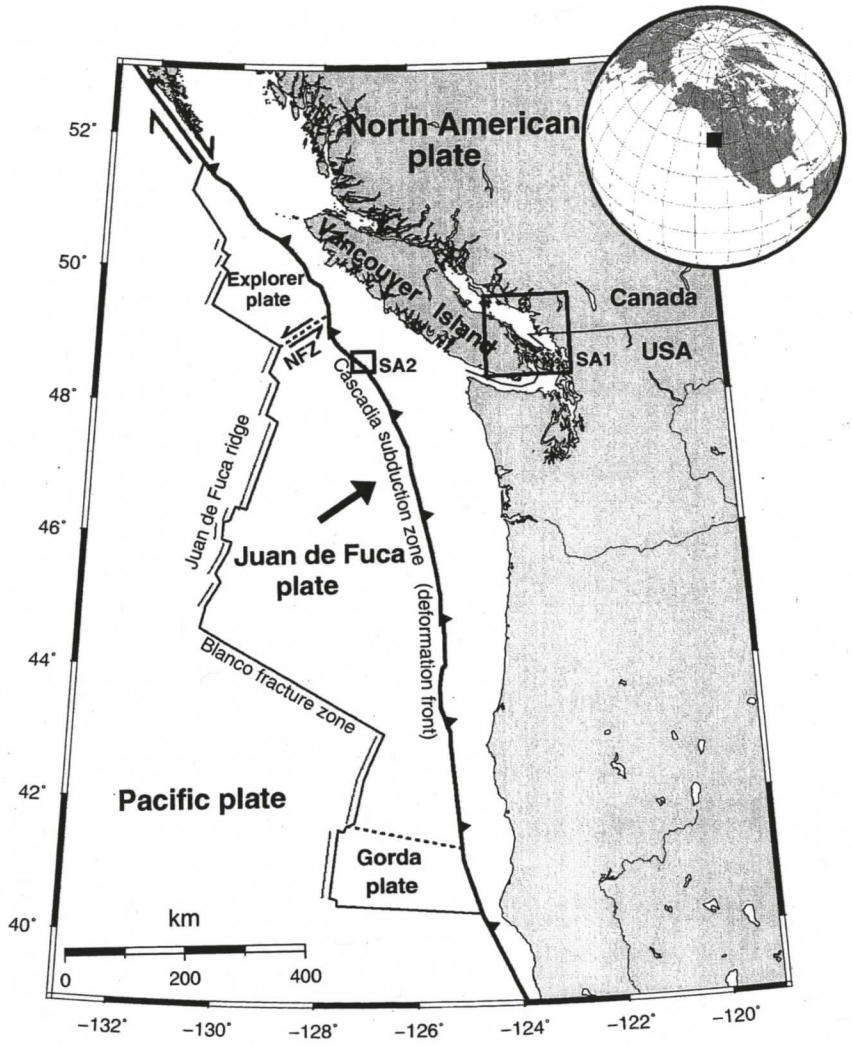

Figure 1.1: Tectonic setting of western North America. Boxes SA1 and SA2 are the study areas investigated in this study. NFZ: Nootka fracture zone.

Offshore Vancouver Island, subduction of the young Juan de Fuca plate has produced a large accretionary prism on the continental slope. The prism has been formed from the off-scraping and accretion of the incoming oceanic sediments at the deformation front (*Hyndman et al.* 2001). The prism sediments contain widespread gas hydrates down to depths of several hundred meters below the seafloor. Gas hydrates are naturally occurring ice-like crystals that are increasingly being studied due to their potential as a future energy resource, their effect on seafloor stability and their involvement in global climate

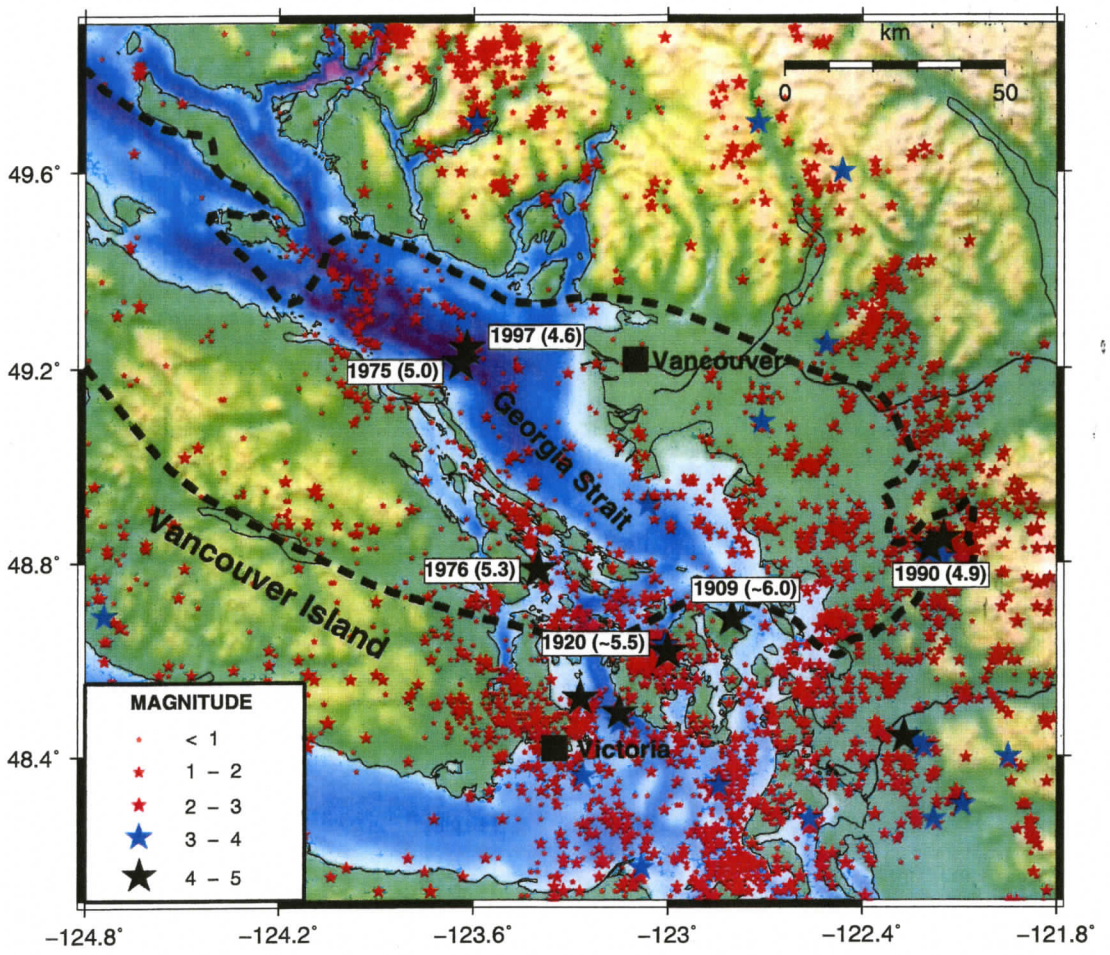

Figure 1.2: Seismicity within Georgia Basin and adjacent areas from 1985-2005 (*Courtesy*: Geological Survey of Canada catalogue). Other historic big earthquakes are also shown. The heavy dashed line outlines the boundary of the Georgia Basin.

change (*Dickens* 2001, *Kennett et al.* 2000). The widespread presence of gas hydrates in the northern Cascadia margin sediments has been attributed to diffuse upward fluid migration, driven by compaction of the subducted sediments (*Hyndman et al.* 2001). There is also evidence for localized, near-seafloor hydrate accumulations that are formed from focused fluid flow in narrow migration conduits. To assess the long-term energy potential of gas hydrate and the role it plays in global climate change, the Integrated Ocean Drilling Program (IODP) Expedition 311 in September 2005 sought to derive a detailed geological model to understand the formation and dissociation of hydrate and its association with

fluid flow across the continental margin. Prior to the expedition, seismic experiments were carried out over the continental slope to provide geophysical information in support of drilling. The second part of the dissertation presents analysis of seismic single channel and wide-angle reflection data from the above experiment and the drill hole data from IODP Expedition-311 Site U1327. Estimates of hydrate concentration and distribution are made to help constrain models of fluid flow and hydrate formation.

1.2 Tectonics of southwestern Canada

As part of the modern plate tectonic regime of western North America, the Cascadia subduction zone extends from northern California in the south to southern British Columbia in the north (Fig. 1.1). The region is characterized by the interaction of three tectonic plates: the larger Pacific and North American plates and the smaller intervening Juan de Fuca plate. Convergence has been the dominant mode of plate interaction for the past 150 Ma (*Riddihough* 1982, *Engebreston et al.* 1992) with alternating periods of northeast-directed convergence and northwest-directed transform motion.

Currently, the Juan de Fuca plate subducts beneath the North American plate at a relative rate of 40-47 mm/a directed N56°-68°E (*Riddihough and Hyndman* 1991, *DeMets et al.* 1990). The Explorer plate (Fig. 1.3) is separated from the Juan de Fuca plate by the Nootka fault zone and has been moving independently for at least 4 Ma (*Riddihough* 1984). It is converging at variable rates along the margin with an average estimated convergence rate of 21 mm/a directed N50°E (*Riddihough and Hyndman* 1991). The oceanic lithosphere entering the Cascadia zone is young, less than 10 Ma (*Riddihough* 1984, *Rogers* 1988, *Wilson* 1993).

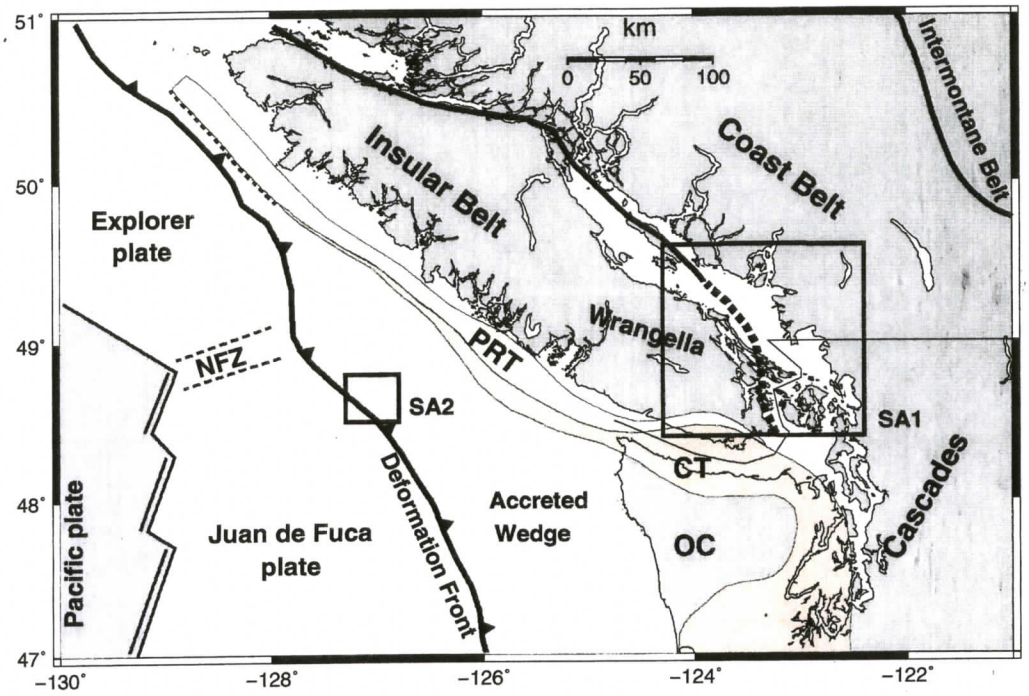

Figure 1.3: Map of the northen Cascadia subduction zone showing major tectonic features. PRT, Pacific Rim Terrane; CT, Crescent Terrane; OC, Olympic Complex; NFZ, Nootka Fracture Zone. The boxes SA1 and SA2 are the present study areas.

1.2.1 Regional geology

Southwestern British Columbia is part of the southern Canadian Cordillera, which is composed of a number of allochthonous terranes assembled on the western edge of North America during Jurassic to Tertiary time. The geological structure of the terranes is shaped by the oblique convergence of the Pacific plate towards the North American plate that has allowed materials from far away in the Pacific Ocean to be accreted to the continental margin of North America (*Riddihough* 1982). At about 180-200 Ma, the Intermontane superterrane, mostly made up of island arc and ocean floor volcanic rocks of Paleozoic age, collided with the North American plate. The Insular superterrane collided with the Intermontane superterrane in a major collisional event around the mid-Cretaceous time ($\sim$ 100 Ma). It is composed of two older terranes, Wrangellia terrane in the south

and Alexander terrane in Alaska that were amalgamated at about 320 Ma. The Insular superterrane consists of island arc and ocean floor volcanic rocks with thick assemblages of overlying oceanic sedimentary rocks. The collision of the Insular superterrane with the existing Intermontane superterrane generated the mid-Cretaceous to early Tertiary intrusive rocks of the Coast Belt (Fig. 1.3) over the region of suture (*Monger et al.* 1982). The Intermontane and Insular superterranes underlie, respectively, the Intermontane and Insular morphogeological belts and are separated by the Coast Belt. During the late Cretaceous to early Tertiary (about 54 Ma), the small sedimentary Pacific Rim terrane was emplaced south and west of the Insular superterrane. Subsequently during the middle to late Eocene time (about 42 Ma), during the north Pacific plate reorganization, the volcanic Crescent terrane (also called the Siletz terrane in Oregon) was accreted against the Pacific Rim terrane.

The modern accretionary complex has formed beneath and against the Crescent terrane by scraping off the incoming sediments on the subducting Juan de Fuca plate (*Hyndman et al.* 1990). The forearc Tofino basin (Fig. 1.4) is formed by the deposition of up to 4 km of Eocene to Recent marine clastic sediments over the Pacific Rim and Crescent terrane and the inner portion of the modern accretionary wedge and covers most of the continental shelf.

1.2.2 Geology of Vancouver Island and Georgia Basin

Vancouver Island is dominated by Wrangellia rocks that belong to the Insular Belt, the westernmost belt of the Canadian Cordillera (Fig. 1.3). Outcrops of the small Pacific Rim terrane are found along the west coast and the southern part of the Island. It includes

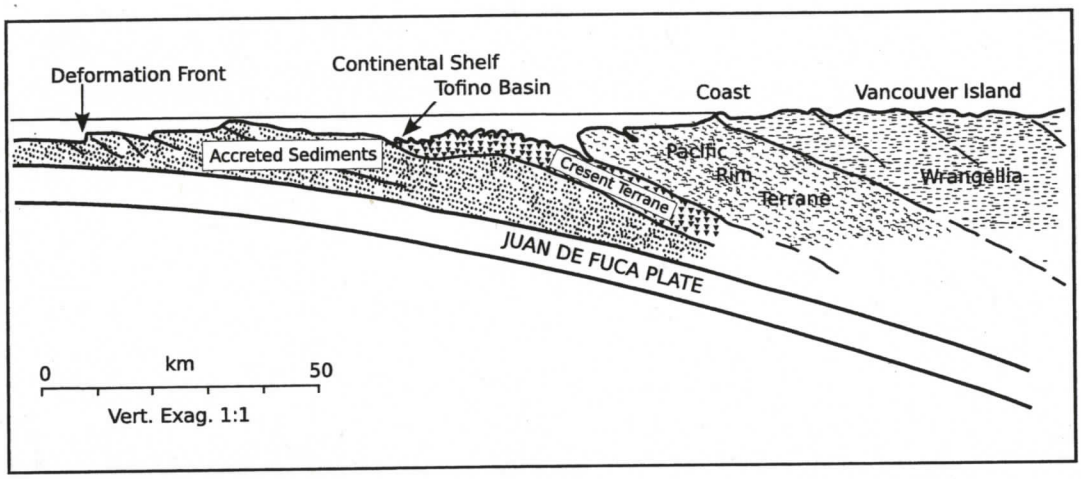

Figure 1.4: Cross section across the continental margin offshore Vancouver Island.

a metamorphic sediment-rich mélange unit in contact with Wrangellia rocks along the San Juan-Survey Mountain fault system (Fig. 1.5). The Crescent-Siletz terrane outcrops on the southern tip of the Island and is separated from the Pacific Rim terrane by the Leech River fault. It comprises voluminous submarine and subaerial basalts of tholeiitic composition with minor amounts of alkali basalts. The Olympic Complex to the south of Vancouver Island (Fig. 1.3) is an exposed former accretionary wedge, metamorphosed and uplifted as a result of subduction (e.g., *Brandon and Calderwood* 1990).

As part of Wrangella terrane, the oldest rocks on Vancouver Island are the Late Devonian arc-related volcanic and sedimentary rocks of the Sicker Group. These are overlain by Upper Carboniferous to Lower Permian clastic rocks and carbonates of the Buttle Lake Group. The Karmutsen Formation above the Sicker Group contains up to 6 km thick Middle to Upper Triassic tholeiitic basalts (*Monger* 1990). It is further divided into three units: a 2500 m thick basal member composed of pillow lava; a 600-110 m thick pillow breccia in the middle; and 3000 m thick upper member composed of basalt flows with minor amounts of pillow lava and some sedimentary layers. The carbonate rocks of the

Quatsino Formation overlie the Karmutsen Formation. The uppermost units of Wrangellia terrane are the Lower Jurassic arc volcanics of the Bonanza Formation and associated Early Jurassic rocks.

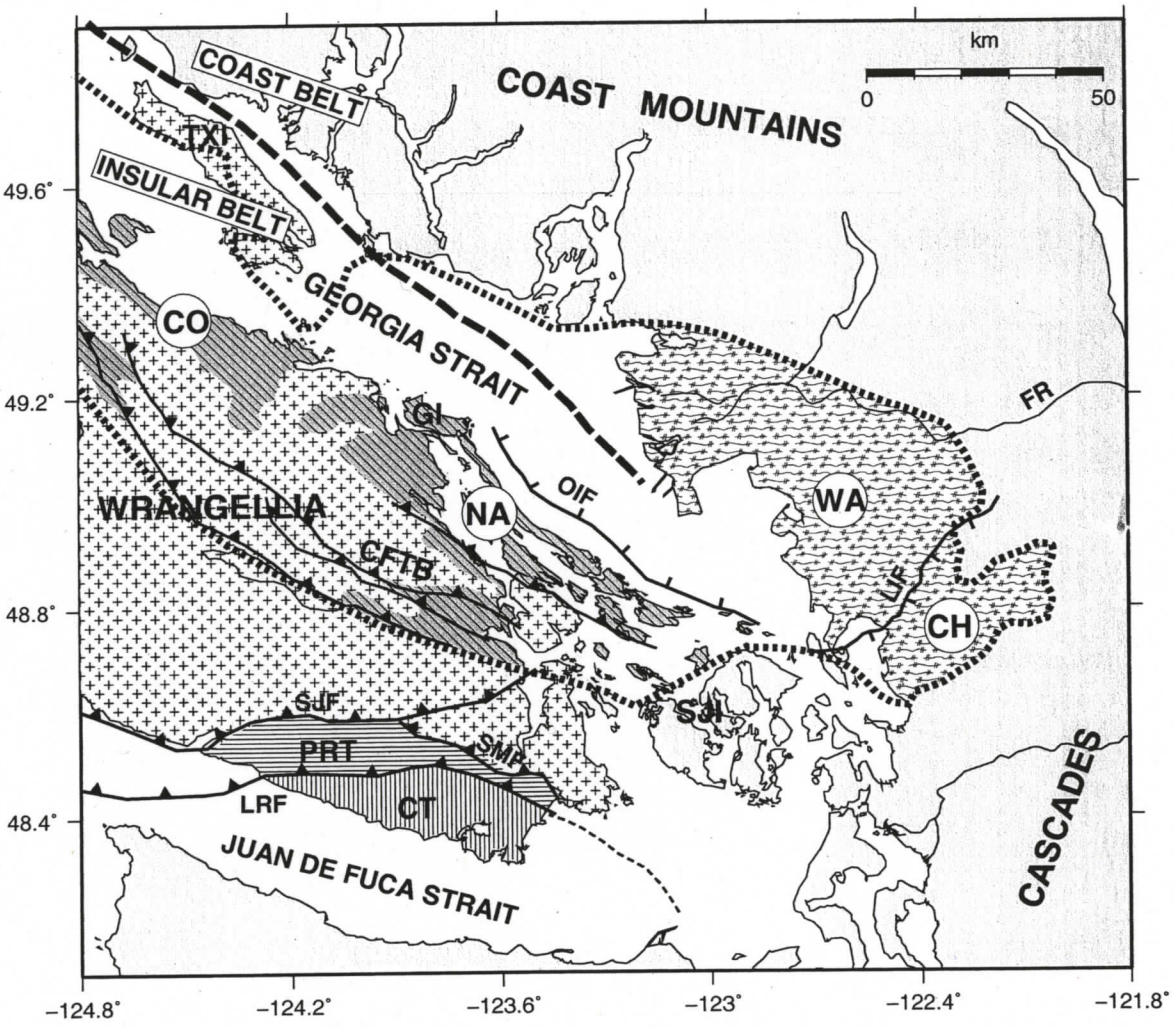

Figure 1.5: Regional geological map of the Georgia Basin showing major tectonic structures. The heavy dotted line outlines the boundary of the Georgia Basin. The boundary between the two westernmost tectonic belts (the Insular Belt and the Coast Belt) lies within the Strait of Georgia. Sedimentary rocks beneath the Georgia Strait comprise mostly the Upper Cretaceous Nanaimo Group, which are exposed on eastern Vancouver Island. Tertiary and Quaternary sediments are exposed in the southeastern part of the basin. Most of Vancouver Island is formed by Wrangellia rocks, which extend to the east to form the basement beneath most of Georgia Basin. Four subbasins mentioned in the text are: CO, Comox; NA, Nanaimo; WA, Whatcom, and CH, Chuckanut. Other abbreviations: PRT, Pacific Rim Terrane; CT, Crescent Terrane, CFTB, Cowichan fold-and-thrust belt; TXI, Texada Island; GI, Gabriola Island; SJI, San Juan Islands; SJF, San Juan fault; OIF, Outer Island fault; LIF, Lummi Island fault, SMF, Survey Mountain fault; LRF, Leech River fault; FR, Fraser River.

The northwest oriented Georgia Basin is a Cretaceous to Cenozoic structural and sedimentary forearc basin that encompasses the Strait of Georgia, eastern Vancouver Island and the Fraser River lowlands of British Columbia. The boundary between the Insular and Coast Belt lies near the eastern edges of the Strait of Georgia, although isolated outcrops of Wrangellia rocks are found in the western Coast Belt (*Journeay and Friedman* 1993). The sediments in Georgia Basin are siliciclastic, locally attaining a thickness in excess of 6 km and distributed over an area of approximately 25000 km^2 (*England and Bustin* 1998).

Georgia Basin overlaps four smaller sub-basins: the Cretaceous Comox and Nanaimo basins in the northwest and the Tertiary Whatcom and Chuckanut basins in the southeast of Georgia Strait (*England and Bustin* 1998). The Comox and Nanaimo basins contain several kilometers of siliciclastic deposits (mainly sandstones, shales and conglomerates) of the dominantly marine Upper Cretaceous Nanaimo group, exposed mainly on eastern Vancouver Island and the Gulf Islands of the strait. The rocks were deposited during a period of basin-wide subsidence in the Late Cretaceous. In southern Georgia Basin, they are in excess of 4 km thick (*Mustard* 1994, *Mustard and Rouse* 1994, *England and Bustin* 1998). Sedimentation in the Whatcom and Chuckanut basins occurred during a second phase of subsidence in the Late Paleocene to Late Eocene, which resulted in the accumulation of several kilometers of siliciclastic, mainly nonmarine sedimentary rocks (*Johnson* 1984, *Mustard and Rouse* 1994). These rocks are exposed in the Vancouver area and northwest Washington together with the Miocene rocks in the Fraser River delta area. The Whatcom basin primarily contains up to 2.5 km Paleogene sedimentary rocks of the Huntington Formation that are overlain by up to 1.2 km of Neogene sedimentary rocks of

the Boundary Bay Formation, and up to 1 km of Quaternary fluvial and deltaic deposits of the Fraser River (*Mosher and Hamilton* 1998, *Clague et al.* 1983). The Chuckanut basin contains about 6 km of Paleogene continental sediments of the Chuckanut Formation and overlying Quaternary deposits (*England and Bustin* 1998). The Chuckanut basin is separated from the Whatcom basin by the east-to-northeast striking Lummi Island-Boulder Creek fault system (*Johnson* 1985). Seismic tomographic studies by *Zelt et al.* (2001) and *Ramachandran et al.* (2004) reveal that Georgia Basin is much thinner in the northwest (2 - 4 km thick), whereas in the southeastern part of the strait, the maximum basin thickness is about 9 km.

Basement rocks in Georgia Basin comprise three distinct geological units: Wrangellia terrane rocks of the Insular Belt to the west, the Coast Belt to the east, and the rocks of the Cascade Mountains to the south and southeast (e.g., *Monger* 1990). The Coast Belt is made up largely of Middle Jurassic to Early Cretaceous granitic and granodioritic rocks of the Coast Plutonic Suite and various metamorphosed sedimentary and volcanic rocks. In the Cascade Mountains, the basement consists of a variably metamorphosed assemblage of Mesozoic sedimentary strata and other diverse rock types (*Monger* 1990).

Seismic reflection profiling on Vancouver Island gives evidence that Wrangellia is an east-dipping, internally-imbricated thrust sheet, possibly 20 km thick (e.g., *Clowes et al.* 1987). The extension of Wrangellia rocks to the east and the nature of the contact with the rocks of the Coast Belt may vary along the boundary between the Insular and Coast Belts. *Mulder and Rogers* (1998) used the differences in Poisson's ratio between the Insular and Coast Belts to conclude that Wrangellia rocks are not emplaced beneath the Coast Belt and that the suture zone between the two belts must lie beneath the Strait of Georgia, or

possibly at the western edge of the Coast Belt. *Lowe et al.* (2003) observed a pronounced west-to-east decrease in gravity values over the eastern part the strait that they interpreted as the boundary between the Wrangellia and the Coast Belt.

Deformation of Georgia Basin occurred in Tertiary during the accretion of the Pacific Rim and Crescent terranes to Wrangellia, which resulted in southwest-verging thrusts (the Cowichan fold and thrust system) and up to 30% shortening of the Nanaimo Group strata in the southwestern Georgia Basin and northwest-trending folds in the Chuckanut Formation in southeastern Georgia Basin (*Johnson* 1984, *England and Calon* 1991). Current tectonics within Georgia Basin are dominated by compressive stress parallel to the continental margin (*Wang et al.* 1995) and oriented north-northwest as derived from focal mechanism solutions and shear-wave anisotropy studies of recent earthquakes. Deformation of shallow sedimentary rocks within Georgia Basin (e.g., east of Gabriola Island) is evident in the multibeam swath bathymetry data (*Barrie and Hill* 2004) (Fig. 1.6). The topographic lineament in the swath bathymetry data corresponds to the shallow Outer Island fault (OIF). Crustal seismicity beneath the Strait of Georgia is persistent, with frequent occurrence of shallow earthquakes (Fig. 1.2). However, only for a few of the earthquakes has it been possible to make associations with mapped faults (*Cassidy et al.* 2000).

1.2.3 Structure of the accretionary prism

The northern Cascadia margin accretionary prism has evolved over the last 40 Ma from the incoming sediments that are scraped off the downgoing Juan de Fuca plate at the deformation front (*Davis and Hyndman* 1989). The prism is bounded at its base by the oceanic

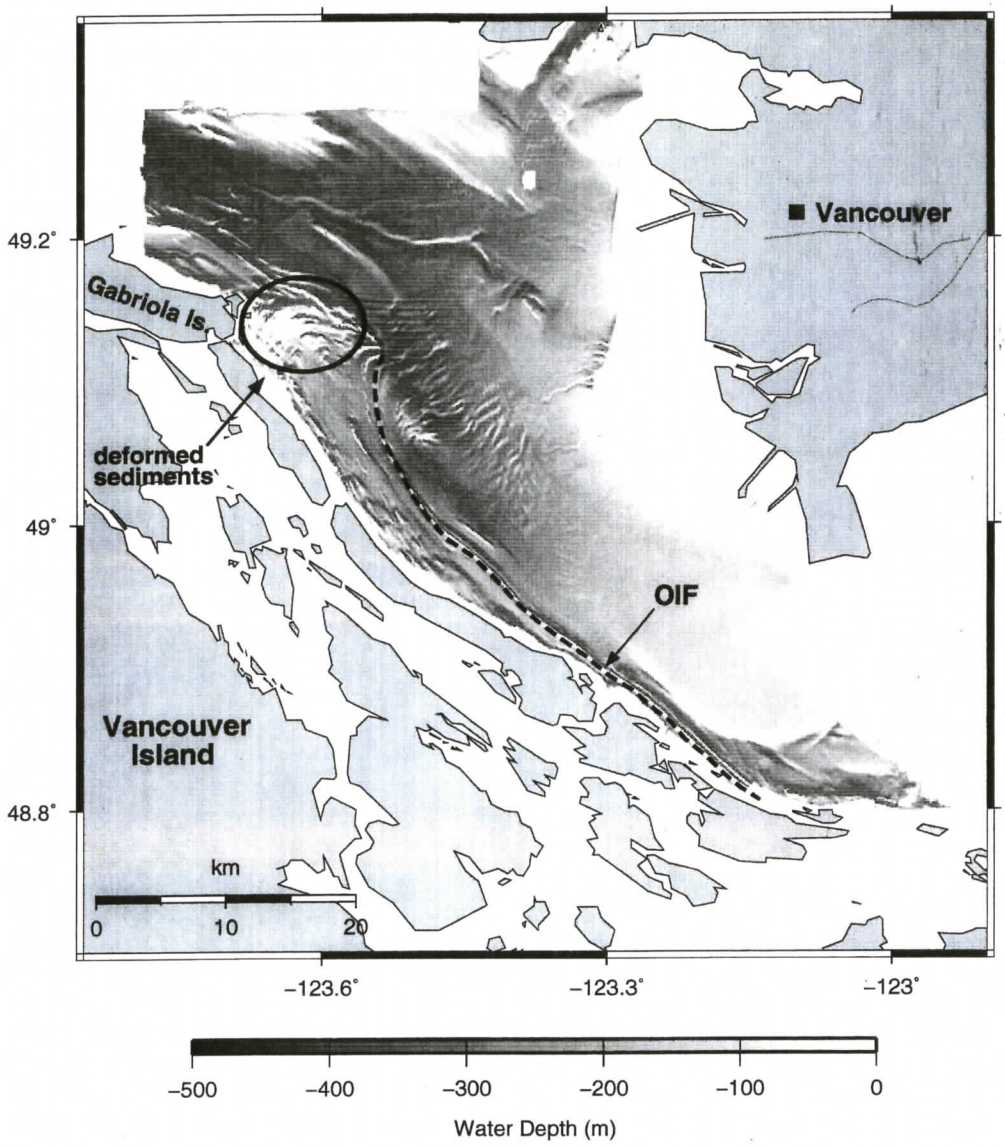

Figure 1.6: Swath bathymetry map of the southern Strait of Georgia. OIF - Outer Island fault.

plate and on its landward side by the landward-dipping Crescent Terrane (Fig. 1.4). The incoming sediment succession consists of a pre-Pleistocene, relatively transparent unit of fine-grained hemipelagic sediments overlain by rapidly deposited, coarser Pleistocene turbidites and has a thickness of 2.5-3 km at the deformation front (Fig. 1.7). The oceanic plate is very young (about 6-8 Ma) and buoyant. It gently dips at the deformation front

at an angle of 3-4°. The thick sediment section and the small dip angle result in a very subdued and shallow trench with water depths of about 2500 m (*Hyndman et al.* 2001). Tectonic compaction of the accretionary prism has resulted in a series of margin-parallel anticlinal ridges and landward-dipping thrust faults. At the base of the continental slope, the anticlinal ridges stand as much as 700 m above the adjacent basin floor. Landward of the deformation front, the seafloor rises rapidly through a series of well-defined thrust faults. The thrust faults penetrate very close to the top of the underlying oceanic crust as observed by several multichannel seismic (MCS) profiles across the continental prism (*Hyndman et al.* 1990). This implies that most of the sediments are scraped off the incoming oceanic crust and there is little underplating beneath Vancouver Island. *Davis and Hyndman* (1989) observed that the accretionary prism sediments are under elevated pore pressure.

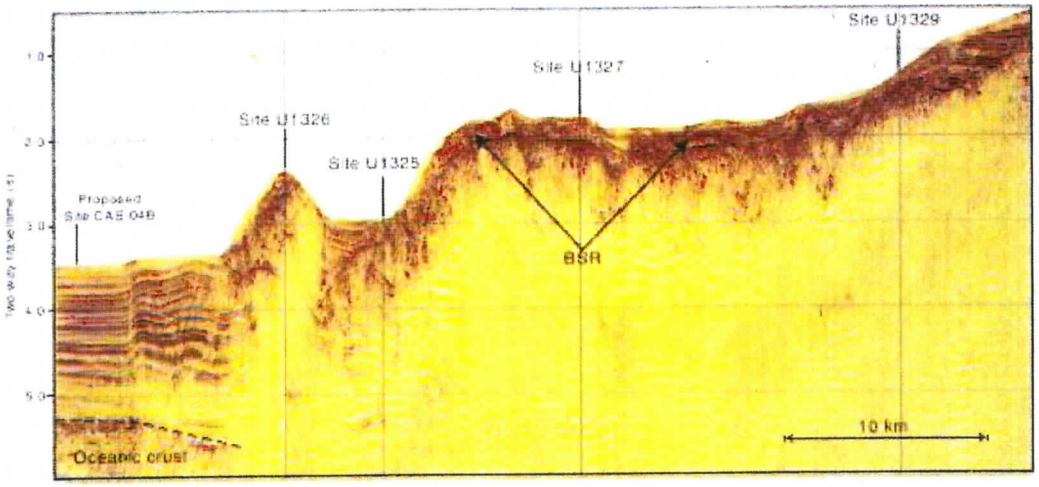

Figure 1.7: Accretionary prism structure from multichannel seismic profile 89-08 across the continental slope. Also shown are the drill hole sites of IODP Expedition 311.

1.3 Previous geophysical studies near Vancouver Island

A number of important regional seismic reflection and refraction studies have been carried out over the northern Cascadia margin. The most significant are the seismic reflection studies around southern Vancouver Island in 1984 and 1985, carried out by the Lithoprobe program onshore and the Geological Survey of Canada offshore. The seismic reflection data from the Lithoprobe program were interpreted by *Clowes et al.* (1987) to determine the large scale structures of the accreted terranes exposed on Vancouver Island and the geometry and structural characteristics of the subducting Juan de Fuca plate. *Clowes et al.* (1987) found that the Juan de Fuca plate is continuous below the deep sea sediments and discontinuous below the continental slope, shelf and Vancouver Island. They also observed three reflective bands (C, D and E) beneath Wrangellia and correlated the top reflective unit C to the Olympic subduction complex. The high velocity reflective band D in the middle was interpreted either as a detached slab of oceanic lithosphere or an imbricated package of mafic rocks derived by continuous accretion from the top of the subducting plate. The lower reflective layer E was interpreted as accreted marine sedimentary rocks. While *Hyndman* (1988) attributed the reflectivity to fluid-filled porosity created by dehydration reactions associated with a change in metamorphic grade at an approximately isothermal level within the crust, *Calvert and Clowes* (1990) proposed that the reflectivity is due to intensely sheared sediments that trap the fluid rising from the subducting plate. The location of the layer beneath southern Vancouver Island, as proposed by *Calvert* (1996), is about 5 - 10 km above the Wadati-Benioff zone. *Graindorge et al.* (2003) observed high gravity values over southern Vancouver Island and

found that the E-band is weaker to the south. *Calvert* (1996) concluded from analysis of reflection profiles that beneath southern Vancouver Island the reflections represent a former subduction decollement where one or two mafic units were underplated beneath the overlying continent. *Zhao et al.* (2001) obtained a seismic tomographic image of Vancouver Island from earthquake data and identified an extensive low velocity zone within the mantle above the subducted slab at 45 km depth and interpreted this feature as a possible indicator of partially-hydrated mantle, most likely serpentinite.

A number of local geophysical studies have been carried out to image the shallow structure within the Georgia Basin. *Zelt et al.* (2001) and *Ramachandran* (2001) obtained three-dimensional velocity models for Georgia Basin and the surrounding areas from the tomographic inversion of SHIPS traveltime data. *Mosher et al.* (2000) correlated the shallow geological structures with recent seismicity within the Strait of Georgia by analyzing aeromagnetic and SHIPS multichannel seismic data. *Mosher et al.* (2000) observed broad folding of sedimentary rocks in the southern part and two broad deformation zones in the northen part of the strait. The northern deformation zone correlates with a region of frequent shallow crustal activity 30 km west of Vancouver. *Lowe et al.* (2003) compared the observed gravity field with the tomographic velocity model of *Zelt et al.* (2001) and found four anomalous regions with thick accumulations of unconsolidated Pleistocene sediments that were unresolved in the tomographic model.

1.4 Gas hydrates

Gas hydrates are naturally-occurring, ice-like crystalline compounds in which natural gas (mostly methane) is trapped within cages of water molecules. Their formation and

stability in the subsurface depend upon appropriate physical conditions, such as low temperature, and high pressures. Their stability also depends on pore fluid salinity and on the type of trapped gas. As well, it depends on sufficient influx of free gas (*Kvenvolden* 1994) or on the amount of gas dissolved in the pore fluid (*Xu and Ruppel* 1999). The presence of hydrates in the pore space strongly affects the mechanical properties of the host sediment, in particular increasing the seismic velocity, which makes it possible to infer their presence over wide areas in seismic surveys of various continental margins. On P-wave seismic profiles, gas hydrates are detected from the observation of the characteristic Bottom Simulating Reflectors (BSRs), which are subparallel to the seafloor, and have high-amplitude and reverse polarity relative to the seafloor reflection. The BSR commonly represents the base of the hydrate stability zone, although for low fluid or gas fluxes the BSR may lie above the base of hydrate stability zone (*Xu and Ruppel* 1999).

1.4.1 Gas hydrates on the northern Cascadia margin

The Cascadia margin hydrate was first detected in 1985 on a multichannel seismic reflection data survey (*Davis and Hyndman* 1989). *Hyndman and Spence* (1992) observed strong, widespread BSRs over much of the continental slope off Vancouver Island, and assumed that they correspond to the base of the gas hydrate stability zone (GHSZ). The region has since been studied with a broad range of geophysical surveys including seismic (*Fink and Spence* 1999, *Yuan et al.* 1996, 1999, *Riedel et al.* 2002, *Zühlsdorff et al.* 1999, *Chapman et al.* 2002, *Spence et al.* 1995, *Hobro et al.* 2005), heat flow (*Davis et al.* 1990, *Riedel et al.* 2006b), electrical and electromagnetic studies (*Edwards* 1997, *Yuan and Edwards* 2000), seafloor compliance (*Willoughby and Edwards* 2000) and geological

studies such as piston coring (*Novosel* 2002, *Riedel et al.* 2002, *Solem et al.* 2002). From the distribution of the BSR, the presence of hydrate in the accretionary prism sediments is inferred over a 30 km wide band at water depths ranging from 800 - 2200 m. The BSR occurs at depths of 200 - 300 m below the sea floor (mbsf). Based on multichannel velocity analyses, *Hyndman and Spence* (1992) concluded that a high-velocity layer exists above the BSR. The layer has a sharp base and a transitional top indicating a decrease in hydrate concentration upwards from the base of the hydrate stability zone. Downhole data from Ocean Drilling Program (ODP) Site 889 and 892 show low velocities immediately below the BSR indicative of free gas (*MacKay et al.* 1994). Integration of downhole data from ODP Site 889 and regional seismic velocities provided estimates for hydrate concentration of up to 20 to 30 % of the pore space. At ODP Site 889, hydrate was found at depths from approximately 127 to 228 mbsf based on geochemical core analysis and wireline logs (*Westbrook et al.* 1994). Recent studies have also confirmed near-seafloor hydrate accumulations in the continental slope (*Riedel et al.* 2006b). *Riedel et al.* (2006b) integrated geophysical and geochemical studies to develop a vent model incorporating all constraints to explain the near-seafloor hydrate accumulations.

Since the concentration of methane in hydrates is much greater than the in situ concentration of methane in the sediments, gas must be carried from much greater depths. *Hyndman and Davis* (1992) proposed a fluid expulsion model for the formation of gas hydrates in the subduction zone accretionary prism. Tectonic consolidation of the prism sediments leads to upward migration of methane through sediment pores or small-scale fractures. The upward-moving methane is incorporated into hydrate as it enters the hydrate stability field (Fig. 1.8). *Westbrook et al.* (1994) and *Paull and Ussler* (1997)

described another important process for the hydrate formation above the BSR. Upward movement of the base of hydrate stability may result from (a) incorporation and uplift of the incoming sediments into the accretionary prism, (b) sedimentation and (c) post-Pleistocene increase in bottom water temperature. Decrease of pressure or increase in temperature causes the base of the stability field to move upward. The dissociated gas from the lowest part of the hydrate then moves upwards forming hydrate again.

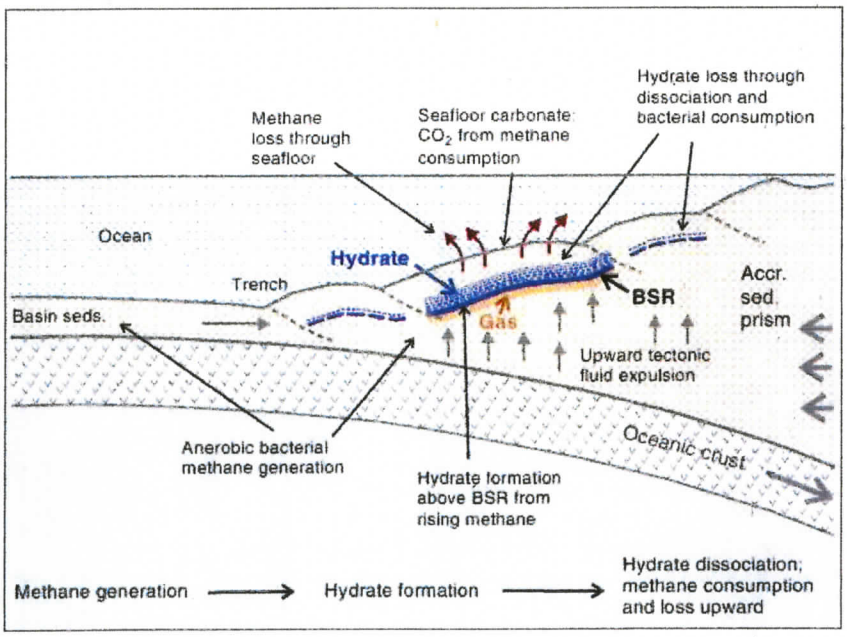

Figure 1.8: Fluid expulsion model for the formation of gas hydrate in the accretionary prism (after *Hyndman and Davis* (1992)).

Xu and Ruppel (1999) developed a mathematical model for the formation of hydrates from upward methane advection and diffusion and showed that the base of the hydrate may be above the base of the stability field and the top of free gas below the base of the stability field. *Davie and Buffet* (2001) developed a numerical model for hydrate formation and distribution in passive continental margin and found that the formation of hydrate depends on the rate of sedimentation, the quality of organic material entering the

sediments and the biological productivity. The sediment rate has alternating effects on the hydrate volume. Lower rates of sedimentation reduce the supply of carbon causing less hydrate formation. On the other hand, higher sedimentation rates can also lower the hydrate volume because rapid sedimentation will bury organic carbon beneath the hydrate stability zone before it is utilized by bacteria. *Liu and Flemings* (2007) developed a multiphase fluid and heat flow model that accounts for the dynamic effects of hydrate formation on salinity, temperature, pressure, and hydraulic properties. In their model, methane is primarily transported by buoyancy as a continuous gas phase into the regional hydrate stability zone (RHSZ). In zones of high gas flux, free gas supplied from depth forms hydrate, depletes water, and elevates salinity until pore water is too saline for further hydrate formation. In low-flux regions and in fine-grained sediments, hydrate formation leads to rapid permeability reduction and to sealing of capillaries.

The Integrated Ocean Drilling Program (IODP) Expedition 311 was designed to further constrain geological models for the formation and dissociation of marine gas hydrates in accretionary prism environments (*Riedel et al.* 2005a, 2006a). The locations of the IODP drill sites are shown in Figure 1.7. Site U1326 is near the deformation front where the rate of fluid flow is expected to be the highest. However, Site U1327, which is a more landward site, has been experiencing fluid flow for a longer period of time. One of the primary objectives of Expedition 311 was to test whether or not the local hydrate accumulation increases landwards.

1.5 Outline of dissertation

This dissertation presents studies of shallow crustal velocity structure in two different geological settings near Vancouver Island using seismic tomography and other associated seismic methods. In chapter 2, data collection and preparation methods for the various datasets used in this study are presented. The tomographic study of Georgia Basin uses first arrival traveltime data from the 1998 SHIPS and the 2002 GBGI wide-angle seismic experiments. The study of the hydrate-containing sediments in the accretionary prism uses normal-incidence and wide-angle seismic reflection data from ocean bottom seismometers (OBS). A key data preparation step presented is the relocation of OBS, from the inversion of direct arrival traveltimes through the water column.

Chapter 3 discusses an imaging method that involves migration of the downgoing multiples from the OBS data. The subbottom image produced from the migration of multiples is shown to be equivalent to that obtained from near-surface streamer data. The method is useful for sparse ocean bottom receivers.

In Chapter 4, the theory of nonlinear seismic tomography is discussed. Both three-dimensional (3D) and two-dimensional (2D) tomographic methods are described. The ill-posedness of the inverse problem was solved by applying *a priori* information. Model parametrization, ray tracing and regularization techniques are discussed.

The seismic velocity structure of the Georgia Basin as obtained from the nonlinear tomographic inversion of the first arrival traveltimes is presented in Chapter 5. The velocity structure is constrained down to about 7 km depth. The shallow crustal faults are correlated with the seismicity.

In Chapter 6, the seismic velocity structure for the shallow sediments near IODP Site U1327 is described. The velocity obtained from simultaneous ray-trace modelling of the wide-angle and normal-incidence data matches very well with the sonic log data from Site U1327. The average hydrate concentration within the pore space is estimated from the seismic velocity, and the results are integrated with the IODP downhole data.

Chapter 2

Seismic data collection and preparation

2.1 Seismic experiments in the Strait of Georgia

To investigate the shallow crustal structure of Georgia Basin and the adjoining areas, two separate seismic refraction experiments were conducted: the 2002 Georgia Basin Geohazards Initiative (GBGI) experiment within the Strait of Georgia and the 1998 Seismic Hazards Investigation in Puget Sound (SHIPS) experiment covering the Strait of Georgia, the Strait of Juan de Fuca and the Puget Sound region of Washington.

2.1.1 Georgia Basin Geohazards Initiative

The GBGI experiment was a collaborative effort of the Pacific Geoscience Centre (PGC, Geological Survey of Canada, GSC), the United States Geological Survey (USGS) and the University of Victoria. The primary objective was to provide the geoscientific knowledge necessary for effective decision making on the environmental and resource management issues in the Georgia Basin (*Riedel* 2002). The experiment, conducted using Canadian Coast Guard research vessel **J.P. Tully** and temporarily deployed land-based

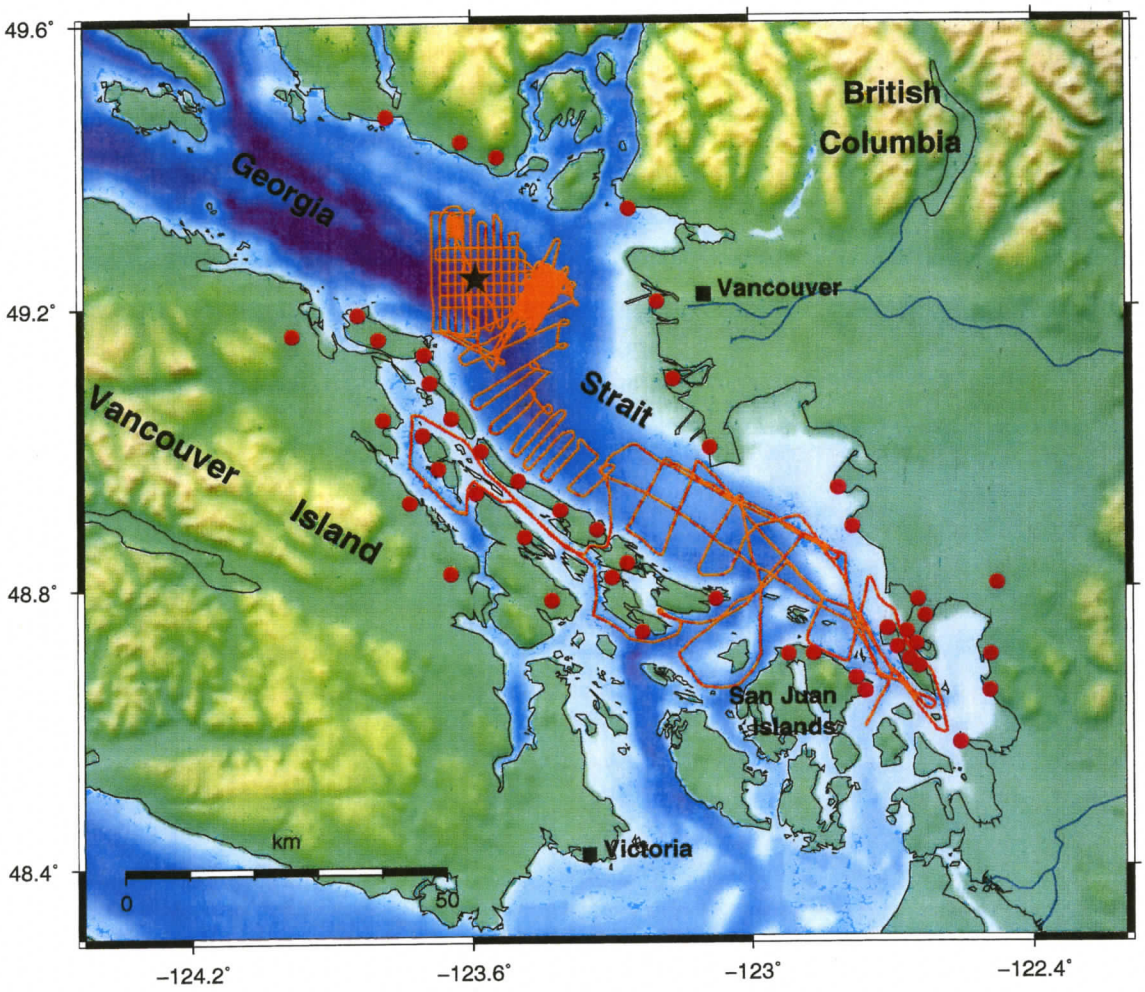

Figure 2.1: Map of the Strait of Georgia showing the Georgia Basin Geohazards Initiative (GBGI) seismic experiment. Red dots and orange lines represent, respectively, the receivers and shot lines for the survey. The star marks the location of the 1975 and the 1997 earthquakes.

seismic recorders, was centred on the southcentral Georgia Basin (*Brocher et al.* 2003). The survey was designed to image the shallow crustal faults and the Cenozoic sedimentary basin, and to add to the existing SHIPS wide-angle data from the area. The cruise was divided into two parts: the first part focused on the southernmost part of Georgia Basin including the Lummi Island fault and southern extent of the Outer Island fault, and the second part was focused on the location of frequent earthquake activity northeast of Gabriola Island, the northern extent of the Outer Island fault and known recent Holocene

faults in the vicinity of Vancouver. Seismic refraction/wide-angle reflection data were recorded with 48 temporary Reftek stations deployed on land surrounding the Strait of Georgia within 10 km of the planned ship tracks (Fig. 2.1). The locations for thirteen of the receiver stations were coincident with the previous SHIPS station locations. Each Reftek station used a three-component, 4.5 Hz seismometer that was connected to a GPS clock to record the absolute time. The source was a single 1.967 litre (120 cu. in.) airgun that operated at a nominal air pressure of 1900 psi. The airgun was towed at a water depth of 4 m and shots were fired at a nominal interval of 5 s or 12 m (*Brocher et al.* 2003). Nearly 160,300 individual airgun shots were recorded along 180 short seismic reflection lines (for a total line length of about 800 km). The shot navigation was achieved using a GPS receiver onboard the ship and the absolute shot coordinates were estimated to be accurate within 40 m. Single-channel normal-incidence and short-offset data were collected simultaneously. The dominant frequency of the data is 6-8 Hz, implying a wavelength of 0.4-1.1 km for P-wave velocities of 3-6.7 km/s.

The data quality at many receivers was very good. However, the signal-to-noise ratio (SNR) varied with the local ground conditions. For example, the stations located on thick sediments relatively close to the large urban areas (e.g., Vancouver) have a very poor SNR. On the other hand, stations located on older high-velocity bedrock (mostly on Vancouver Island) have excellent SNR. Figure 2.3 shows examples of wide-angle data from different parts of the strait with the shot locations given in Figure 2.2. Shots on the northwestern side of the strait provided useful data whereas the data quality on the east and southeast is moderate to poor. The average maximum source-receiver offset for the picked first arrivals was 17 km with a maximum offset of 35 km.

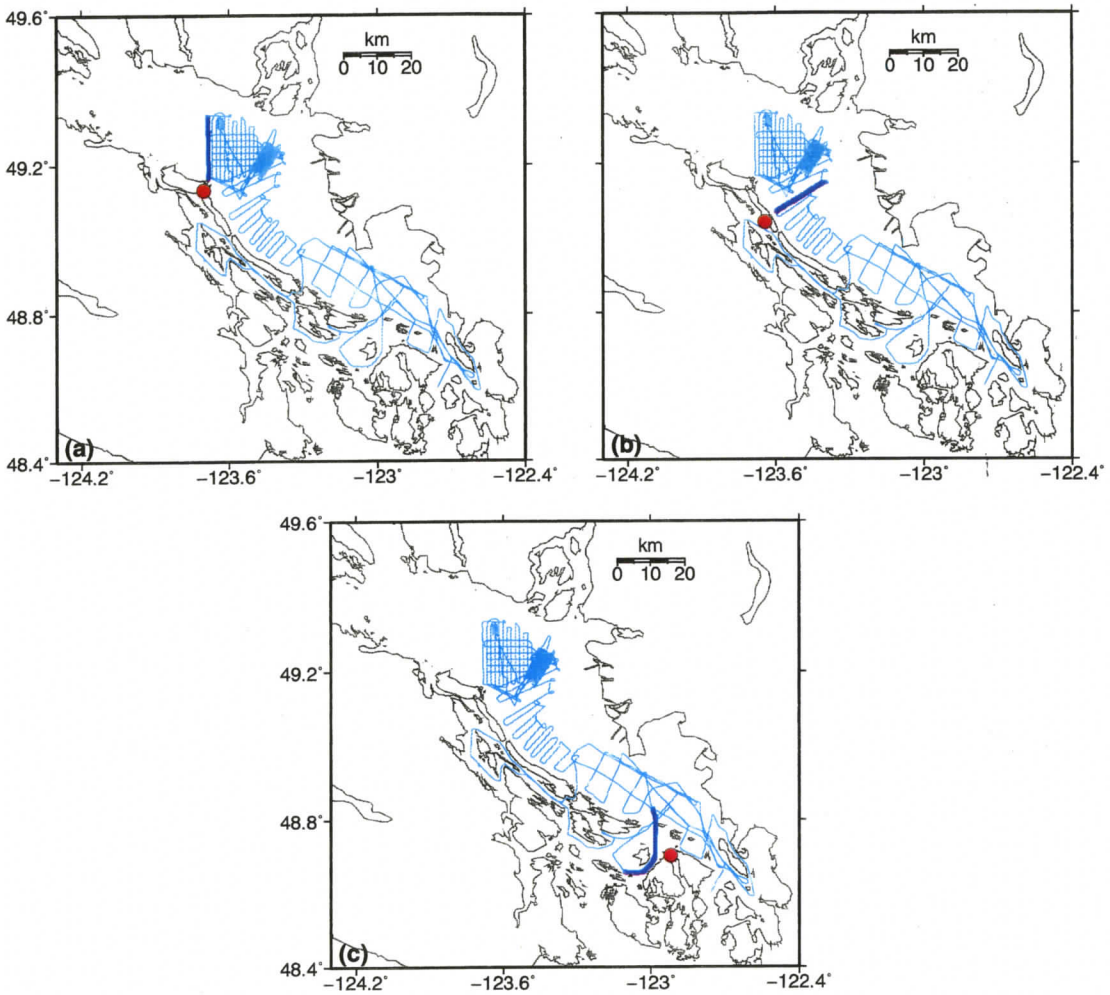

Figure 2.2: Solid dots and bold line segments indicate the location of Reftek stations and seismic profiles shown in Figure 2.3.

The experiment provided useful data from 40 of the 48 stations deployed. Three-fourths of all stations yielded useful first-arrivals to source-receiver offsets beyond 10 km. Eight stations yielded no useful data and useful first-arrivals were limited to offsets less than 10 km at five stations. The seismic data were first bandpass filtered (2 - 12 Hz) to remove the common high frequency noise and to facilitate first arrival picking on the time sections. First arrivals were picked manually with pick uncertainties varying from 10 to 200 ms, based on the difficulty in identifying the onset of the arrivals. A total of approximately 325,000 first-arrival traveltime picks were obtained from 38 receivers.

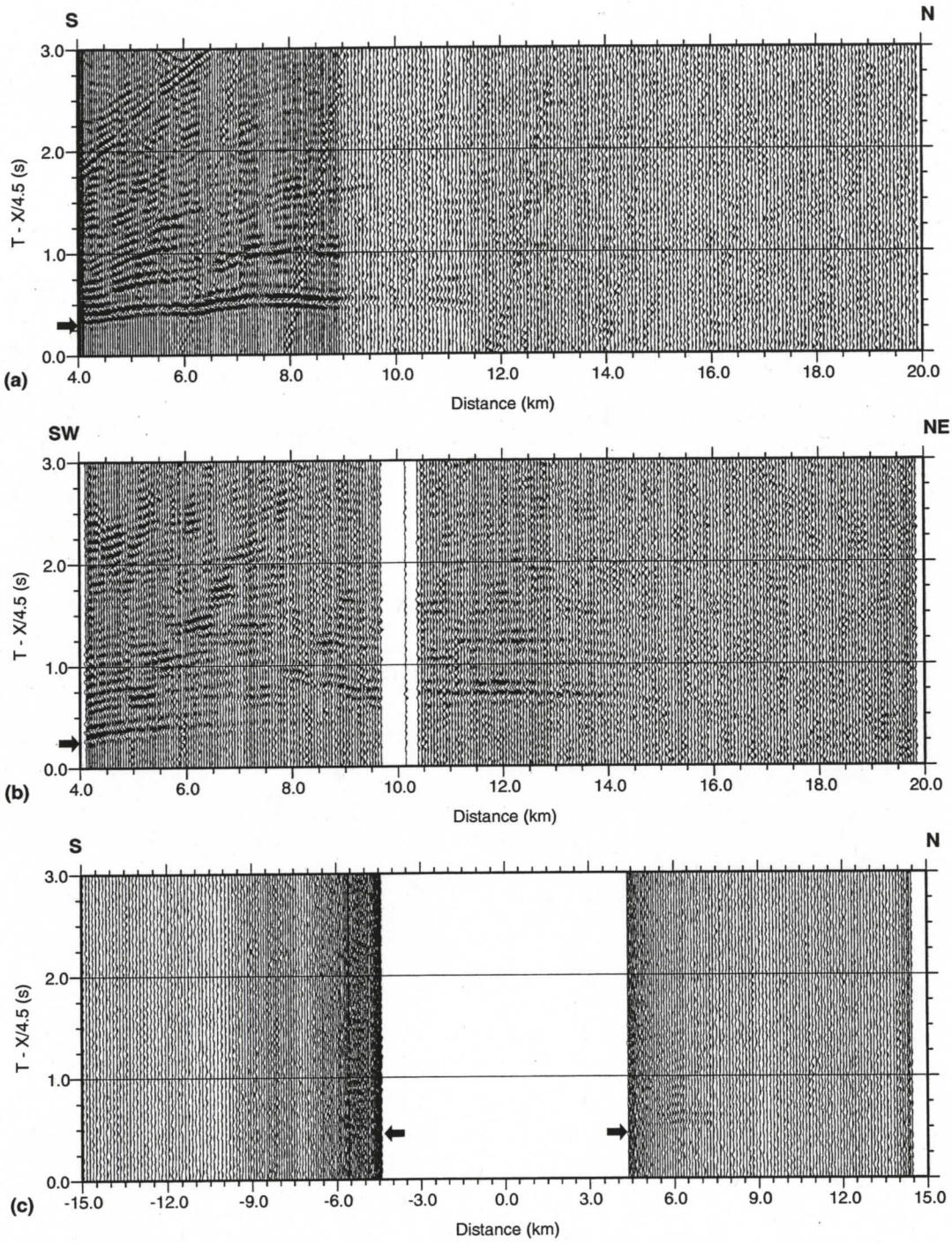

Figure 2.3: Examples of the wide-angle seismic data depicting the data quality at different regions in the strait. The locations of the shot lines a, b and c are shown in Fig. 2.2. Arrows indicate the onset of the arrivals. The data have been band-pass filtered between 2 Hz and 12 Hz to remove the high frequency noise. The seismic sections are plotted with a reducing velocity of 4.5 km/s. Notice the poor quality of data in the southern part of the strait.

2.1.2 Seismic Hazards Investigation in Puget Sound

A detailed description of the 1998 SHIPS experiment and data is given by *Brocher et al.* (1999) and *Ramachandran* (2001). The objective of the experiment was to map seismogenic zones and to obtain seismic velocity information for Cenozoic sedimentary basins in southwestern British Columbia and northwestern Washington (*Brocher et al.* 1999). The experiment covered the Strait of Georgia, Strait of Juan de Fuca and Puget Sound regions. A total of 33,000 airgun shots was fired along 11 shot lines and recorded at 257 Reftek stations distributed widely over southwestern British Columbia and northwestern Washington (Fig. 2.4). The Reftek stations used 3-component seismometers and recorded data at a sample rate of 100 Hz. For the first part of the experiment, which focused on the wide-angle data, shots were fired from a large airgun array consisting of 16 individual airguns (total volume of 110 litres) towed at water depth of 8 - 10 m and fired at an interval of 40 s or 90 m (*Ramachandran* 2001). In the second part of the experiment that included the recording of multichannel seismic reflection data, a smaller 13 airgun array (total volume of 79 litres) was used and the shots were fired at every 20 s or 50 m. The reflection data were recorded with a towed 2.4-km, 96-channel digital streamer. Estimated location accuracy was 40 m for the shots and 50 m for the Reftek stations.

For the present study, 56,000 first arrival picks were obtained from 25 stations and 2 shot lines within the Strait of Georgia. Comparable to the uncertainty estimates of *Ramachandran* (2001), pick uncertainties of 50, 70, and 90 ms were assigned to picks having first arrival travel times less than 10 s, between 10 and 15 s, and greater than 15 s, respectively.

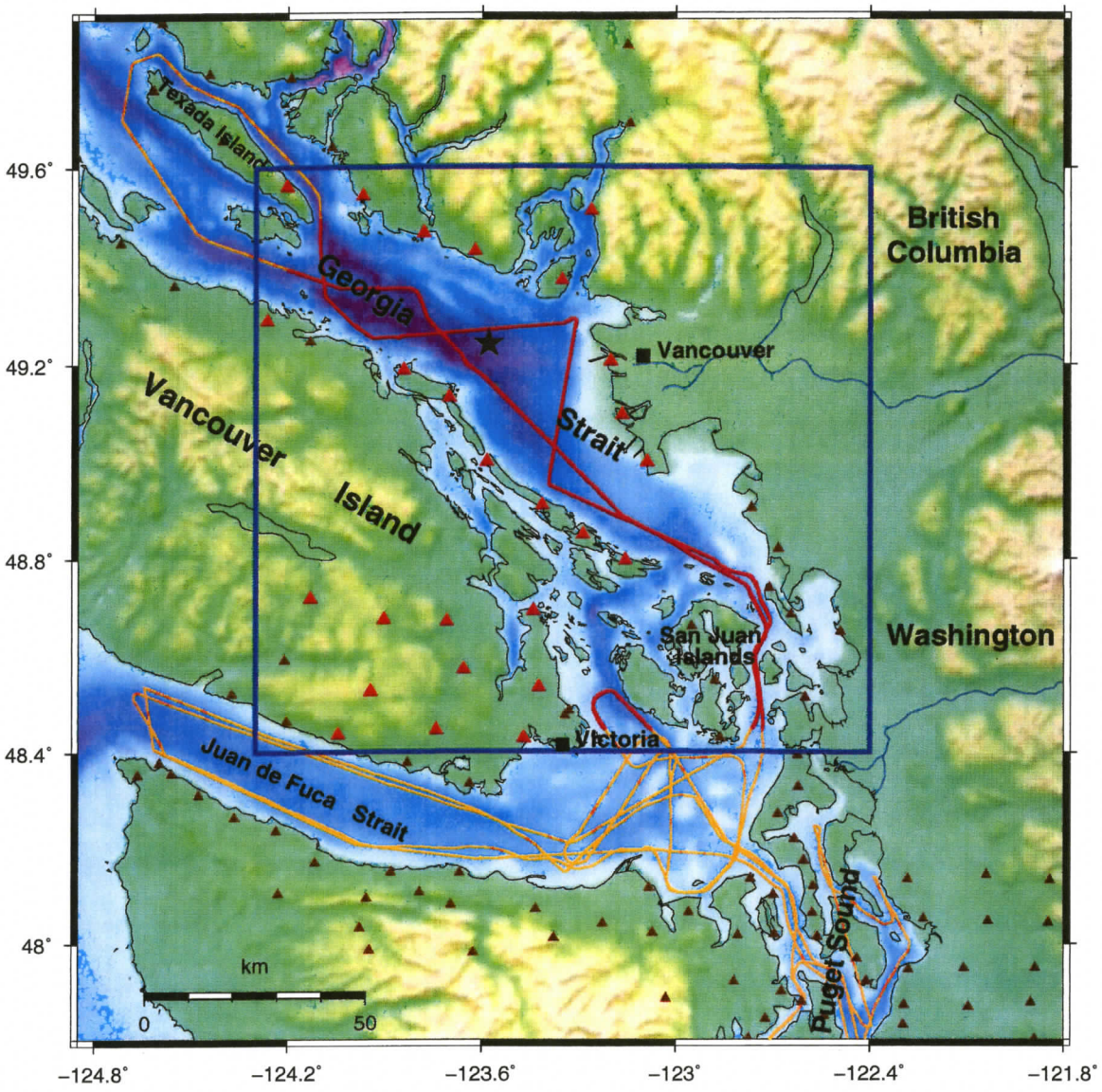

Figure 2.4: Map of the Strait of Georgia showing a part of the Seismic Hazards Investigation in Puget Sound (SHIPS) experiment. The orange and red lines are the shot lines. Triangles represent the receivers. Only the data from the receivers within the study area (marked by the red triangles) are used in this study. The star marks the location of the 1975 and the 1997 earthquakes.

2.2 Seismic experiment offshore Vancouver Island

In support of the hydrate research program of the Geological Survey of Canada and University of Victoria and as part of the site surveys for the International Ocean Drilling

Program (IODP) Expedition 311, seismic experiments were conducted on the continental slope off Vancouver Island in August/September 2005 (Fig. 2.5). The objectives were to image sedimentary structures that are associated with gas hydrate accumulations and to determine gas hydrate distribution and concentration from measurements of seismic velocity. This information should help to understand the processes of formation and dissociation of methane hydrate, and to characterize the associated methane and fluid flow within Cascadia margin sediments. Two deployments of Ocean Bottom Seismometers (OBS) were carried out in the vicinity of IODP Sites U1326 and U1327. Operational details of the experiment are described by *Spence et al.* (2005).

Ten OBSs from Dalhousie University were used during **C.C.G. J.P. Tully** cruise PGC005-09 to record wide-angle reflection and refraction data near the above mentioned sites. The OBSs were identified with letters A, B, C, D, G, H, I, K, L, N. Each OBS contained an *Onset Computer Corp. 16-bit Tattletale 7* data acquisition system that recorded four components of the seismic wavefield: one hydrophone recording pressure, and one vertical and two horizontal geophones recording the ground velocity. For timing purposes, each OBS was equipped with a high precision Seascan Inc. SAIL clock. The clocks were set before the deployment and the time differences were checked after their recovery using an Odetics/Zyfer GPS (Global Positioning System) Time and Frequency system. The OBSs were anchored with 100 lb metal plates that were left on the seafloor after the OBSs were released.

Single-channel vertical incidence reflection data from a Teledyne single channel streamer were collected simultaneously with the wide-angle data. The streamer had 50 hydrophones over a length of 25 m.

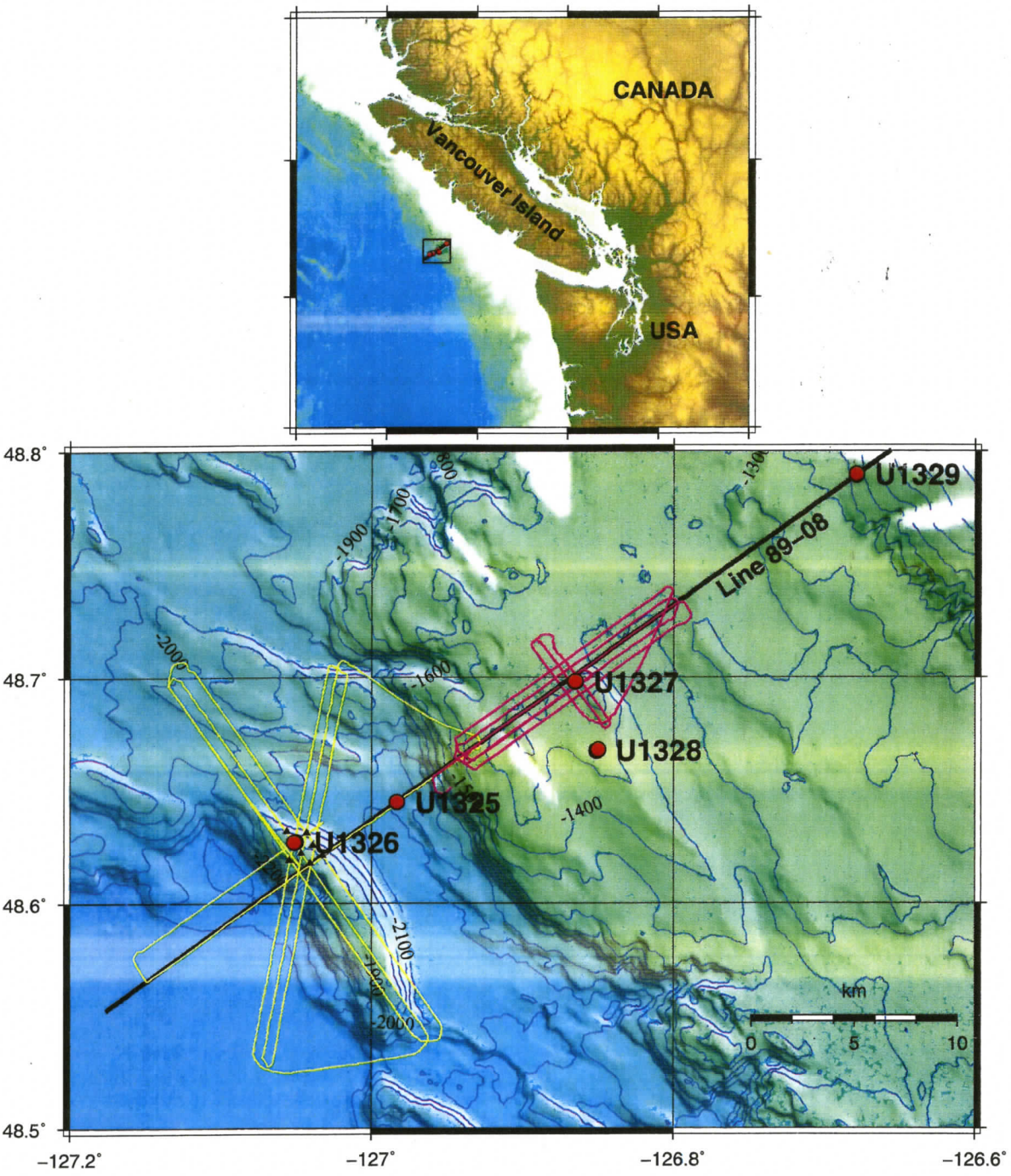

Figure 2.5: Seismic experiment on the continental slope offshore Vancouver Island. The top figure shows the location of the study area on the continental slope. The shot profiles near IODP Sites U1326 and U1327 are shown in the bottom figure.

The source used for all the OBS experiments was a *Seismic Systems Inc.* Generator-Injector (GI) gun obtained from *Sercel*, France. The GI gun is a dual-chamber air gun

designed to minimize the bubble pulse. The "injector" chamber of the GI gun discharged a short time (about 34 ms) after the "generator" chamber so as to suppress the bubble pulse and create an optimal signal. However, the source signature as recorded in the shot point hydrophone (Fig. 2.6) shows the presence of bubble pulses. The maximum volume of the GI gun was 105 cu. in. for each of the two chambers, with an operational pressure of 1900 psi. As evident from the amplitude spectrum the dominant frequency is about 120 Hz with significant energy from about 50 - 180 Hz.

At IODP Site U1327, all ten OBSs were deployed in alphabetical order along the southwest-northeast line, coincident with the multichannel line 89-08 (Fig. 2.7). The water depth at this site is about 1310 m. The line of OBSs that passed through ODP Sites 889A and 889B, and IODP Site U1327 was at a distance of about 200 m from the nearest OBS. The OBS separation was nominally 100 m. The GI gun was fired along 8 lines each separated by about 500 m. Lines 1 to 5 were parallel to the multichannel line 89-08, and the shorter lines 6 to 8, perpendicular to 89-08, were included mainly to help find the accurate position of the OBSs. The GI gun was configured with 45/45 cu. in. chambers (i.e., 45 cu. in. generator chamber and 45 cu. in. injector chamber), which fired shots at an interval of 6 s. Preparation of the OBSs took approximately 8-10 hours, while deployment took only about 1 hour. Recovery of the OBSs took about 5 hours. Except OBS D, all other OBSs recorded data for the whole period of the experiment. After recovery, the OBS clocks were calibrated for determining the clock drift during the experiment (Table 2.1). Clocks from OBS B and N were calibrated using previous year data as their recovery information could not be recorded precisely. The measured clock drift rates were small with a maximum value of 4 ms/day. The raw seismic data files were

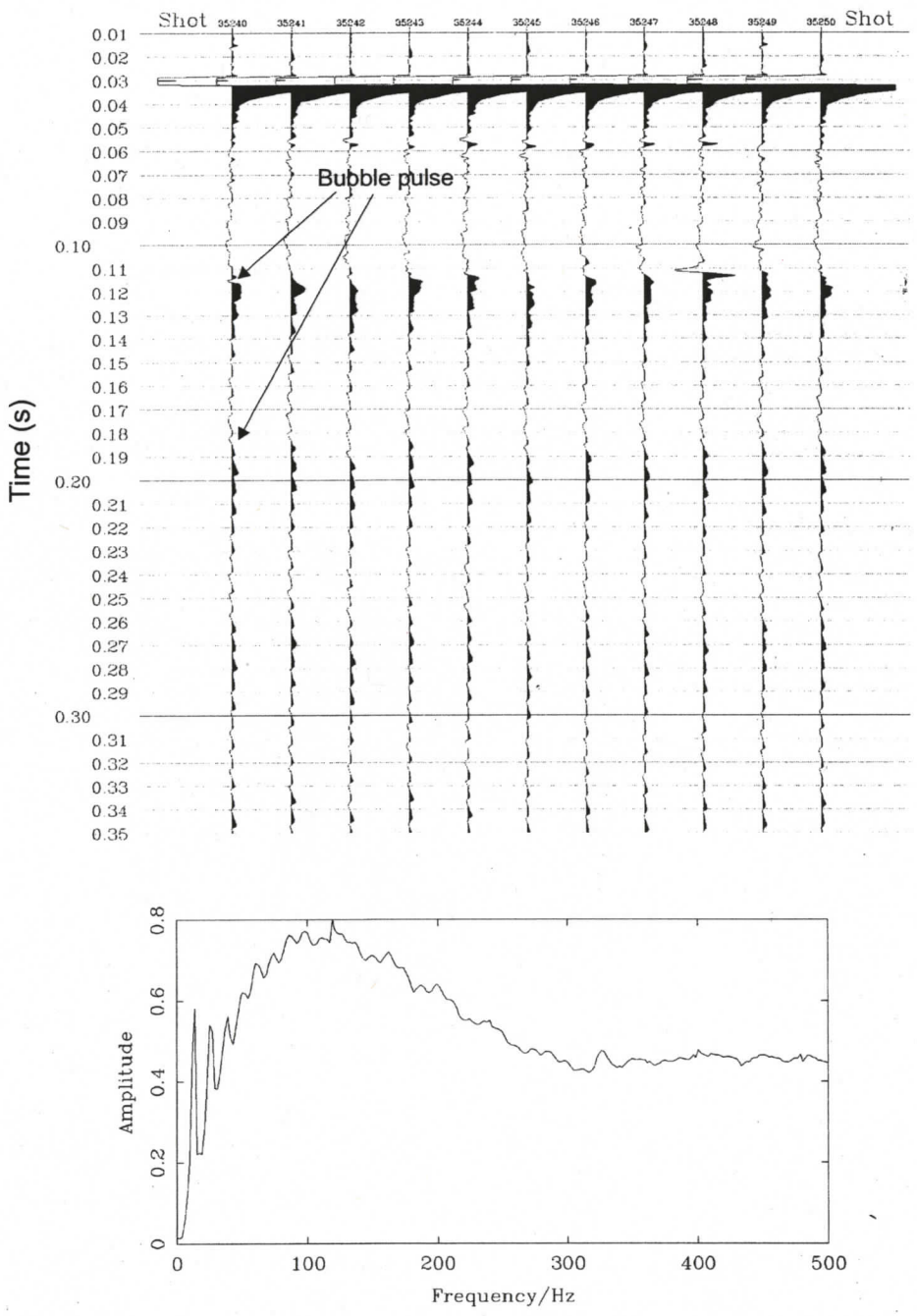

Figure 2.6: Source signature and amplitude spectrum of the GI gun (45/45 cu. in.) as recorded in the shot hydrophone. Significant energy is present from about 50-180 Hz, with a dominant frequency of about 120 Hz.

converted to SEGY format while correcting for the clock drift and the relative position of GPS antenna to airguns.

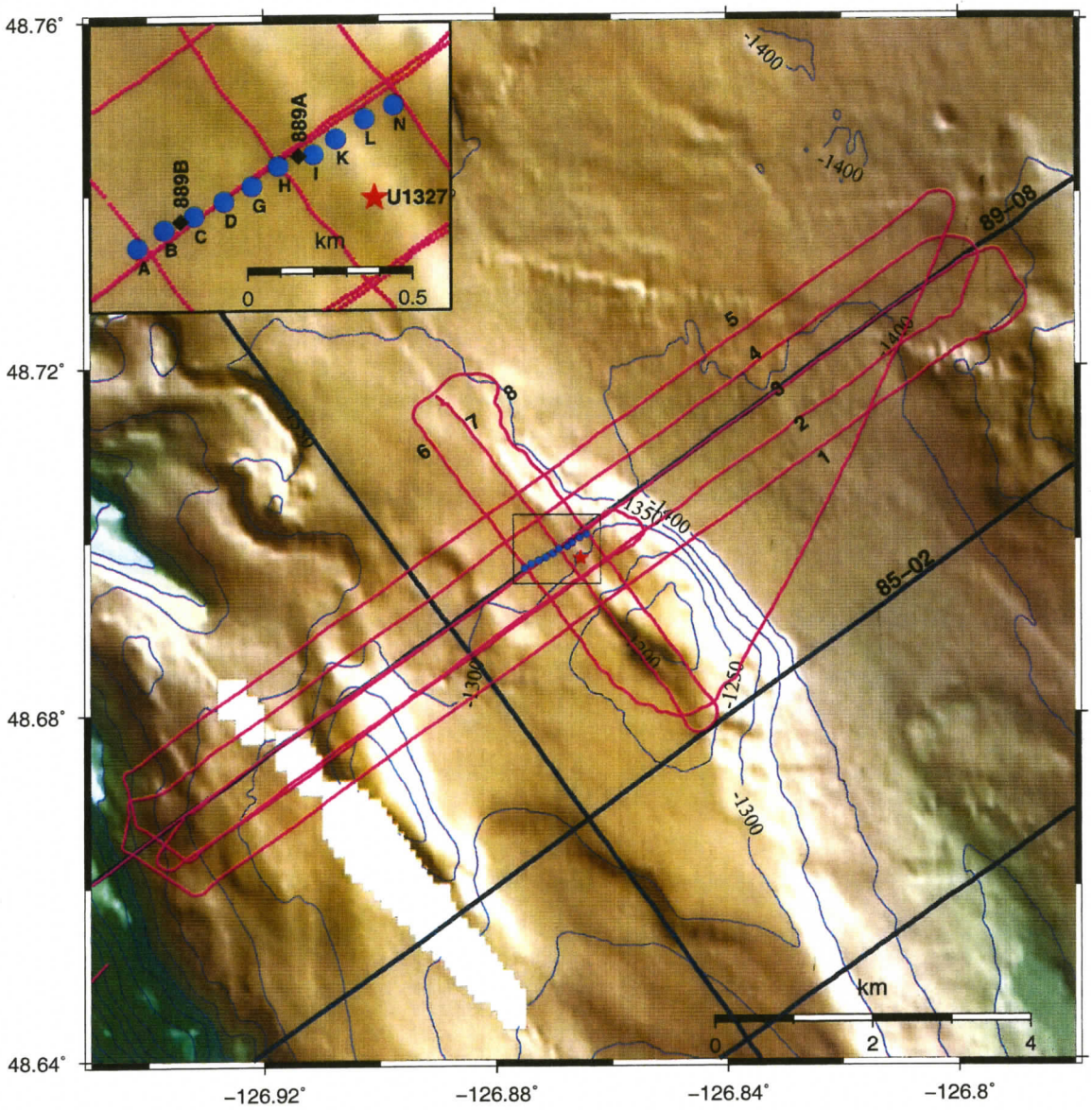

Figure 2.7: Seismic experiment near IODP Site U1327 (represented by the red star). Blue circles represent the deployed OBS positions. Diamonds represent the previous ODP drill sites in the area.

Near IODP Site U1326, eight OBSs were deployed in a grid pattern, each at 650 m separation (Fig. 2.5). The site is on the frontal ridge near the deformation front. The water depth is about 2300 m. The experiment was not fully completed because of the

Table 2.1: OBS clock drift information after recovery.

OBS	Clock set time (before deployment)	Clock check time (after recovery)	Total time (hrs.)	Drift (ms)	Drift rate (ms/day)
A	213:18:28	214:20:12	25.73	2.37	2.21
B	213:18:13	214:10:10	15.95	2.29	3.45
C	213:20:56	214:20:36	23.67	0.8	0.81
D	213:17:38	214:23:22	29.73	1.03	0.83
G	213:19:38	214:20:30	24.87	-0.42	-0.41
H	213:19:59	214:21:6	25.12	-1.48	-1.41
I	213:20:22	214:20:22	24.00	3.59	3.59
K	213:17:34	214:21:20	27.77	4.73	4.09
L	213:21:15	214:22:14	24.98	-0.47	-0.45
N	213:17:2	214:30:2	37.00	2.95	1.91

failure of the air compressor. Also poor sea conditions (30-35 kts wind; 2-3 m waves) resulted in very noisy single channel data. However, the OBS data were excellent due to the bigger air gun source (105/105 cu. in. chamber GI gun) used at this site. Preliminary analysis of these data are presented in *Lopez et al.* (2006).

Only the data from the experiment near IODP Site U1327 are described here. Both the normal incidence (SCS) and wide-angle (OBS) experiments produced good quality data. Deconvolution was applied to suppress the airgun bubble pulse, and a band pass filter (40-160 Hz) was applied to the single channel data. Figures 2.8 and 2.9 show examples of normal incidence reflection data perpendicular and parallel to the continental margin, respectively. In the northeastern part of Figure 2.8 and the northwestern part of Figure 2.9, the smooth and flat sea floor is associated with a large slope basin. The uppermost reflections are from the slope sediments (clayey silts and fine sands). Below the slope sediments lie the accretionary prism sediments, which are more consolidated and highly fractured. However, the boundary between the accreted sediment layer and slope

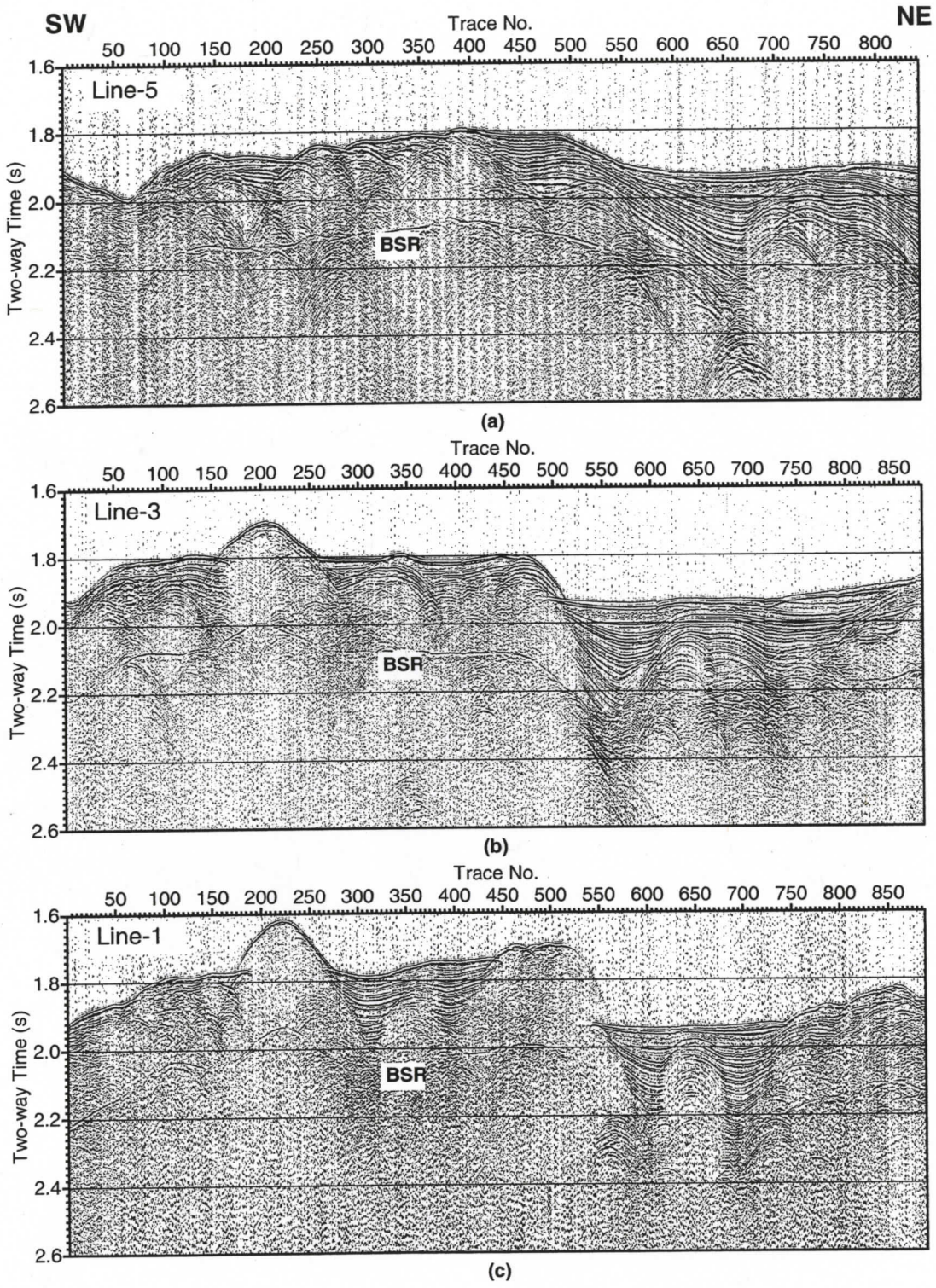

Figure 2.8: Single channel seismic data along shot lines 5 (a), 3 (b), and 1 (c) near IODP Site U1327. Line length is 12 km approximately. Line locations are shown in Figure 2.7.

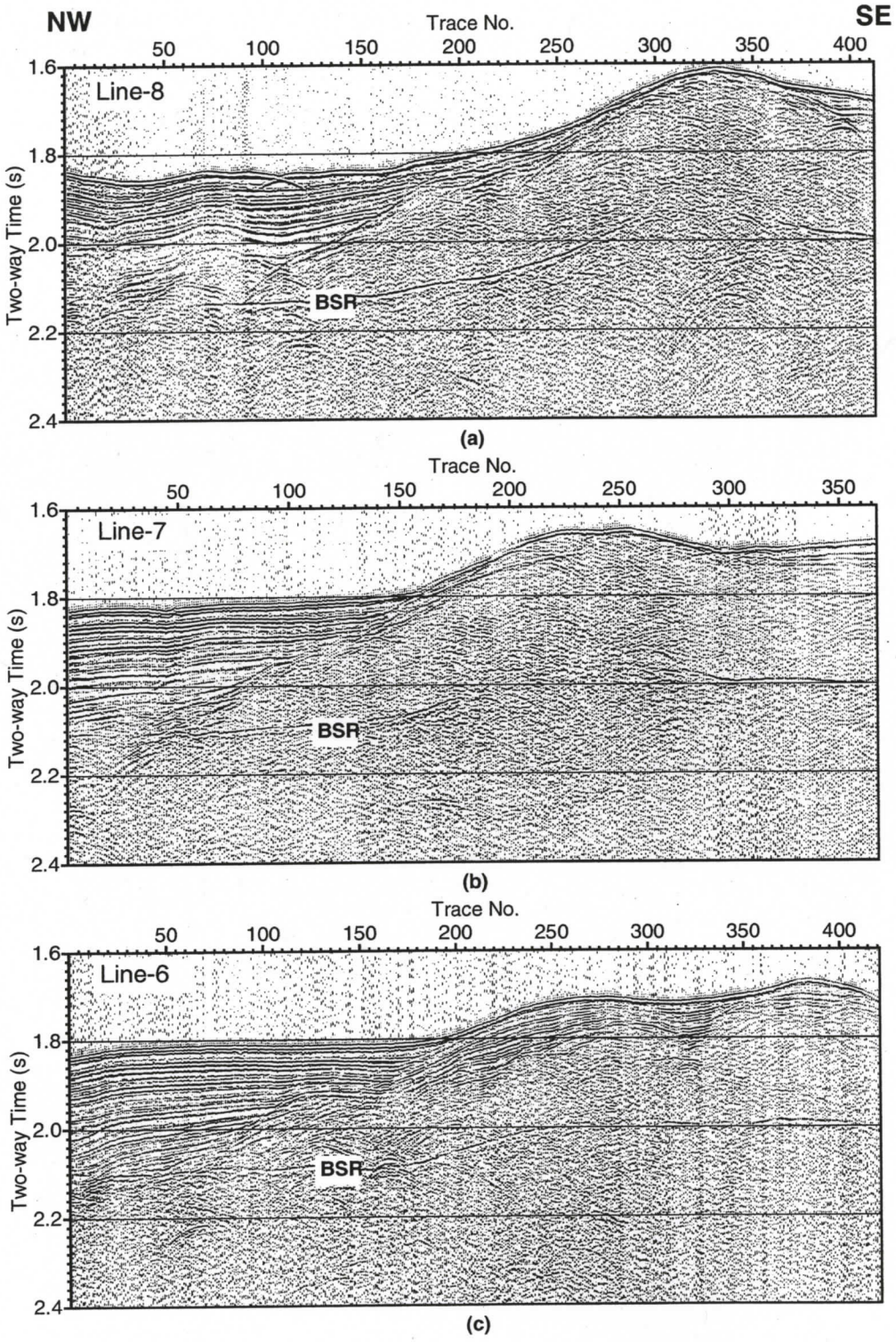

Figure 2.9: Single channel seismic data along shot lines 8 (a), 7 (b), and 6 (c) near IODP Site U1327. Line length is 6 km approximately. Line locations are shown in Figure 2.7.

sediments is not well-defined. The accreted sediments exhibit surprisingly few reflections probably because of pervasive deformation. The BSR (at about 280 ms below the seafloor) is clearly recognizable on all sections indicating the wide distribution of hydrates in the area. In the northeast portion of the shotlines, the sub-horizontal bedded slope sediments obscure the BSR.

The OBS data were collected out to 7 km maximum offset on either side of the deployed position. The data quality was good, but unlike the SCS data, the bubble pulse was prominent (Fig. 2.10) and obscured the primary reflections. Figure 2.11 (top panel) shows the amplitude spectrum before deconvolution. A gaped-deconvolution was applied to the pressure and vertical component geophone data. A bandpass filter of 10-110 Hz was then applied to the data to remove the high frequency noise (Fig. 2.11, bottom panel). The processed data clearly show the reflections including the BSR (Fig. 2.12). Refractions are almost absent in the OBS data. Where present, their amplitudes are very weak and their apparent velocities are very small ($\sim$ 1.65 km/s)(Fig. 2.13). The absence of any strong refraction indicates that there is no high velocity layer underneath.

The horizontal components have varying data quality (Fig. 2.14). Most of the horizontal components contain very high frequency spurious noise which could be related to the instrument. In some OBS horizontal components (e.g., OBS-G) no data are recorded; the reason for this is not well understood. On most OBSs, the presence of shear-waves (S-waves) in the horizontal components is evident. In particular, arrivals can be seen below the BSR, which occurs at a time of about 1150 ms at near offset. It must be noted that the OBSs were not directly below the shot line, so the minimum offset is not equal to zero. In pressure and vertical geophone components, events below the BSR are virtually

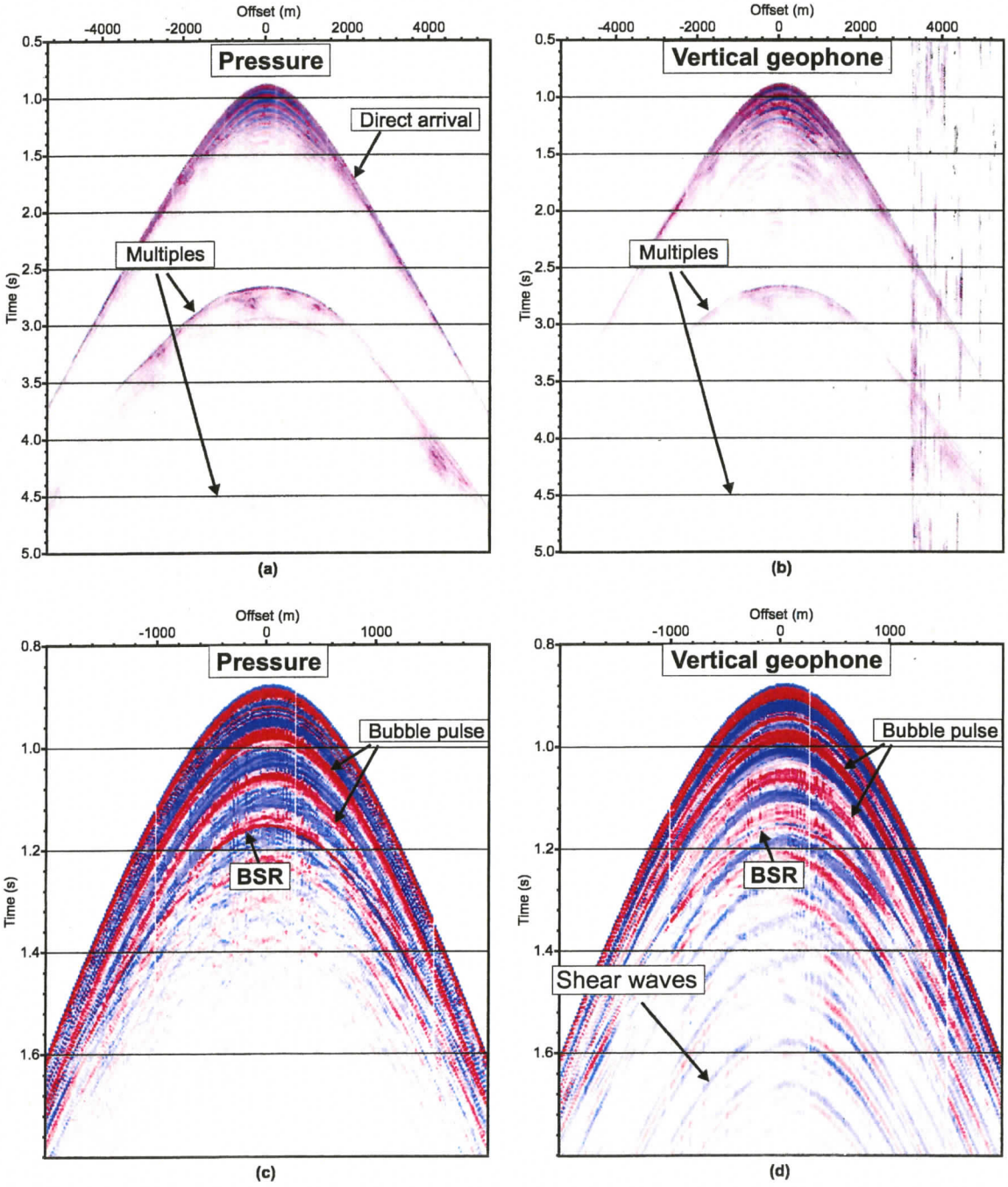

Figure 2.10: Pressure (a,c) and vertical geophone component (b,d) data recorded on OBS-A before deconvolution.

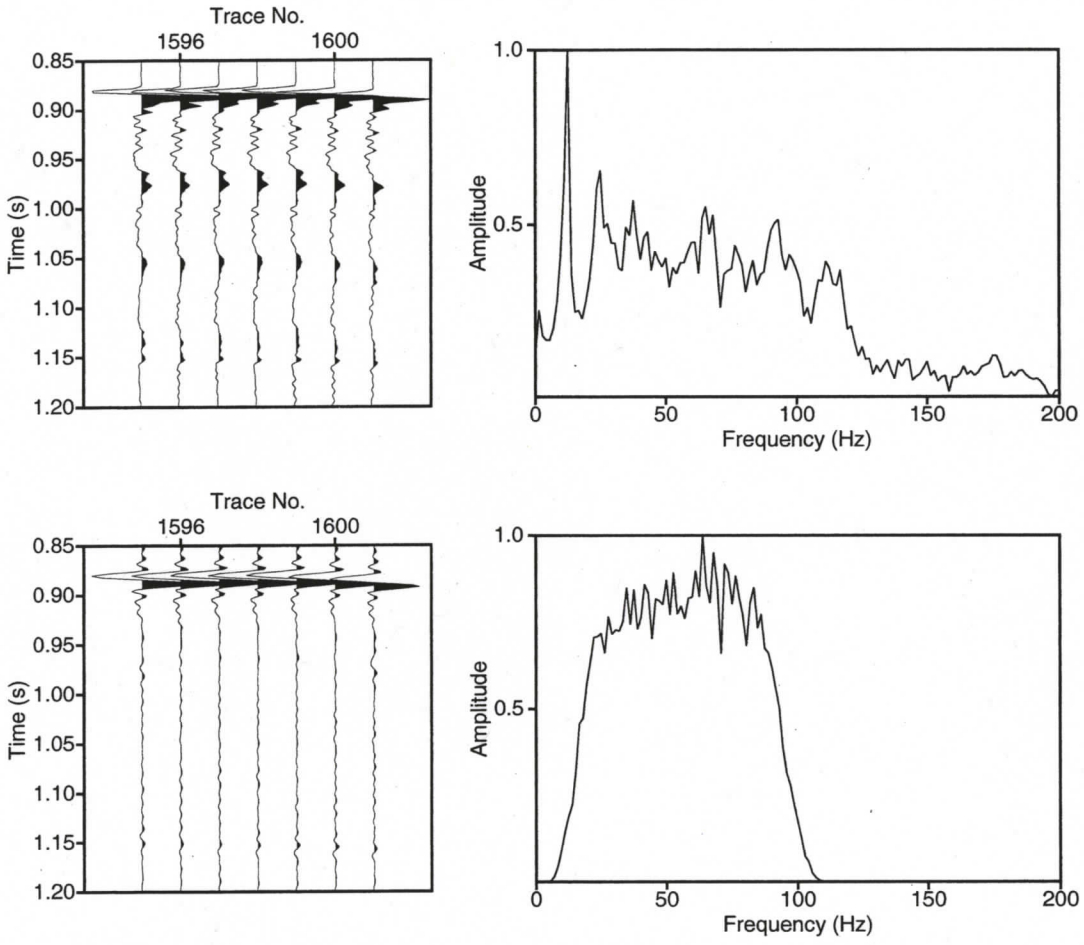

Figure 2.11: Sample traces and amplitude spectrum of the OBS data before (top) and after (bottom) deconvolution. A bandpass filter of 10-110 Hz was applied to the bottom data after deconvolution.

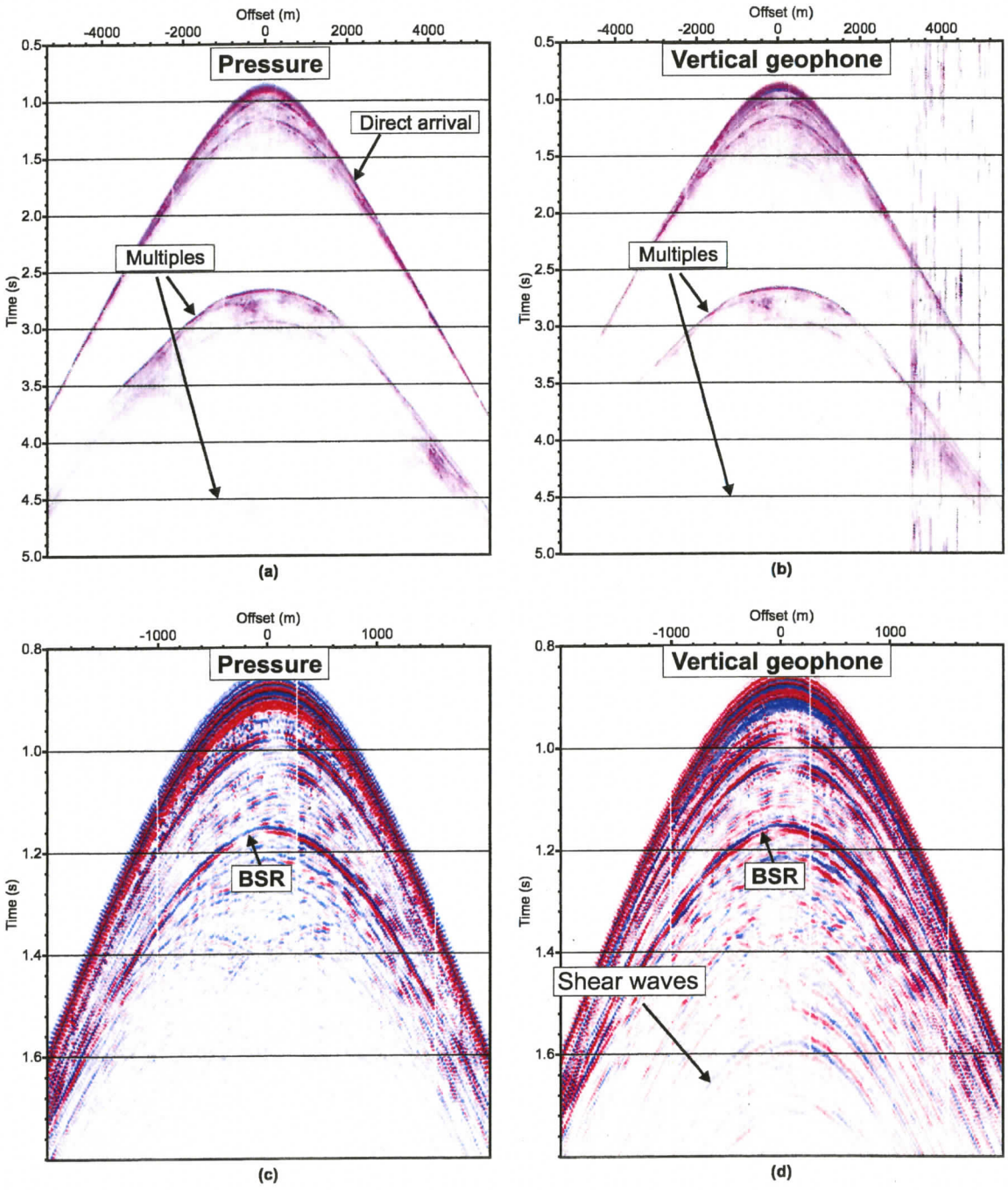

Figure 2.12: Pressure (a,c) and vertical geophone component (b,d) data recorded on OBS-A after deconvolution.

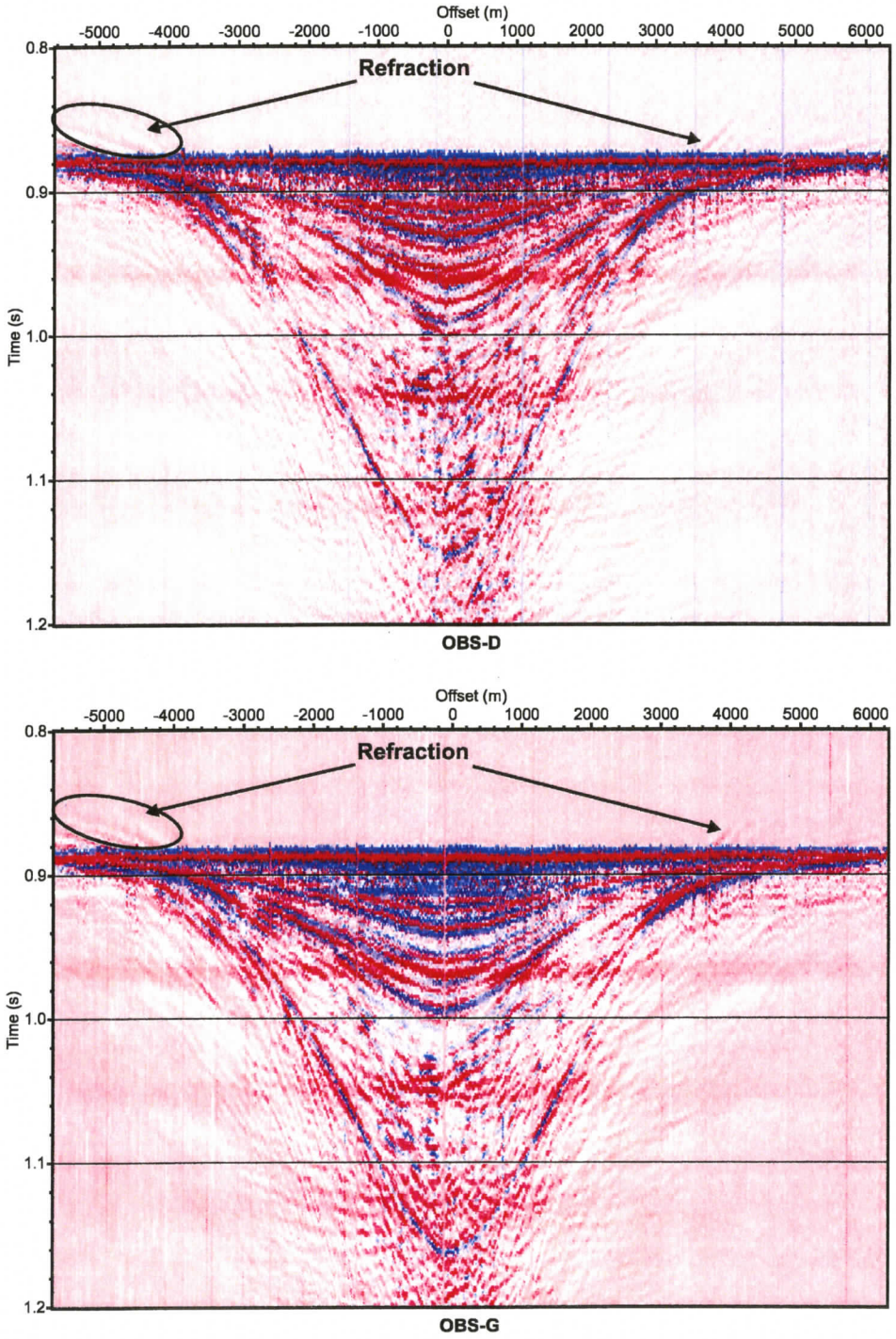

Figure 2.13: Hydrophone components recorded on OBS D and G showing refractions at far offsets. A static time shift has been applied to flatten the direct arrival.

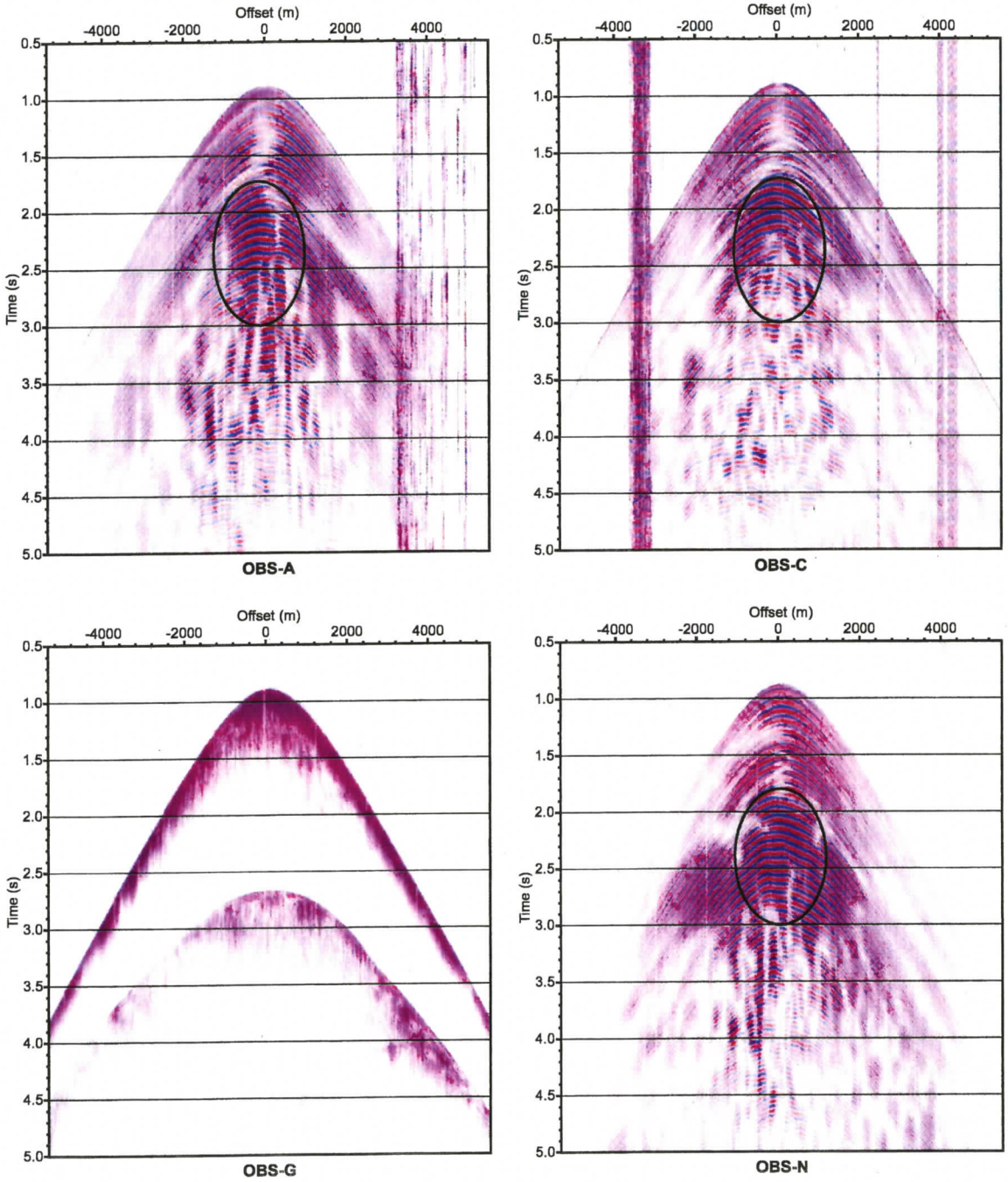

Figure 2.14: Horizontal components from OBS A, C, G and N. The presence of shear wave arrivals is evident on OBS A, C and N below the P-wave BSR, which occurs at $\sim$ 1.15 s at near offset. Shear waves as indicated by ellipses are particularly strong from $\sim$ 2-2.5 s at near offset.

absent which may be explained as strong attenuation of P-waves below BSR due to the presence of free gas. However, S-waves are insensitive to gas and are very useful in areas where P-waves are not recorded. In chapter 6, S-waves are used to investigate structures below the BSR.

2.2.1 OBS relocation

Although the deployment position of an OBS on the sea surface is known with high accuracy, its actual rest point on the sea floor is not well known. While sinking to the sea floor, the OBS can drift by several hundred meters from the point of deployment depending on the water depth and the current speed. Although the depth of the seafloor is constrained by bathymetry data, an accurate water depth at the final position of the OBS is not known. The shot positions recorded from the ship have an uncertainty of the order of tens of meters. Also, the time drift of the clock is assumed to be very small and linear with time, which may not be a valid assumption and may contribute to the error in the seismic data. Thus the the OBS position, clock drift and the shot locations need to be known more precisely in order to get a better model of the subsurface.

The OBS relocation problem is similar to the determination of hypocenter location and source time in earthquake studies. It is an inverse problem in which the objective is to find the seafloor location of the OBS and a time correction that minimize the error between the observed and calculated traveltimes of the seismic signal through the water column. Several OBS relocation procedures exist that utilize the traveltimes through the water column to estimate the true OBS location. *Shiobara et al.* (1997) attempted to find the OBS position from slant range data, ship position data and 1D water velocity structure.

Tolstoy et al. (1993) used a grid method to determine OBS location/clock corrections. *Creager et al.* (1982) inverted for both OBS position and shot locations. *West* (2001) inverted for OBS position, clock offset and clock drift rate. *Hobro* (1999) developed a regularized inversion method to invert for OBS position and shot locations.

For a typical OBS survey with n_s number of shots recorded by n_r of receivers, the number of traveltime data is

$$N_{data} = n_s n_r \tag{2.1}$$

Since the depth of the seismic source is approximately constant, the number of free parameters is

$$N_{param} = 2n_s + 3n_r \tag{2.2}$$

For the present study the source-receiver localization (SRL) scheme of *Zykov* (2006) was used. It is similar to the method of *Hobro* (1999), but it also solves for the GPS clock drift. *Zykov* (2006) argued that the SRL problem is ill-conditioned since OBSs are concentrated in a very small area compared to the shot geometry. The azimuths from far offset shots to the OBSs are concentrated in a narrow sector and this causes instability in the solution. Therefore, the method uses a regularized inversion approach[1] by incorporating *a priori* information into the solution. The model parameters (such as the shot and receiver positions) were regularized with a prior estimate and uncertainty. Also, smoothness constraints were imposed on the shot positions by assuming small curvature of the shot lines.

Direct arrival traveltimes were used for the source-receiver localization. Traveltimes

[1]The concept of regularization is explained in Section 4.2.4.

through the water column were obtained from all the shots by picking the first zero crossing. An uncertainty value of 2 ms was assigned to all the picks. Except for OBS D, all the other OBSs recorded signals for the full duration of the experiment i.e., about 7190 shots. OBS D recorded about 3400 shots. The total number of arrival times used in the inversion is 67736. The parameters estimated in the inversion were the (a) x, y, z coordinates of the OBSs, (b) x, y coordinates of the shots, (c) sound speed profile bias and (d) GPS clock drift of the internal clock of the OBS. The depth of the shots was assumed to be constant throughout the experiment. The sound speed profile through the water column can change laterally by up to $\pm$ 2 m/s and for shots at large offsets this may lead to traveltime errors of up to $\pm$ 4 ms that may significantly affect the localization result (*Zykov* 2006). The drift rate of the OBS clock may be constant or may change in the middle of the experiment. To examine this effect, the inversion was done with and without solving for the clock drift. Following *Zykov* (2006), uncertainties to the initial model paramaters were assigned as given in Table 2.2.

Table 2.2: Initial model parameter uncertainties for the SRL problem

Model parameters	Uncertainty
Shot (x, y)	$\pm$ 15 m
OBS (x, y)	$\pm$ 200 m
OBS (z)	$\pm$ 5 m
Sound speed bias	$\pm$ 2 m/s

First, the localization was attempted under the assumption that there is no internal clock drift. The inversion converged after 4 iterations with a normalized χ^2 value of 0.88. However, the traveltime residuals for some of the OBSs were larger than 6 ms as shown in Figure 2.15. The higher residual values seem to arise from shots at near offsets.

The effect of clock drift was then examined by including the drift function in the inversion. Since there is no definite drift pattern found from the above inversion, a linear drift function $t_{drift} = b + kT$ was assumed for the whole duration of the survey, where T is the shot instant time at the beginning of the survey, b is the drift at the beginning and k is the drift rate. The coefficients b and k were solved during the inversion. Convergence was achieved after 4 iterations with a normalized χ^2 value of 0.22. Traveltime residual values were generally less than 2 ms, which were comparable to the picking error of the direct arrival traveltimes. The RMS change of the shot positions was 2.49 m. The recovered depths were compared with the depths from the bathymetry data (Table 2.3). The average error in depth from the inversion is less than 1%. The OBS clock drifts obtained from the inversion are in addition to the drift measured after their recovery. OBS B showed the maximum clock drift, but the drift rate for OBS A was highest at about 6 ms/day. Figure 2.16 shows the traveltime residual and the clock drift for all the ten OBSs. Figure 2.17 shows the relocated OBS positions.

Table 2.3: Depth of the OBSs at the deployed position as recorded in the ship and the recovered depths from the inversion.

OBS	Depth from bathymetry (m)	Recovered depth (m)	Error (m)
A	1318	1308.4	-9.6
B	1316	1308.6	-7.4
C	1314.3	1307.8	-6.5
D	1314.2	1307.7	-6.5
G	1314	1306.6	-7.4
H	1313.4	1304.3	-9.1
I	1311	1302.3	-8.7
K	1310	1301.5	-8.5
L	1308	1302.2	-5.8
N	1305	1301.5	-3.5

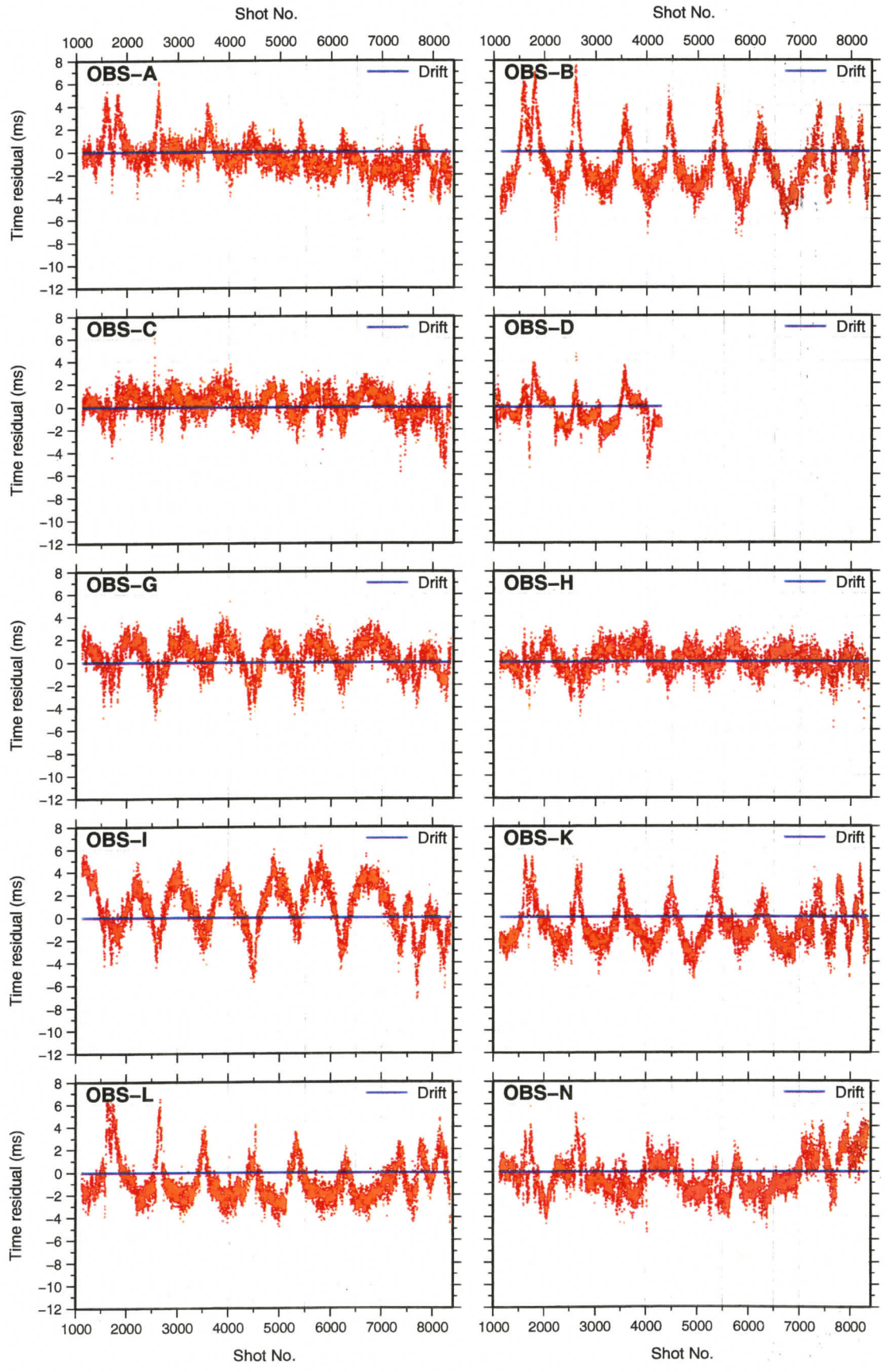

Figure 2.15: Traveltime residual after inversion without solving for clock drift. Only clock drift measured at OBS recovery has been applied.

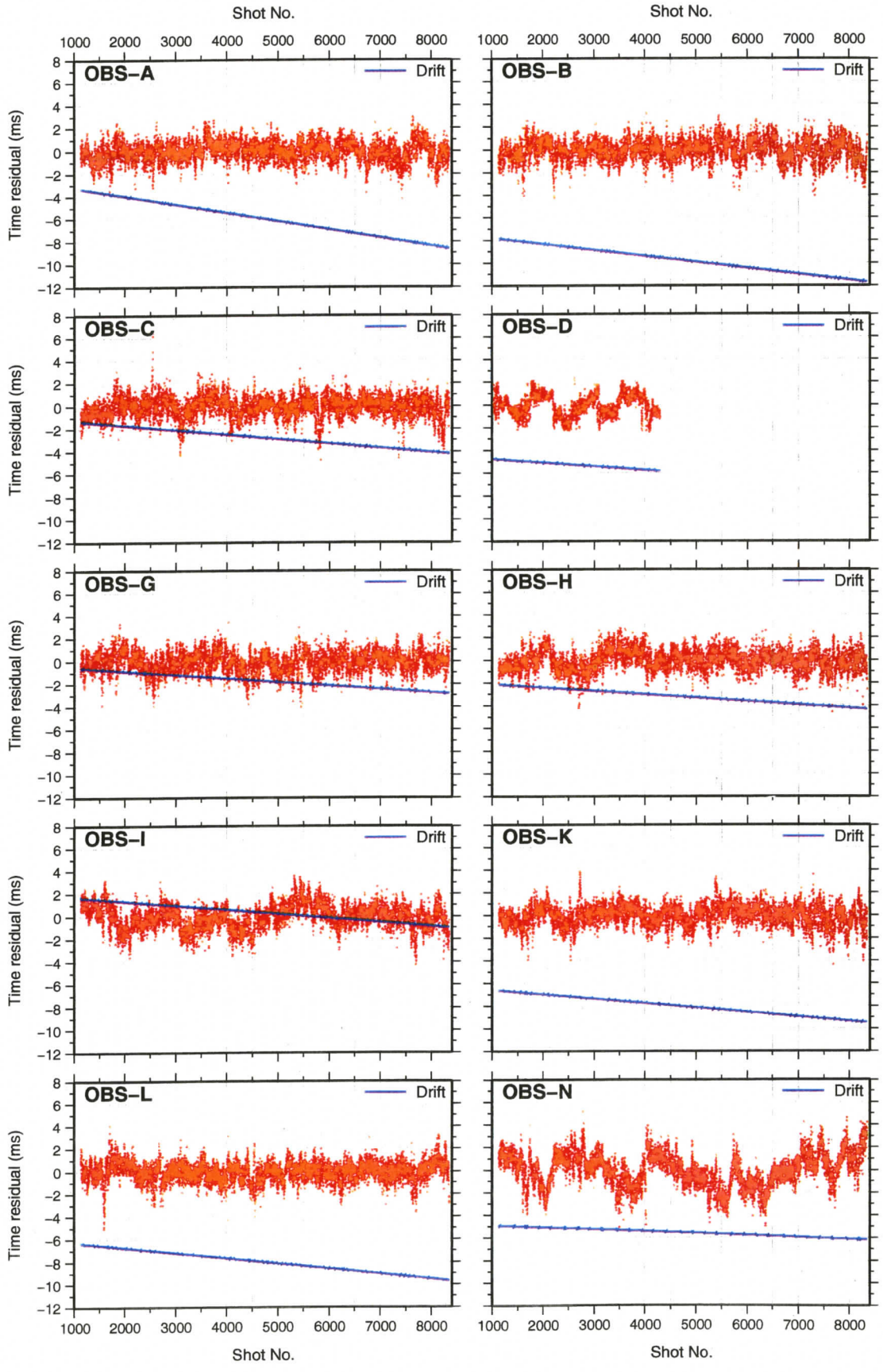

Figure 2.16: Traveltime residual and the recovered clock drift after inversion.

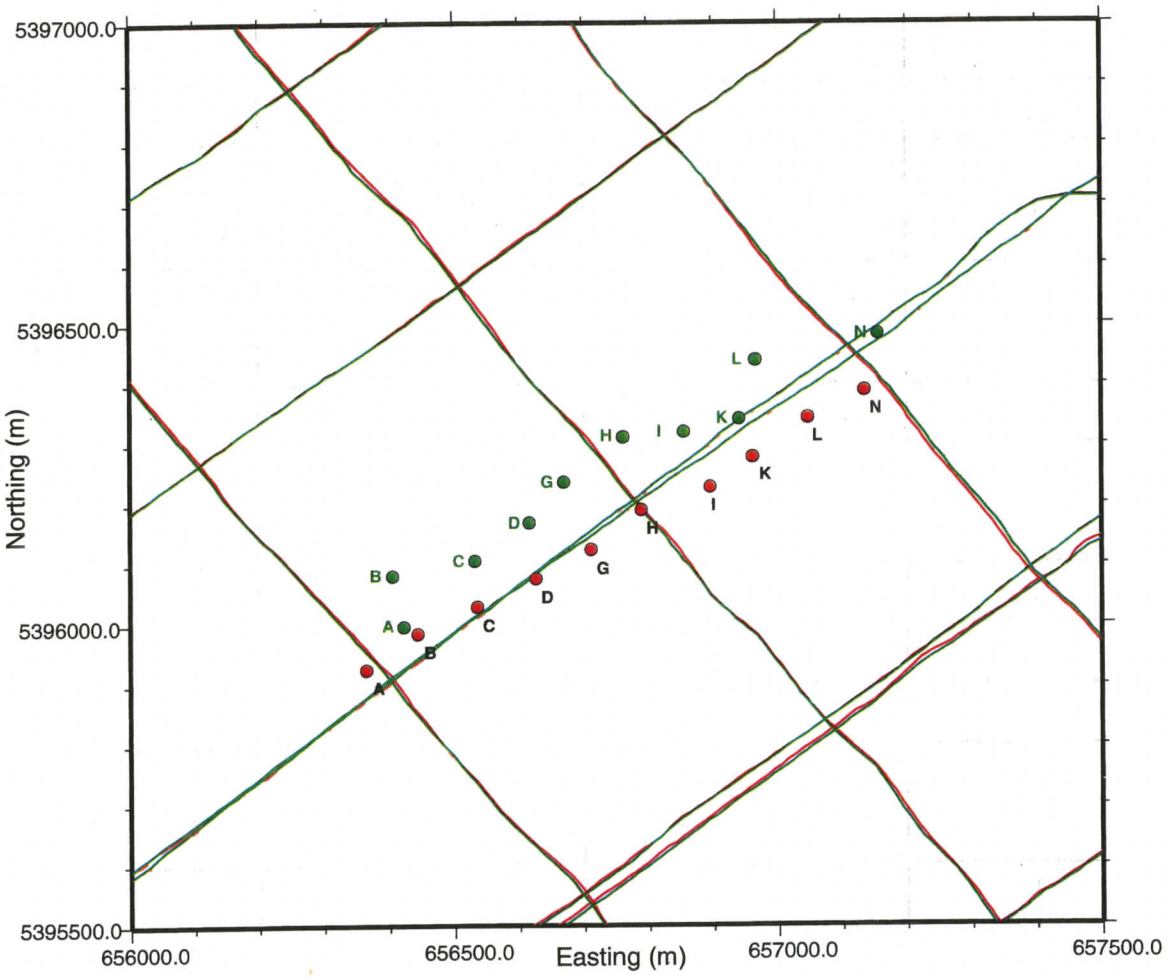

Figure 2.17: The relocated shot and receiver positions (in green) plotted with the original shot and receiver positions (in red).

Chapter 3

Mirror imaging: Migration of OBS data

3.1 Introduction

Ocean Bottom Seismometers (OBSs) are multicomponent receivers that are increasingly being used for marine seismic studies. A typical OBS records four components of the seismic wavefield: one hydrophone (pressure) component, and one vertical and two horizontal geophones that record the ground velocity (or acceleration). Recording of the seismic wavefield at the seafloor using OBSs has several advantages over the conventional near surface recording (*Caldwell* 1999). Due to their deployment on the ocean floor, OBSs are less vulnerable to noises/disturbances in the water column and so have a relatively higher signal/noise ratio. OBSs offer wide-azimuth geometry which is important for imaging under complex overburden such as salt domes as well as for the analysis of angle-dependent reflectivity. While it is impossible to record shear waves in conventional surface streamer surveys, multicomponent marine data hold much information about the shear velocities (recorded by the horizontal geophone components) down to subseafloor depths of several kilometers. Because shear wave velocities and wavelengths can be very

small for soft sediments, the vertical resolution of shallow sediment layers obtained from shear waves (i.e., converted waves) can be much higher than that obtained from P-waves alone (*Backus et al.* 2006).

However, OBS data acquisition and processing have their share of difficulties. For example, inadequate coupling of OBS sensors with the ocean bottom can cause signal distortion. To reduce the coupling effects it is important to have the sensors rigidly positioned into more consolidated sediments, which is often not feasible in practice. Secondly, due to the high cost of acquisition, OBS data density is often sparse. Sparse OBS geometry produces poor illumination, especially for reflectors whose depth under the seafloor is less than the OBS spacing. Thirdly, it is often difficult to image the seafloor profile using OBS data alone since the primary arrivals do not contain reflections from the ocean bottom. Also, conventional OBS imaging from primary arrivals fail to image shallow reflectors just beneath the seafloor and the problem is worse for sparse OBS spacing. In this chapter, a new method of imaging is described that utilizes multiples from OBS to image the shallow structure beneath the seafloor[1].

3.2 OBS tilt estimation and correction

OBS multicomponent recording involves vector measurement of the seismic wavefield. Faithful recording of different vector components (or, *vector fidelity*), assuming a Cartesian coordinate system, requires that particle motion on one axis should produce an accurate response on that axis and no response on the other two orthogonal axes. To achieve vector fidelity of the multicomponent data, the sensors must be properly oriented so

[1]All the results of this chapter are produced by R. Dash using in house seismic imaging software of CGGVeritas.

that the vertical component of the geophone records only the vertical particle motion (i.e., mostly P-waves) and the horizontal components measure the particle motions in the two orthogonal directions. Also, for S-wave studies (e.g., anisotropic studies), one of the horizontal components should be oriented along the shot line (Fig. 3.1a). But ideal orientation is rarely achieved in practice as the OBS deployment is often done by allowing the OBS to free-fall from the ocean surface (Fig. 3.1b). Therefore additional processing is required to correct for orientation effects.

For a gimballed type OBS, the vertical geophone is guaranteed to measure the vertical component of the particle motion. P-waves are recorded mainly on the vertical component and shear waves mainly on the horizontal components. For a non-gimballed type OBS, as the ones used in this study, the tilt effect (angle between the vertical component and true vertical) can be significant. A tilted OBS can record S-waves in the assumed vertical component making the interpretation difficult.

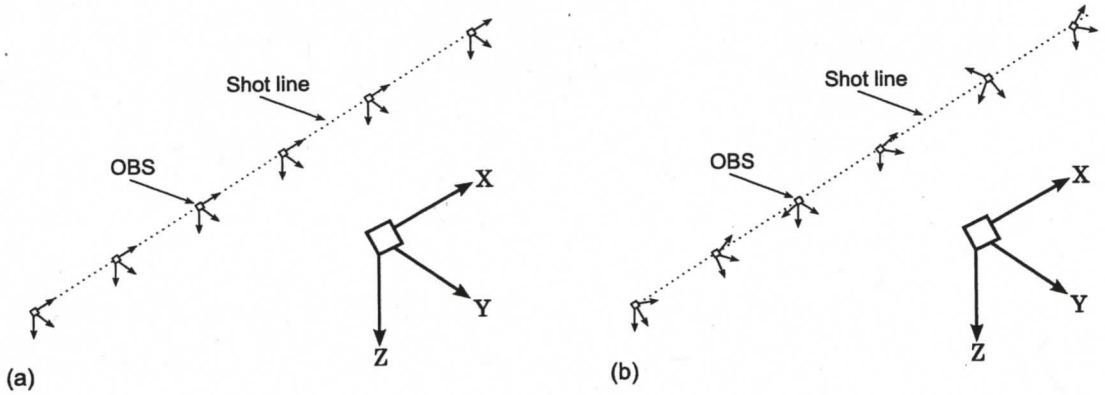

Figure 3.1: Orientation of the horizontal and vertical geophone components in the acquisition coordinate system. For an ideal case, the inline x-component points towards the positive shot line direction (a). In practice, geophone components are directed arbitrarily and the orientation varies from station to station (b).

Under the multicomponent acquisition coordinate system, the three geophone components are termed as inline, crossline and vertical components corresponding to their

orientation along x, y, and z direction, respectively. Assuming a right-handed coordinate system, the inline component is aligned with the shot line, the crossline line component is directed 90° towards the right and the vertical component is downward.

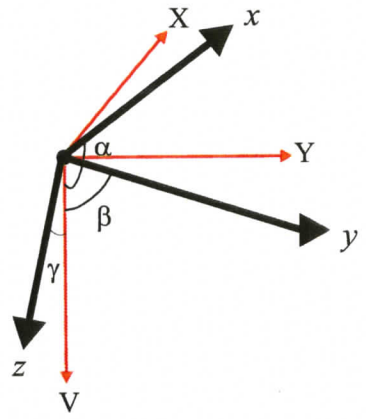

Figure 3.2: Tilt angles for a three-component geophone.

OBS tilt and orientation angles for this study are estimated using the vertical orientation rotation (VOR) and the horizontal orientation rotation (HOR) methods of *Li et al.* (2004) and *Li and Ronen* (2005). A set of angles α, β and γ (where α, β and γ are the angles of the three orthogonal axes with true vertical as shown in Figure 3.2) are obtained that are best to remove the tilt effect from the data. Following the convention of *Li and Ronen* (2005), the axes of the tilted OBS (x, y, z) are related to the true axes (X, Y, V) as follows:

$$\begin{pmatrix} X \\ Y \\ V \end{pmatrix} = \begin{pmatrix} sin\alpha & -\frac{cos\alpha cos\beta}{sin\alpha} & -\frac{cos\alpha cos\gamma}{sin\alpha} \\ 0 & \frac{cos\gamma}{sin\alpha} & -\frac{cos\beta}{sin\alpha} \\ cos\alpha & cos\beta & cos\gamma \end{pmatrix} \begin{pmatrix} x \\ y \\ z \end{pmatrix} \tag{3.1}$$

Accordingly, the data recorded with a tilted receiver can be transformed to the data for an equivalent vertically planted receiver once the tilt angles α, β and γ are known.

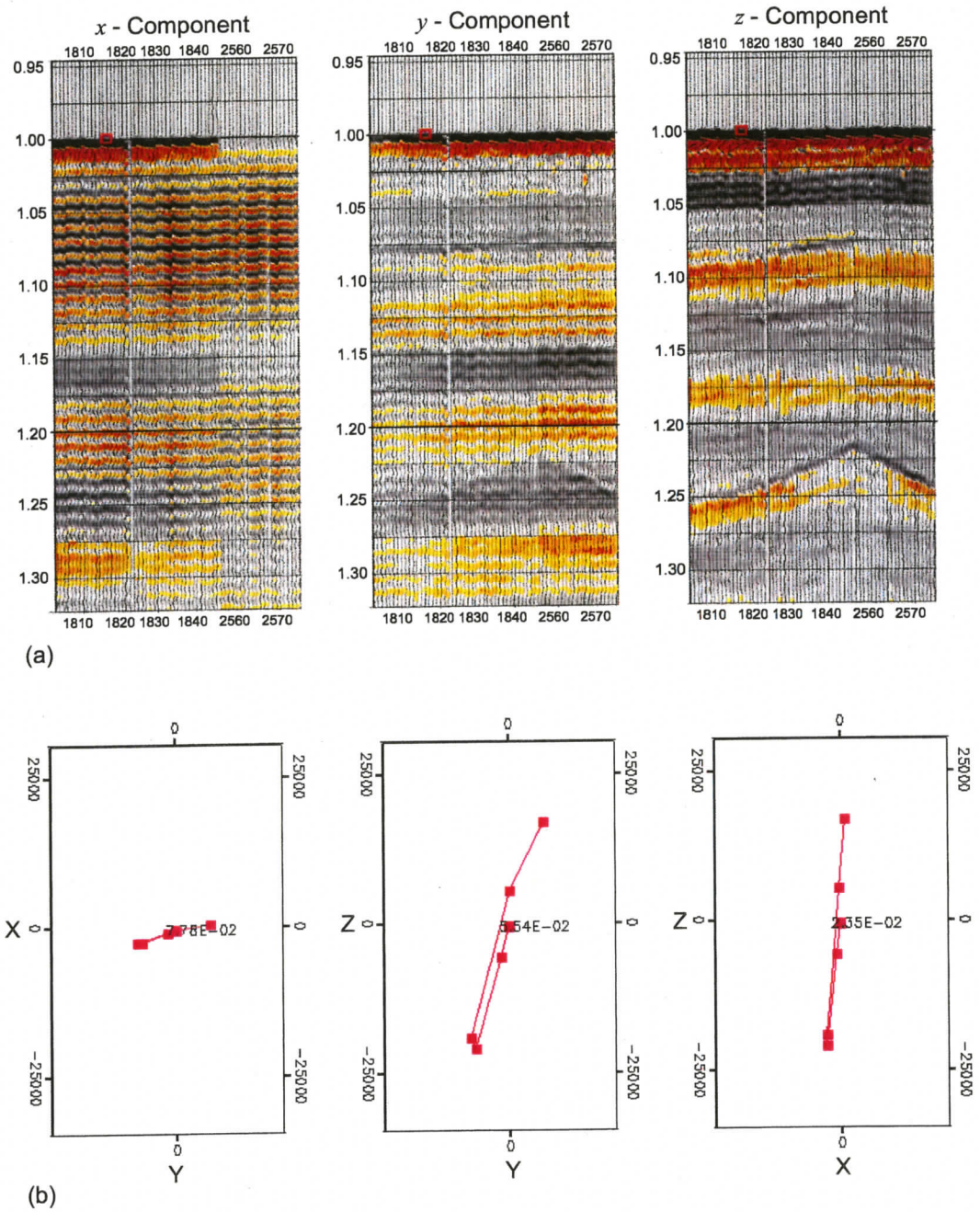

Figure 3.3: Tilt angle estimation for OBS-C. (a) display of original $x-, y-$ and $z-$ component data. The data have been linearly moved out using the water velocity. (b) hodogram of the $x-y$, $z-y$ and $z-x$ components over 6 samples.

To determine the tilt angles, the orientation angle θ_i of the OBS (the angle between the assumed inline component and north measured clockwise, or the azimuth of the assumed

inline component) from each shot i is computed by fitting a line to the hodogram of the direct arrivals from the two horizontal components x and y (Fig. 3.3b). Ideally, the orientation angle should be independent of the source-receiver azimuth and all shots should give the same orientation angle. However θ_i can be inconsistent if (1) the OBS is tilted, (2) the OBS is rotated in the middle of the survey due to oceanic currents or other environmental effects and (3) the first breaks are not radial (Shuki Ronen, *personal communication*, 2007). The average orientation angle over all the shots is

$$\overline{\theta} = \frac{1}{N}\sum_{i=1}^{N}\theta_i \tag{3.2}$$

The angles α, β and γ are chosen such that the standard deviation

$$\sigma = \sqrt{\frac{1}{N}\sum_{i=1}^{N}\left(\theta_i - \overline{\theta}\right)^2} \tag{3.3}$$

is minimum. Figure 3.4a shows the contour plot of the standard deviation σ for different values of α and β. The receiver orientation after tilt correction is shown in Figure 3.4b.

After the tilt correction, horizontal orientation rotation was applied to the OBS that involves rotation of inline and crossline components were rotated horizontally to the radial and transverse directions. Table 3.1 shows the tilt and orientation angles for different receivers. The radial geophone component represents horizontal particle motion along the source-receiver plane and the transverse component records horizontal particle motion perpendicular to the radial response. Figure 3.5 shows the three components of OBS-A before tilt correction and Figure 3.6 after rotation. Out of the ten receivers, only seven were found to have tilts less than 10°. OBS-G, H and L have much larger tilt angles, which

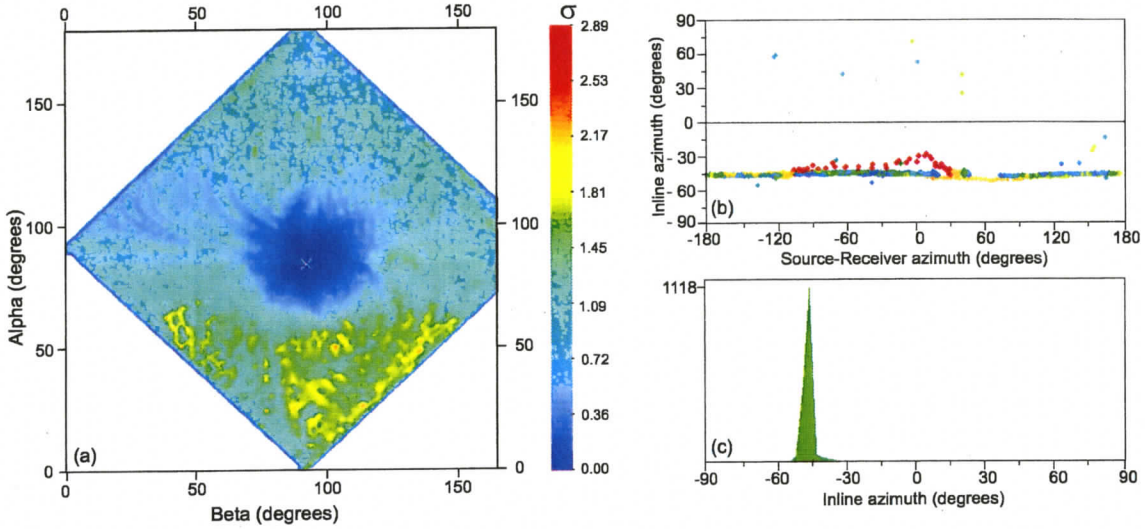

Figure 3.4: Tilt angle estimation for OBS-C. (a) standard deviation σ as a function of α and β used to pick the tilt angle. The X marks the minimum value of the standard deviation σ. (b) crossplot of the inline azimuth against shot-receiver azimuth after tilt correction. (c) histogram plot showing number of orientation angles for an azimuth bin.

may be due to wrongly wired sensors. These OBSs were not used for further analysis.

Table 3.1: Estimated tilt angles for the OBS (in degrees).

OBS	tilt (γ)	α	β	inline azimuth
A	7.85	88.16	97.63	123
B	5.45	93.45	94.21	114.48
C	5.87	84.71	92.54	133.26
D	6.91	91.15	83.19	68.3
G	23.63	101.81	69.84	19.16
H	48.13	133.09	107.24	16.35
I	1.81	89.71	91.79	148
K	4.10	87.48	86.77	105.9
L	16.28	74.86	95.84	7.16
N	2.0	92	90.5	136.26

3.3 Wavefield separation

The seismic wavefield that carries information about the subsurface arrives at the OBS from below (upgoing wavefield) while the initial source signal arrives at the OBS

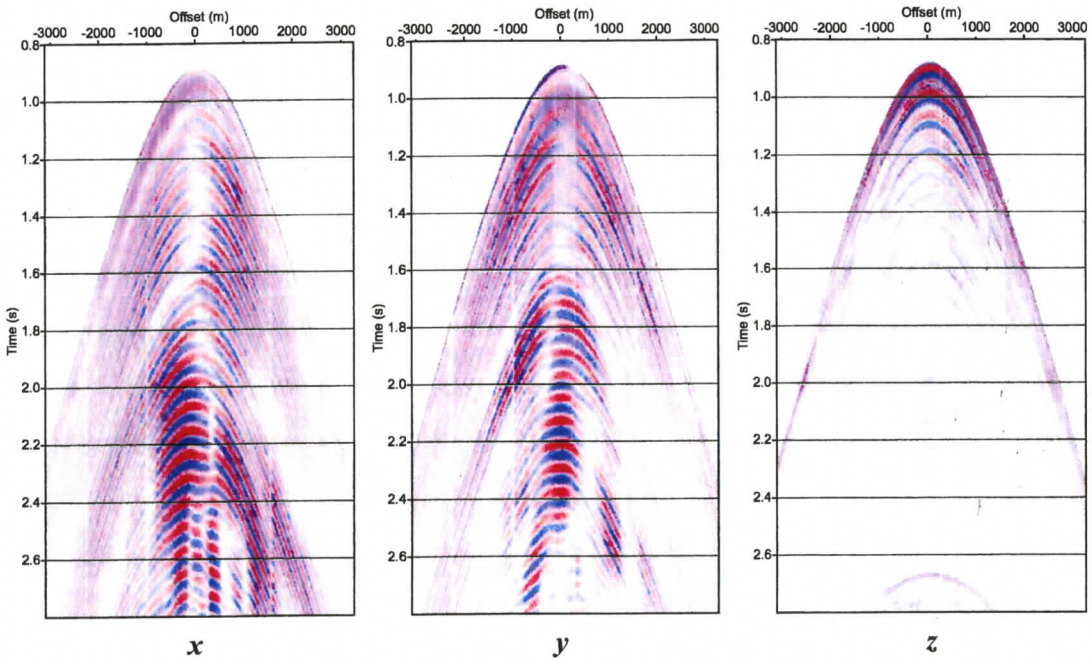

Figure 3.5: Horizontal and vertical components of OBS-A before tilt and horizontal orientation rotation.

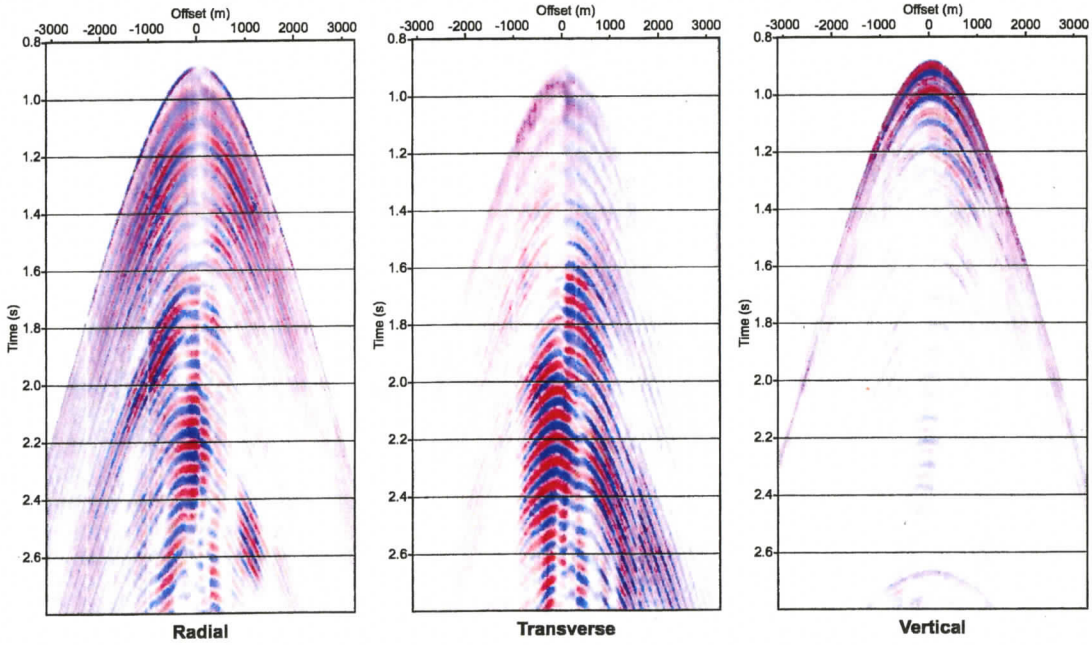

Figure 3.6: Horizontal and vertical components of OBS-A after tilt and horizontal orientation rotation.

from above (downgoing wavefield). However, both the up- and downgoing wavefields are contaminated by multiples. While pure water reverberations and receiver side multiples are contained in the downgoing wavefield, the source side multiples are present in the upgoing wavefield (Fig. 3.7). The receiver side multiples are reflected from the water surface immediately before reaching the OBS. In the last decade, numerous schemes have been developed to separate the up- and downgoing wavefields and to eliminate the multiples from primary reflections by combining different components of the seismic wavefield (*Barr and Sanders* 1989, *Hoffe and Cary* 2000, *Schalkwijk et al.* 2001).

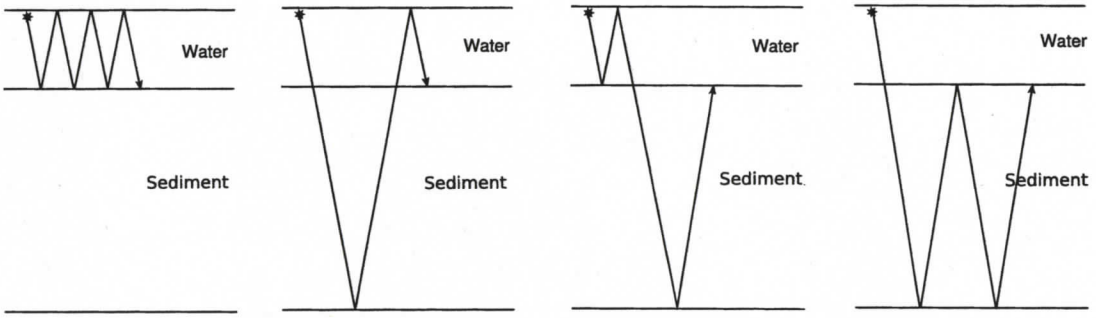

Figure 3.7: Source and receiver side multiples recorded on ocean bottom receivers.

Schneider et al. (1964) first recognized that simultaneous measurement of pressure and ground velocity on the ocean bottom can attenuate water layer multiples. The approach takes into account the polarity of the upgoing and downgoing wavefields recorded on the hydrophone and the vertical geophone. While the upgoing wavefield has the same polarity on the hydrophone and the vertical geophone, the downgoing wave is recorded with opposite polarity. This is because the pressure is a scalar quantity and so does not depend on the direction of wave propagation whereas the geophone records the ground velocity, a vector. Therefore, by combining the hydrophone and the vertical geophone data (dual-sensor or PZ summation), the up- and downgoing wavefields can be separated

as:

$$U = \frac{P + \rho cZ}{2}, D = \frac{P - \rho cZ}{2} \tag{3.4}$$

where U is the upgoing wavefield, D the downgoing wavefield, P the pressure as recorded on the hydrophone, Z the particle velocity recorded on the vertical geophone, ρ the density of the subsurface and c the acoustic velocity. ρc is the scaling factor for the geophone to account for the seafloor acoustic impedance. It should be noted that the above equation is valid for near vertical arrivals. The PZ summation must also account for instrument differences, as well as the phase and spectral differences that can be caused by poor coupling, particularly in areas with soft ocean bottoms. Thus, before attempting wavefield separation, it is crucial to scale the geophone and hydrophone to match their amplitude and phase responses.

While doing wavefield decomposition, the distinction should be made between the wavefield above and below the seafloor. This is because the pressure is continuous across the sea-bottom interface, but its up- and downgoing parts are in general not (*Grion et al.* 2007). Also, wavefield decomposition above and below the seafloor is useful for S-wave studies. While a decomposition just above the seafloor (i.e., in the water) gives up- and downgoing pressure wavefields, a decomposition just below the seafloor (i.e., in the solid) can provide up- and downgoing P- and S-wave potentials (*Schalkwijk* 2001). However, only P-waves are considered for the present study. Immediately above the seafloor, the downgoing component contains the direct arrival and the receiver ghosts (receiver-side multiples) while the upgoing component contains the primaries and free-surface (source-side) multiples. Immediately beneath the seafloor, the direct arrival, the receiver side

water layer reverberation and the water bottom reflection are recorded as downgoing waves while the primaries are recorded as upgoing. Primaries and interbed multiples are recorded as upgoing waves both above and below the seafloor.

After proper scaling and wavelet processing, the up- and downgoing wavefields just above the seafloor are:

$$\begin{aligned} U_+ &= P + Z \\ D_+ &= P - Z \end{aligned} \tag{3.5}$$

The above relation assumes near vertical propagation and the vertical particle velocity is scaled by the water impedance. Similarly, the up- and downgoing wavefields just below the seafloor are:

$$U_- = P + KZ \tag{3.6}$$

$$D_- = P - KZ; \tag{3.7}$$

$$K = \frac{1+R}{1-R}$$

where K is the seafloor acoustic impedance and R is the seafloor reflection coefficient.

To remove the bubble pulse, gap deconvolution with a 12-ms gap length and 300-ms filter length was applied to the hydrophone and vertical component data. Amplitude calibration of the pressure components was applied to compensate for variations in the amplitude across the receivers. PZ calibration was applied before the wavefield separation. Figure 3.8 shows the up- and downgoing wavefields above and below the seafloor. The

main target area in the vertical component data (including the BSR) lies within the 300 ms two-way time below the seafloor.

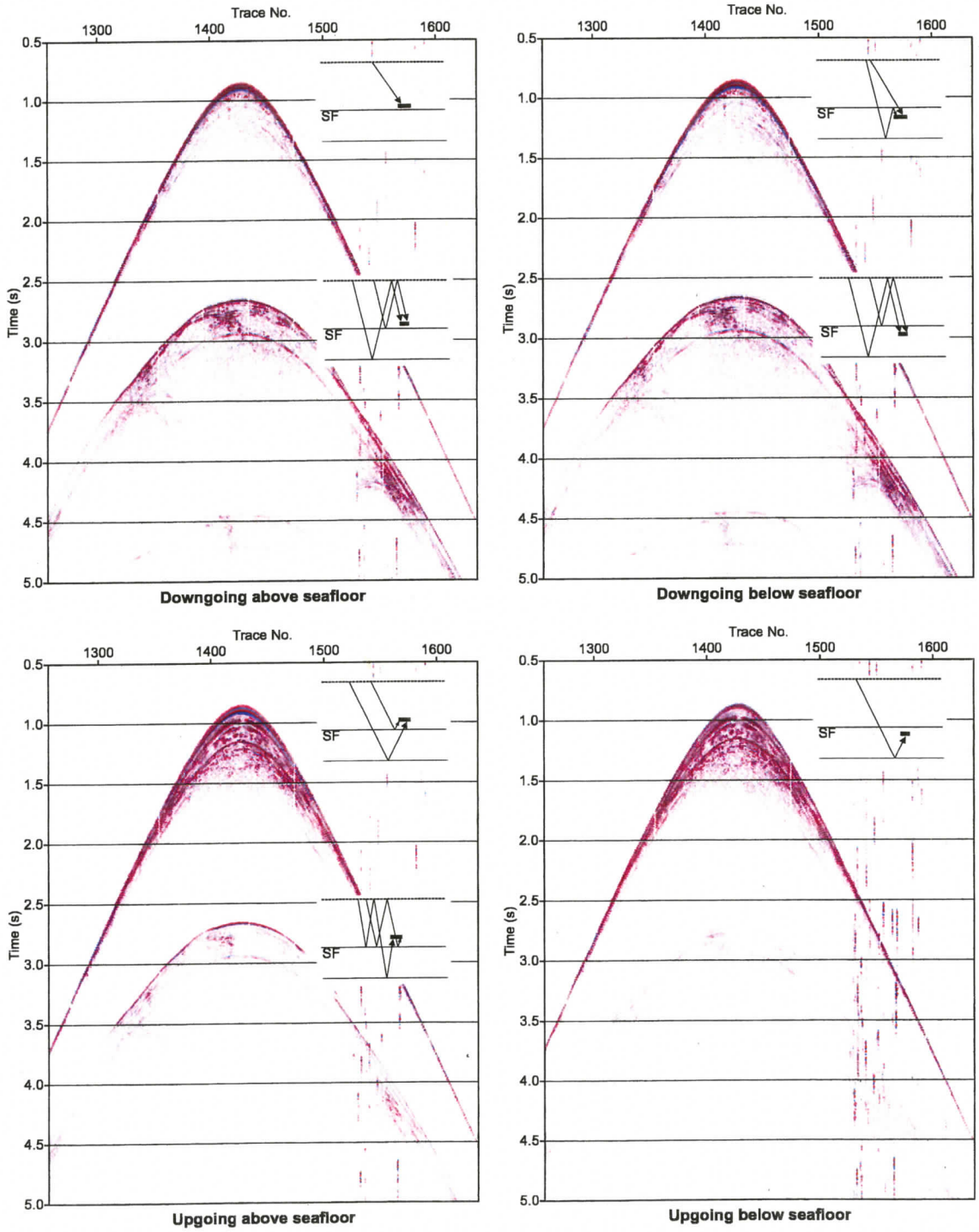

Figure 3.8: Up- and downgoing wavefields recorded at OBS-A.

3.4 Migration of OBS data

Seismic migration from OBS data is usually done using the upgoing primary reflections. The upgoing wavefield below the seafloor is preferred over the upgoing wavefield above the seafloor since the latter is contaminated with water layer reverberations. The upgoing wavefield beneath the seafloor, calculated using equation 3.6, is shown in Figure 3.9. However, migration of upgoing primary wavefield is not the best option for a sparse receiver geometry. In such cases, OBS multiples can provide a better structural image of the subsurface from a wider angle (Fig. 3.10) and thus can be used for migration. Several authors have used the receiver-side multiples in the downgoing wavefield in migration (*Godfrey et al.* 1998, *Grion et al.* 2007, *Jiang et al.* 2005, *Ronen et al.* 2005, *Pica et al.* 2006). The migration using the receiver-side ghosts is called mirror-imaging because the sea surface acts as a mirror reflecting the upgoing wavefield back to the receiver.

The present study follows the method of *Ronen et al.* (2005). Seismic data from shotline 3 (Fig. 2.7) recorded on seven OBSs were used for the migration. Kirchhoff depth migration was applied to the upgoing, primary wavefield below the seafloor and the downgoing multiples above the seafloor. The downgoing wavefields above the seafloor were calculated using equation 3.5. The same OBSs were selected that were used for migration of the upgoing wavefield beneath the seafloor (Fig. 3.11).

3.4.1 Kirchhoff migration

Kirchhoff migration assumes that a reflector can be constructed by the summation of many diffractors. The basic steps are traveltime (total time from source to diffractor and

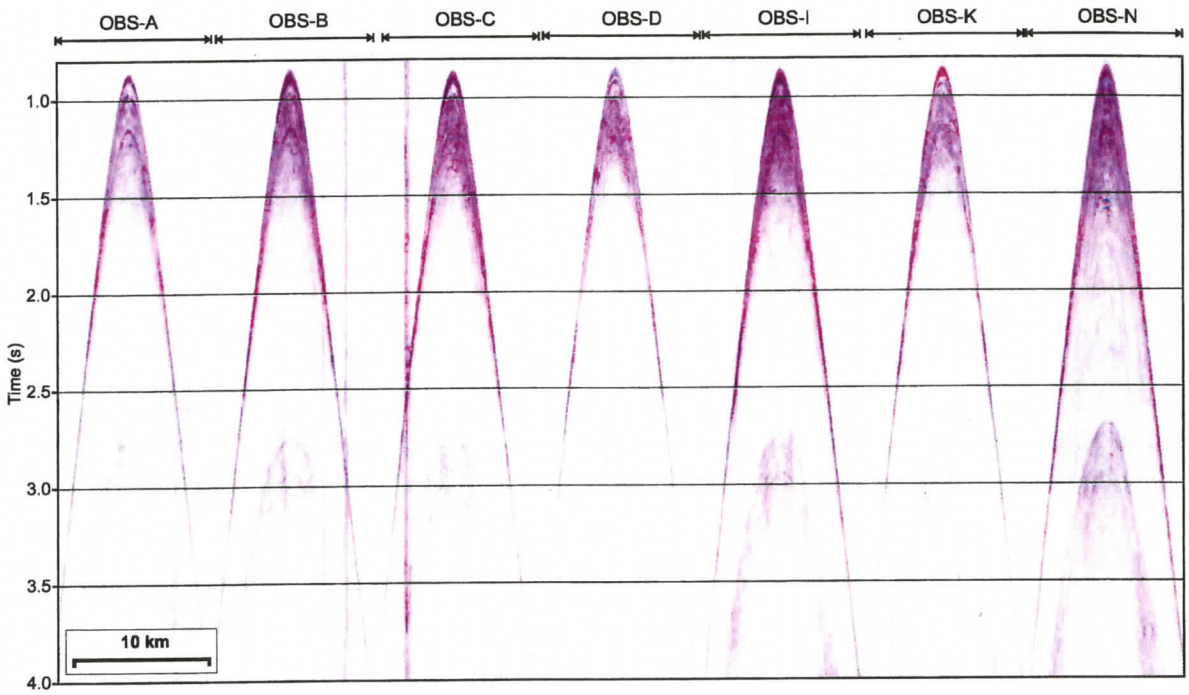

Figure 3.9: Upgoing wavefield below seafloor from OBS A, B, C, D, I, K and N as input data for the conventional migration.

back) computation and imaging. Trace amplitudes are mapped along the paths of equal traveltime or isochrons. A single weighted amplitude of a trace is mapped into all possible grid points along the traveltime isochron. A reflector is then constructed along the tangent of the total travel time isochrons. While Kirchhoff time migration is more common, it fails in the presence of rapid lateral and vertical velocity variations. Thus Kirchhoff depth migration produces a better result. Traveltime computation requires definition of the velocity field. The velocity model over line 3 was obtained from 2D traveltime tomography of the OBS and single channel reflection data as described in Chapter 6. In the absence of a prior velocity model, ray tracing of the primary and multiples and NMO velocity analysis can provide velocity information for migration. The input velocity model for the mirror migration of downgoing multiples was designed such that the receivers were placed at the sea surface (not on the seafloor) of a water column twice as thick as the original

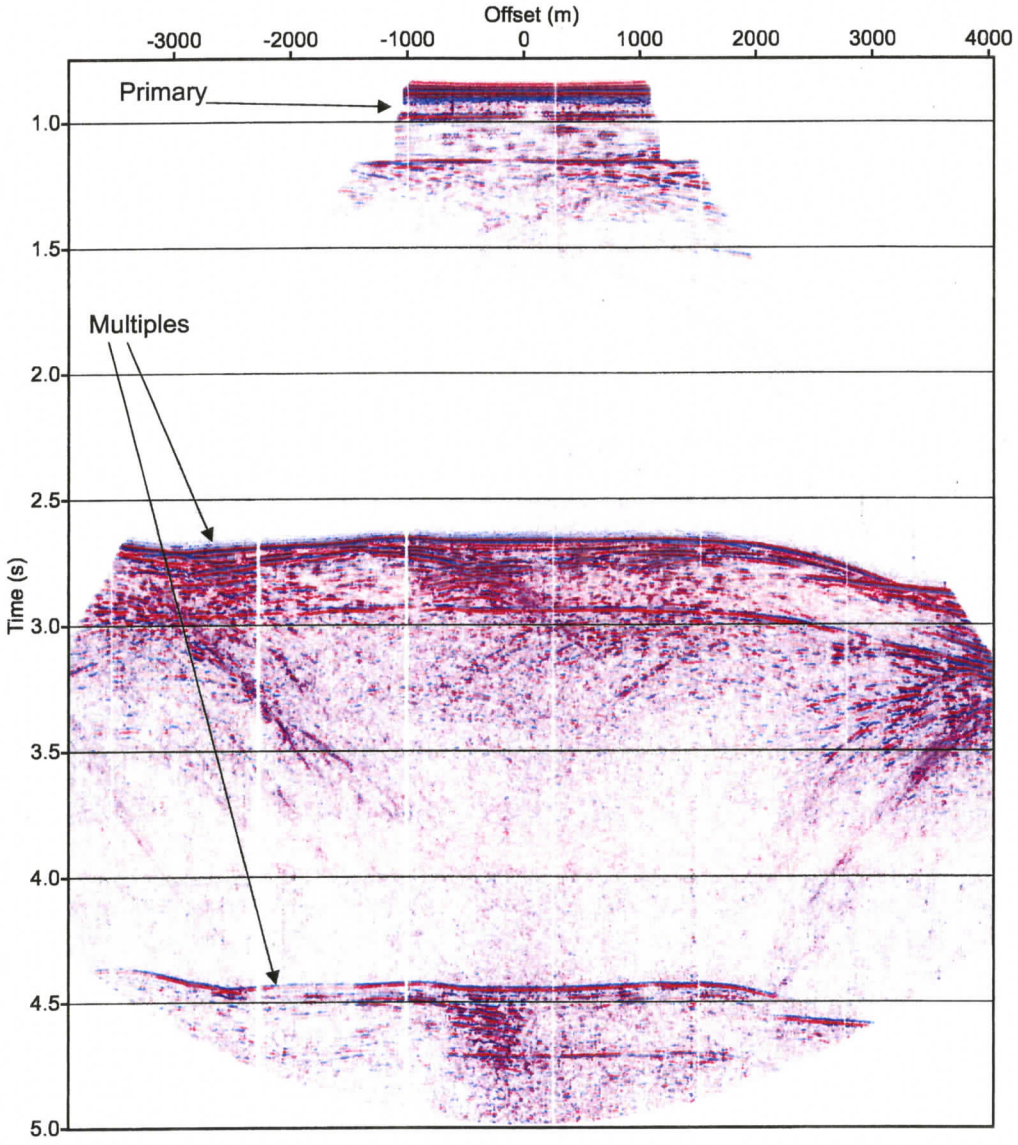

Figure 3.10: Normal moveout (NMO) corrected data from OBS-A (hydrophone) showing the structural information contained in the multiples.

water layer (Fig. 3.12).

First, migration of the upgoing wavefield below the seafloor was attempted. As can be seen from the migration results in Figure 3.13, the illumination is very poor. The seafloor and the shallow reflectors immediately below the seafloor are not imaged. Only reflectors near the BSR are well imaged. However, migration of the downward wavefield above the

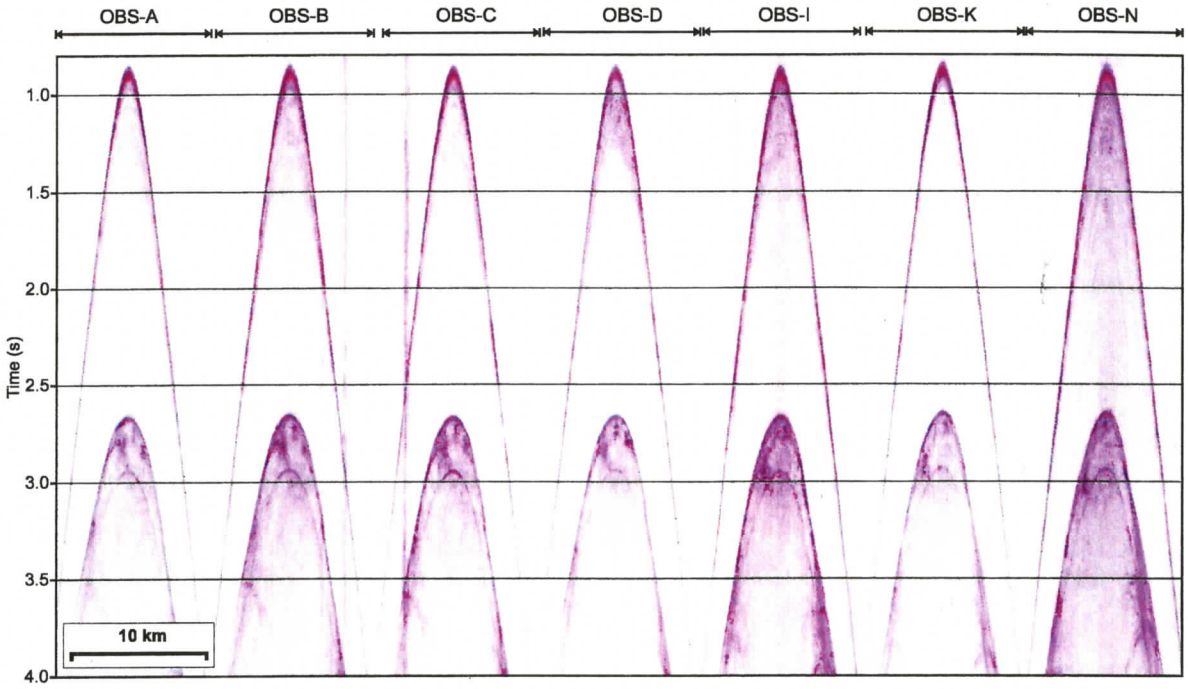

Figure 3.11: Downgoing wavefield above seafloor from OBS A, B, C, D, I, K and N as input data for mirror imaging.

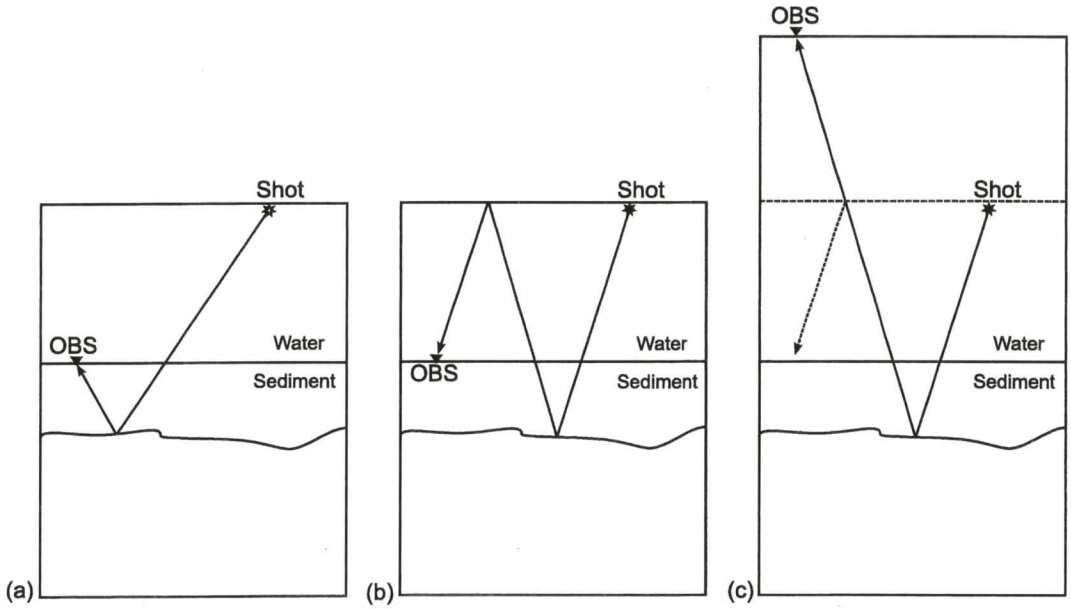

Figure 3.12: Ray paths of upgoing primaries (a) and downgoing multiples (b). The downgoing receiver ghost in (b) can be treated as an upgoing primary reflected downward from the seasurface. For migration, multiples can be treated as primaries assuming that the data is not recorded on the seafloor but above an layer with twice the thickness of the water column (c). The multiples offer extended illumination compared to the primaries.

seafloor using the same migration aperture angle (45°), as shown in Figure 3.14 (input data in Figure 3.11), produces a much better image. The lateral illumination is much enhanced and the shallow layers including the seabed are clearly imaged. *Ronen et al.* (2005) argued that the upgoing waves are more susceptible to the inhomogeneities near the seabed than the downgoing waves. Inhomogeneities near the seabed cause more statics, amplitude variations and scattering of the upgoing waves. However, the downgoing waves travel the water column twice and the scattering/diffractions heal when they reach the receiver. Also in mirror imaging, the receiver is much farther from the seabed anomalies. Mirror imaging using a larger migration aperture angle (70°) produces an image with much wider lateral illumination (Fig. 3.15). In contrast, the migration of the upgoing wavefield using the larger 70° aperture did not improve the original image (Fig. 3.13) with the 45° aperture.

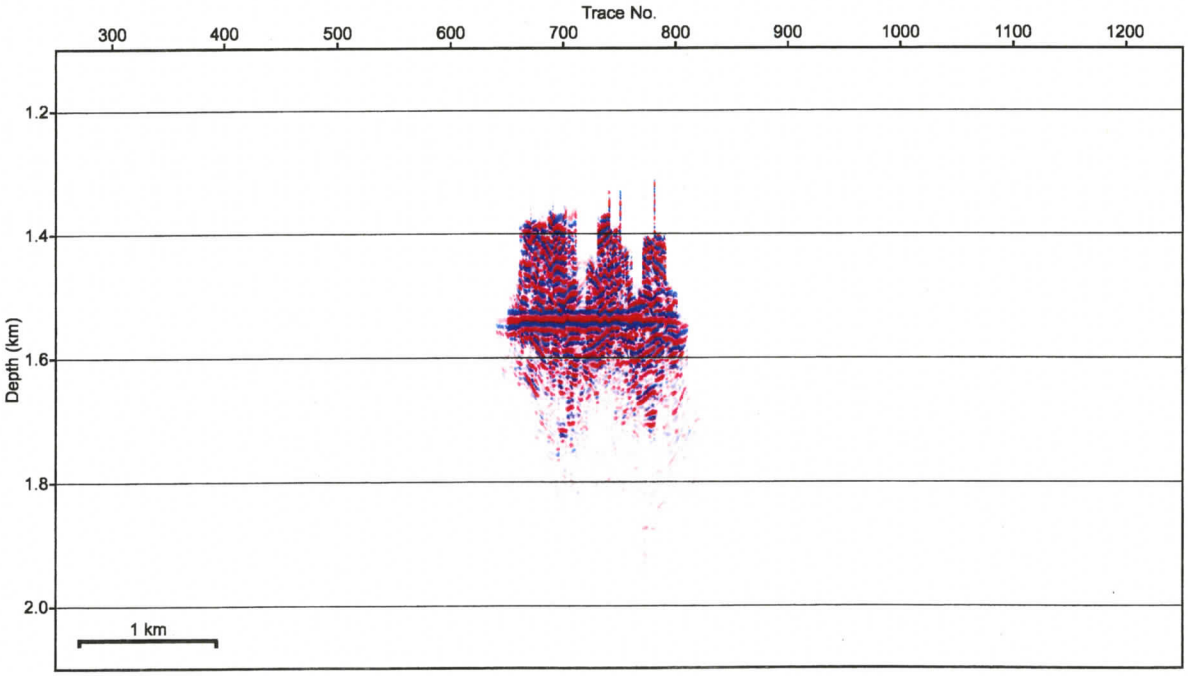

Figure 3.13: Migrated image of the upgoing wavefield below seafloor.

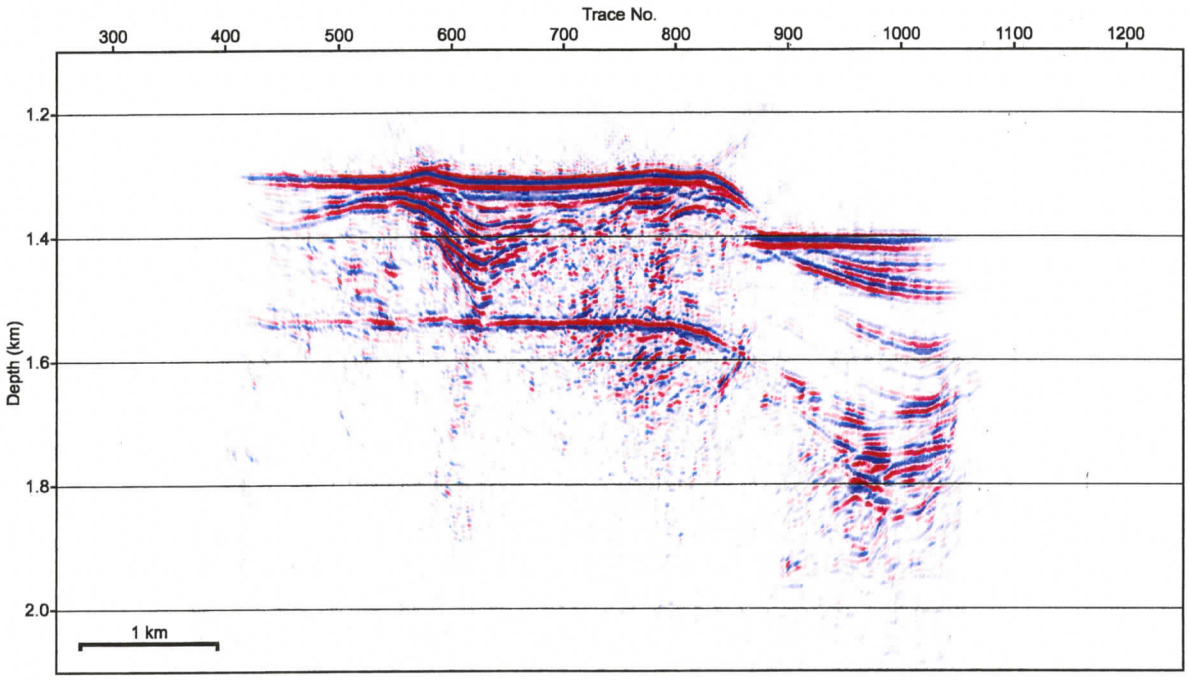

Figure 3.14: Migrated image of the downgoing wavefield above seafloor.

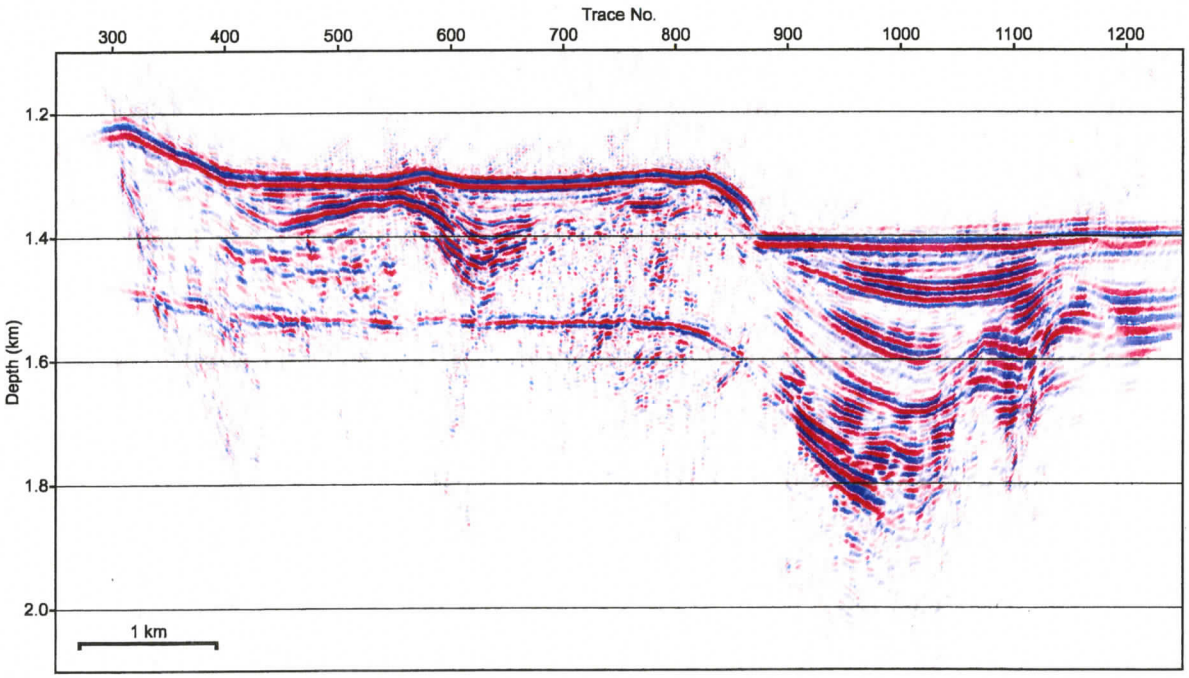

Figure 3.15: Migrated image of the downgoing wavefield above seafloor with larger migration aperture angle.

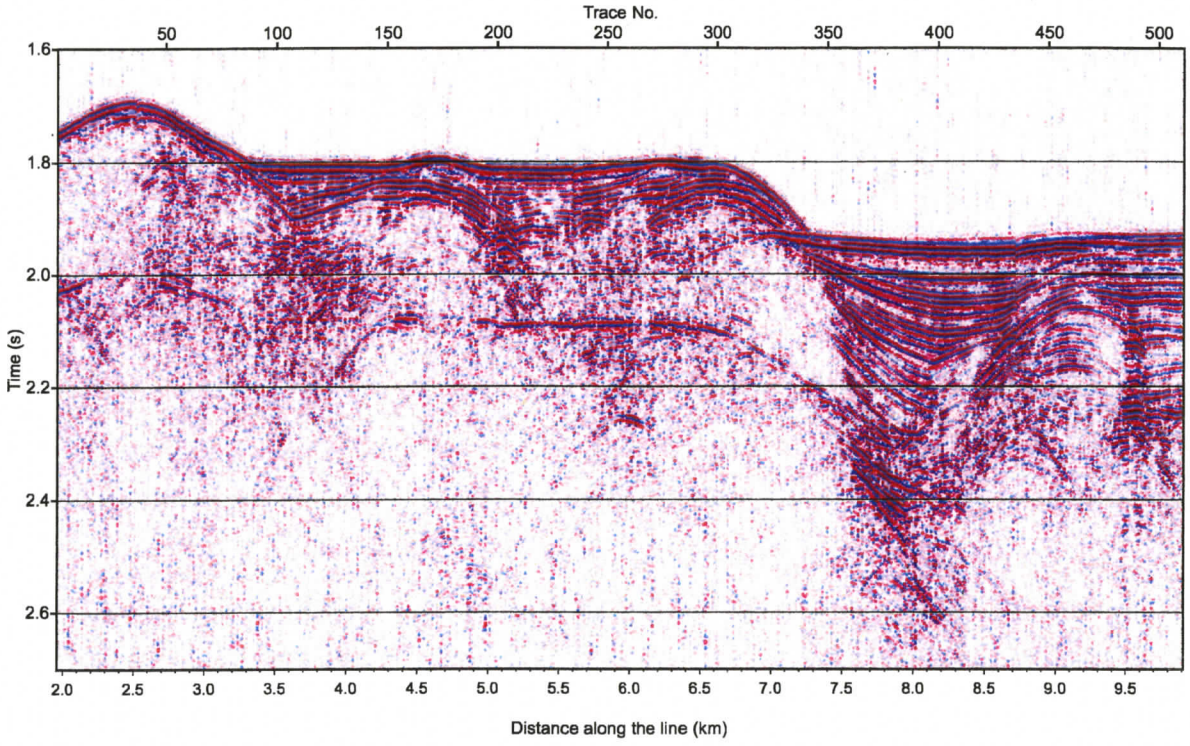

Figure 3.16: Single channel normal-incidence reflection data along line 3 (location in Fig. 2.7).

3.5 Summary

The image produced from the migration of multiples alone is comparable to the near-vertical reflection image obtained from the surface-towed streamers (e.g., Fig. 3.16) in terms of lateral illumination and is much better than the image produced from the migration of upgoing primary wavefield. The improvement is mainly due to wider illumination especially for shallow, near seafloor targets and reduced exposure to shallow inhomogeneous anomalies under the seabed. The method can be very useful for sparse receiver spacings.

Chapter 4

Seismic tomography theory

4.1 Introduction

In this chapter, the theoretical background of different seismic tomographic methods is reviewed. Seismic tomographic methods are used for obtaining velocity models for the shallow structures within Georgia Basin and for the gas hydrate bearing sediments in the continental slope offshore Vancouver Island, as described in Chapters 5 and 6, respectively. In the Georgia Basin study, for which the shots and receiver stations are widely distributed, a three-dimensional (3D) seismic tomographic method developed by *Zelt and Barton* (1998) was used (Chapter 5). For determination of structures and velocities associated with gas hydrate on the Vancouver Island slope, a two-dimensional (2D) velocity structure beneath a profile of 10 OBSs was required. Results in Chapter 6 were obtained using the method of *Zelt and Smith* (1992).

Seismic tomography involves estimation (or *reconstruction*) of the velocity structure of the earth from observation (or *projection*) of seismic data on the surface. It is an inverse problem where the information from the seismic data such as traveltime, amplitude,

waveform spectra or full waveform is used to constrain the earth models represented by a number of model parameters. The word *tomography* itself means slice picture (two-dimensional or 2D) as derived from the Greek word $\tau o' \mu o \sigma$ (*tomos*) meaning slice or section. Initially used by the medical community to study the human body from X-ray attenuation (*Lee and Pereyra* 1993), it was later adapted by seismologists to study the earth structures from seismic waves and was later extended to three-dimensional (3D) structural imaging.

4.2 Theory

Seismic traveltime tomography involves imaging the velocity structure of the subsurface by using time delays between source events and receiver arrivals. The original method for this was proposed by *Aki et al.* (1977) in their study of the earth's crust under the NORSAR array in Norway. Since then, it has been successfully applied to a variety of earth structures ranging from the crust (*White* 1989, *Zelt et al.* 1996, *Ramachandran* 2001) to the whole earth (*van der Hilst et al.* 1997, *Grand et al.* 1997) and utilizing both controlled source and earthquake data.

The mathematical basis of seismic tomographic reconstruction of velocity field is the ray approximation, for which the traveltime t of a seismic arrival can be identified with the integral of slowness (reciprocal of velocity) along the corresponding ray path:

$$t = \int_{L(s)} s(\mathbf{r})\, dl, \tag{4.1}$$

where $s(\mathbf{r})$ is the slowness field of the medium and L is the ray path. The ray path location

itself depends upon the slowness field $s(\mathbf{r})$ thus making the relationship between t and $s(\mathbf{r})$ nonlinear. The nonlinear inverse problem is often solved by linearized inversion techniques that exploit Fermat's principle, which states that the traveltime along a ray path does not change to first order when the ray is perturbed (for a small change in slowness). Iterations are required to update the starting model until the misfit between the observed and the calculated time reduces to the desired level. If, however, the final model is sufficiently close to the starting model that the rays in the starting model are an accurate representation of the true rays, then iterations are not necessary (*Hole* 1992).

Seismic tomographic reconstruction usually involves the following steps:

- **Model parametrization:** The region under study is defined in terms of finite number of model parameters.
- **Forward modelling:** Model data (such as traveltime) are calculated using the source-receiver geometry.
- **Inversion:** Model parameter values are updated to minimize the misfit between the observed data and the data computed from the model parameters.
- **Appraisal problem:** The estimated model is tested for resolution.

4.2.1 Model parametrization

While the velocity (or slowness) field of the subsurface varies continuously with position, any practical description of it requires that it be represented by a finite number of parameters. In crustal tomography the velocity field is often defined by a set of constant velocity blocks (*voxels*) or nodes with a specified interpolation function to define the ve-

locity within the blocks. Constant velocity blocks are easy to define and result in linear ray paths within each block (*Aki et al.* 1977, *Humphreys and Clayton* 1988). However, the velocity discontinuity between adjacent blocks makes it difficult to represent a smooth model of the subsurface. This is partly overcome by using a large number of velocity blocks and putting restrictions on the magnitude of velocity change between adjacent blocks. An alternative to block parametrization is the grid parametrization, where the velocity values are defined at the vertices of a rectangular grid together with a specified interpolation function (*Thurber* 1983).

Some tomographic methods solve for interface depth along with the velocity field. (*Bishop et al.* 1985, *White* 1989). For this purpose the subsurface is parameterized both in terms of velocity and interface depth. The wide-angle ray tracing method of *Zelt and Smith* (1992) and the reflection method of *Williamson* (1990) define the interface geometry by piecewise linear segments. The interface is often smoothed to avoid discontinuity of the interface gradient at the joints between the segments.

4.2.2 Forward modelling

Forward modelling involves calculation of traveltimes given the source-receiver geometry. Rays are traced such that the path between a source and a receiver is an extremum with respect to travel time (*Cervený* 1987). Typically, a solution is sought that is the global minimum in traveltime (first arrivals), but secondary arrivals are sometimes utilized. Because tomographic methods rely on thousands of ray paths to sample a study volume, the ray tracing must be computationally efficient. To attain efficiency, some ray tracing algorithms assume that the ray paths calculated for a one-dimensional model ad-

equately represent those in a two- or three-dimensional structure (*Thurber* 1983, *Um and Thurber* 1987). Recent advances in numerical methods, however, provide several new and more accurate approaches to calculate seismic ray paths and travel times for 2D and 3D models (e.g., *Vidale* 1988, 1990).

Vidale (1988)'s method uses a wavefront tracking approach, in which finite-difference solutions of the eikonal equation are sought to compute the traveltime of the waves in a medium. The slowness of the medium is represented on the nodes of a rectilinear grid with interpolated slowness values between the nodes. The method progressively calculates the traveltimes along expanding squares in 2D.

The eikonal equation, which describes the propagation of seismic wavefront in an elastic medium, can be described as:

$$(\nabla T)^2 = [s(\mathbf{r})]^{\mathbf{2}} \tag{4.2}$$

and in 2D,

$$\left(\frac{\partial T}{\partial x}\right)^2 + \left(\frac{\partial T}{\partial z}\right)^2 = [s(x,z)]^2 \tag{4.3}$$

where T is the traveltime of the propagating wavefront. Assuming that the traveltime at point A in Figure 4.1 is known (say, T_0), the traveltimes at nodes B1, B2 and C1 will be

$$T_1 = T_0 + \frac{\partial T}{\partial x}h \tag{4.4}$$

$$T_2 = T_0 + \frac{\partial T}{\partial z}h \tag{4.5}$$

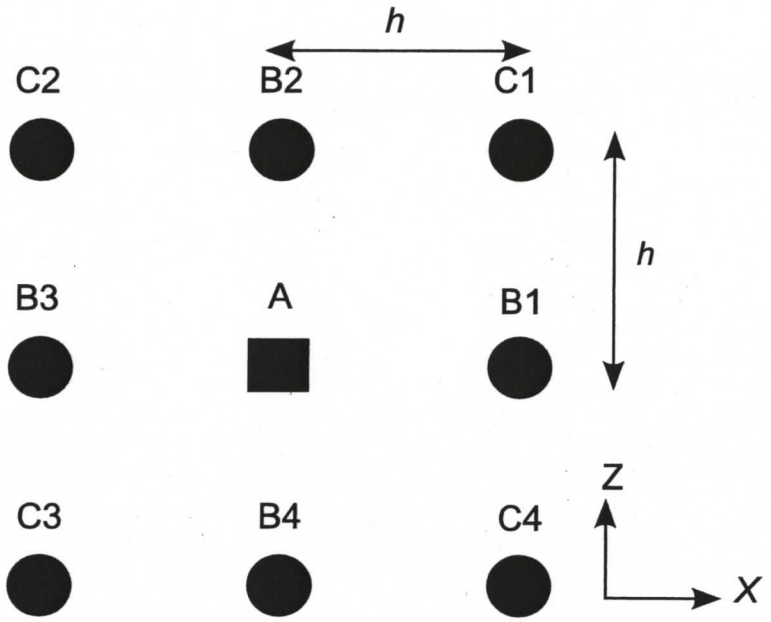

Figure 4.1: *Vidale* (1988)'s method of calculating traveltime. h is the grid interval in both x and z directions.

$$T_3 = T_0 + \left(\frac{\partial T}{\partial x} + \frac{\partial T}{\partial z}\right) h \tag{4.6}$$

respectively. The gradient of T along the x and z directions can then be obtained with the following equations:

$$\frac{\partial T}{\partial x} = \frac{1}{2h}[T_3 + T_1 - T_2 - T_0] \tag{4.7}$$

$$\frac{\partial T}{\partial z} = \frac{1}{2h}[T_3 + T_2 - T_1 - T_0]. \tag{4.8}$$

Substituting the values of $\frac{\partial T}{\partial x}$ and $\frac{\partial T}{\partial z}$ in equation 4.3, one can obtain the value of T_3 as

$$T_3 = T_0 + \sqrt{(2\overline{s}^2 h^2 - (T_1 - T_2)^2} \tag{4.9}$$

where $\overline{s}$ is the average slowness.

The above formula assumes that the wave field propagates through the medium as plane waves which is valid for the far field. *Vidale* (1988) also derived a separate formulation for the circular, near-field wavefront. Ray tracing under a wavefront tracking approach like above is done by following the traveltime gradient ∇T backward through the computed traveltime from the receivers to the source. ∇T is always perpendicular to the first-arrival wavefront and therefore traces the first-arrival ray path.

While *Vidale* (1988, 1990)'s expanding square (or, cube in case of 3D) method is efficient in calculating the first-arrival traveltimes, it fails when the wave encounters large, sharp velocity contrasts within the medium (*Hole and Zelt* 1995). In that case, the geometry of the expanding square does not resemble the shape of the first-arrival wavefront. Thus the computed traveltimes may not represent first-arrivals. Another limitation of *Vidale* (1988, 1990)'s method is that it can not compute reflection traveltimes. The reason for this, as pointed out by *Hole and Zelt* (1995), is that *Vidale* (1988, 1990)'s scheme lacks head-wave operators that allow waves to travel along the boundaries of the grid cells, and there is no provision for the expanding waves to sharply turn back towards the source. Several schemes have been proposed incorporating new finite-difference operators to tackle the above problem (*Podvin and Lecomte* 1997, *van Trier and Symes* 1991, *Qin et al.* 1992, *Hole and Zelt* 1995). *Hole and Zelt* (1995) modified *Vidale* (1988, 1990)'s algorithm by incorporating head-wave operators and reverse propagation of traveltimes that enabled traveltime computation for large velocity contrasts and reflected waves.

4.2.3 Inversion

The inverse step involves updating the model parameter values to minimize the misfit between the observed and calculated traveltimes. In seismic tomographic studies, the relationship between data (traveltime) and model (slowness) parameters in equation 4.1 is non-linear since the ray path itself depends upon the slowness. Thus the problem is solved by linearizing equation 4.1 using Fermat's principle of ray path stationarity with respect to slowness (*Hole* 1992). Considering a small perturbation $\delta s(\mathbf{r})$ to the reference slowness field $s_o(\mathbf{r})$, equation 4.1 can be written as

$$t = \int_{L(s_o+\delta s)} s_o(\mathbf{r})\, dl + \int_{L(s_o+\delta s)} \delta s(\mathbf{r})\, dl, \tag{4.10}$$

Using Fermat's principle, the integral over $L(s_o + \delta s)$ can be approximated by an integral over $L(s_o)$ in the reference slowness field. The first integral in the above equation then becomes t_o, the traveltime in the reference slowness field. Thus

$$t = t_o + \int_{L(s_o)} \delta s(\mathbf{r})\, dl, \tag{4.11}$$

Since the ray path $L(s_o)$ and the traveltime t_o can be calculated for the reference slowness field, the relationship between the traveltime residual and the slowness perturbation near the reference slowness field

$$\delta t = \int_{L(s_o)} \delta s(\mathbf{r})\, dl, \tag{4.12}$$

is linear and can be used for inversion. Since equation 4.12 is a linearization of the nonlinear problem, iterations are required to find the final slowness model. Written in a more general matrix form equation 4.12 can be written as

$$\delta \mathbf{t} = \mathbf{A}\delta \mathbf{m} \tag{4.13}$$

where $\delta \mathbf{t}$ is the data (traveltime) residual vector, and $\delta \mathbf{m}$ is the model correction. It must be noted that the model parameters may also contain the layer interface depth in addition to the slowness field (as in the case of reflection tomography). The matrix $\mathbf{A}$ (usually called the Jacobian or sensitivity matrix) contains the partial derivatives of the traveltimes with respect to the model parameters ($A_{ij} = \frac{\partial t_i}{\partial m_j}$) evaluated at $\mathbf{m_o}$. The linearized equations are solved by either creeping or jumping approach (*Shaw and Orcutt* 1985). In the creeping approach, the inverse problem is solved for $\delta \mathbf{m}$ (from equation 4.13) and the final solution is achieved by proceeding with small perturbations $\delta \mathbf{m}$ from the starting model. Hence the final solution depends on the starting model. The prior information must be applied to $\delta \mathbf{m}$ in the form of a solution norm. Typically the smallest value of $\delta \mathbf{m}$ is sought. In the jumping approach, the inverse problem is formulated in terms of the model $\mathbf{m}$ (not the perturbation $\delta \mathbf{m}$). Substituting $\mathbf{m} - \mathbf{m_o}$ for $\delta \mathbf{m}$ in equation 4.13,

$$\mathbf{A}\mathbf{m} = \delta \mathbf{t} + \mathbf{A}\mathbf{m_o} \tag{4.14}$$

where $\mathbf{m}$ is the updated model. The right hand side contains all the known quantities. The solution is achieved by proceeding through a series of unconstrained changes and, therefore, is more likely to be independent of the starting model. The final model in both

creeping and jumping approaches is determined when the solution converges.

4.2.4 Regularized Inversion

Tomography, like other geophysical inverse problems, suffers from ill-posedness problems. Ill-posedness arises from the fact that the solution is neither unique nor stable. The primary reason for this is the attempt to extract too much information from the data. Also, the data are always contaminated with noise. The presence of errors due to both measurement uncertainties and modelling approximation implies that the system of equations do not completely describe the physical model. Furthermore, there are a large number of model parameters sampled by only a few observations (a much smaller number of rays travel through some parts of the model) making the inverse problem underdetermined. This makes the system of equations ill conditioned and the solutions unstable in the presence of errors. An effective way to deal with ill-posed problems is to regularize the solution by introducing *a priori* information to the inverse problem. Additional constraints are imposed, which the solution must satisfy so that the under-determined part of the solution is controlled (*Scales et al.* 1990). The constraints result in the final model satisfying some property in addition to fitting the data. The property is often chosen so that the model has "minimum structure", that is, the model includes only structure that is required to fit the data according to its noise level. Minimum structure is usually measured in terms of model roughness (second spatial derivatives), although model flatness (first order spatial derivatives) is sometimes used. Regularized inversion minimizes an objective function that includes norms that measure model roughness/flatness and data

misfit. With regularization term applied, the objective function takes the form

$$\mathbf{\Phi}(\mathbf{m}) = (\mathbf{Am} - \delta\mathbf{t} - \mathbf{Am_o})^{\mathbf{T}}\,\mathbf{C_d^{-1}}\,(\mathbf{Am} - \delta\mathbf{t} - \mathbf{Am_o}) + \lambda\mathbf{m^T R^{-1} m} \tag{4.15}$$

where the first term in the right hand side is the data misfit and the second term is the prior misfit (regularization term). $\mathbf{C_d}$ is the data covariance matrix containing standard deviation values (σ_i) associated with each data value. For uncorrelated data errors, $\mathbf{C_d}$ = diag $\{\sigma_i^2\}$. λ is the trade-off parameter and $\mathbf{R}$ is the regularization or roughening matrix. The trade-off parameter λ controls the relative importance of data misfit and prior information. The value of λ is chosen such that the acceptable data misfit with Gaussian noise distribution is equal to the expected value for the χ^2 misfit statistics ($\chi^2 = (t_{calc} - t_{obs})^T C_d^{-1}(t_{calc} - t_{obs})$, i.e., $< \chi^2 >= N$, where N is the number of data, and t_{calc} and t_{obs} are the calculated and observed traveltime respectively). The primary reasons for seeking smooth models, as pointed out by *Zelt and Barton* (1998), are that : (i) infinite-frequency ray methods are valid only for smooth media, (ii) traveltimes constrain only the long wavelength model features since the data represent integrals through the model, and (iii) the linearization assumption of stationary ray paths is more likely to be satisfied for smooth models.

The damped least square (DLS) method is another variant of regularization, where the solution is obtained by minimizing a combination of data residual and solution length. The damped least square solution is a perturbation from the starting model and can be written as

$$\delta\mathbf{m} = (\mathbf{A^T C_d^{-1} A} + D\mathbf{C_m^{-1}})^{-1}\mathbf{A^T C_d^{-1}}\delta\mathbf{t} \tag{4.16}$$

where the damping parameter D regulates the balance between data residual and solution length. Damping reduces the total length of the solution perturbation vector, but puts no constraint on the similarity of adjacent elements of the solution (*Phillips and Fehler* 1991). $\mathbf{C_d}$ and $\mathbf{C_m}$ are the data and model covariance matrices which, under the assumption of uncorrelated uncertainties, are diagonal matrices $\mathbf{C_d} = \text{diag}\ \{\sigma_i^2\}$, $\mathbf{C_m} = \text{diag}\ \{\sigma_j^2\}$. The standard deviation, σ_i, is the estimated uncertainty of the i^{th} traveltime measurement. The value of σ_j is an *a priori* estimate of the uncertainty of the j^{th} model parameter.

4.2.5 Model Assessment

Model resolution tests are necessary for evaluating the quality or robustness of a solution to an inverse problem. Parametrizations that describe continuous velocity fields often opt for resolution tests that attempt to reconstruct a synthetic model using the same source-receiver geometry as the real experiment. Checkerboard test is a common approach to estimate model resolution, in which a laterally alternating anomaly pattern of positive and negative squares is added to the final velocity model for the depth range of the model. Synthetic data are generated by using the source-receiver geometry of the real data. Gaussian noise, with standard deviations equal to the pick uncertainties, is added to the synthetic data to invert for the perturbed model. Regions of the recovered model perturbation that resemble the checkerboard pattern are considered to be well resolved at the length scale of the checkerboard anomaly.

Zelt and Smith (1992) describe methods to estimate the spatial resolution and absolute uncertainty value of specific model parameters. To test the spatial resolution, a single model parameter of the final model is perturbed on the order of its estimated uncertainty

and traveltime is computed for the perturbed model. The perturbed parameter is then reset to its final value and the synthetic traveltimes are inverted to solve for all model parameters that were determined at the same time as the selected parameter. The amount of smearing of the selected parameter's perturbation into other parameters gives an indication of the spatial resolution about the selected parameter. *Zelt and Smith* (1992) estimate a parameter's absolute uncertainty by perturbing its final value and holding it fixed while inverting the observed data for all other model parameters that were determined at the same time as the selected parameter. The absolute uncertainty is indicated by the smallest perturbation for which the resulting model is unable to fit the data as well as the final model, either because it is impossible to trace rays to all observations, or the χ^2 values of the two models differ signicantly.

4.3 Method and Modelling

4.3.1 3D Modelling

The 3D velocity structure is determined using tomographic inversion of first-arrival traveltime data. The regularized inversion algorithm of *Zelt and Barton* (1998) is used. The algorithm allows for variable weighting with depth of any combination of smallest, flattest and smoothest perturbation constraints. *Zelt and Barton* (1998) use the jumping strategy of linearized, iterative inversion that penalizes the total model roughness. The amount of regularization is determined automatically to achieve the final model for which the normalized χ^2 is 1. Non-linearity is accounted for by iteratively updating the starting model. New ray paths are calculated at each iteration. Traveltimes are calculated on a uniform grid using a finite difference solution to the eikonal equation (*Vidale* 1990).

The objective function Φ minimized at each iteration is given by

$$\Phi(\mathbf{m}) = \delta\mathbf{t}^{\mathbf{T}}\mathbf{C}_d^{-1}\delta\mathbf{t} + \lambda\left[\mathbf{m}^{\mathbf{T}}\mathbf{C}_h^{-1}\mathbf{m} + s_z\mathbf{m}^{\mathbf{T}}\mathbf{C}_v^{-1}\mathbf{m}\right] \tag{4.17}$$

where $\mathbf{m}$ is the model vector, δt is the data residual vector; $\mathbf{C}_d$ is the data covariance matrix; $\mathbf{C}_h$ and $\mathbf{C}_v$ are the horizontal and vertical roughening matrices, respectively. The trade-off parameter λ determines the overall amount of regularization and tells how well the solution will satisfy the data and the smoothness. s_z determines the relative importance of maintaining vertical versus horizontal smoothness. The value of λ is reduced at each iteration to stabilize the inversion by constraining the long-wavelength model structure in the initial iterations and by allowing finer model structure in later iterations. Following *Zelt and Barton* (1998) the system of equations solved at each iteration is given by

$$\begin{bmatrix} \mathbf{C}_d^{-1/2}\mathbf{L} \\ \lambda\mathbf{C}_h \\ s_z\lambda\mathbf{C}_v \end{bmatrix} \delta\mathbf{m} = \begin{bmatrix} \mathbf{C}_d^{-1/2}\delta\mathbf{t} \\ -\lambda\mathbf{C}_h\mathbf{m_0} \\ -s_z\lambda\mathbf{C}_v\mathbf{m_0} \end{bmatrix} \tag{4.18}$$

where $\mathbf{m_0}$ is the current model, $\delta\mathbf{m}$ is the slowness perturbation, and $\mathbf{m} = \mathbf{m_0} + \delta\mathbf{m}$. The matrix $\mathbf{L}$ is the partial derivative matrix with elements L_{ij} $(= \frac{\partial t_i}{\partial m_j})$ equal to the path length of the i^{th} ray in the j^{th} cell of the model. The roughening matrices $\mathbf{C}_h$ and $\mathbf{C}_v$ contain the 2D and 1D second derivative finite difference operators that measure the model roughness in the horizontal and vertical directions respectively. Each row of $\mathbf{C}_h$ contains five non-zero elements of the Laplacian operator equal to $1/m_j, 1/m_j, -4/m_j, 1/m_j$ and $1/m_j$ where the cells correspond to the central cell and the four adjacent cells in the x and y directions and m_j is the prior slowness of the center cell. The horizontal roughening

matrix is

$$\mathbf{C}_h = 1/m_j \begin{bmatrix} \vdots & & & & & & & & & & & & & & \\ \cdots & 0 & 1 & 0 & \cdots & 0 & 1 & -4 & 1 & 0 & \cdots & 0 & 1 & 0 & 0 & \cdots \\ \cdots & 0 & 0 & 1 & 0 & \cdots & 0 & 1 & -4 & 1 & 0 & \cdots & 0 & 1 & 0 & \cdots \\ \vdots & & & & & & & & & & & & & & \end{bmatrix} \tag{4.19}$$

The normalization by prior slowness is applied to avoid a bias towards greater levels of model roughness in regions of high velocity. Similarly, each row of $\mathbf{C}_v$ has three non-zero elements equal to $1/m_j, -2/m_j$ and $1/m_j$, where the elements correspond to the central cell and two adjacent cells in the z-direction. The vertical roughening matrix is

$$\mathbf{C}_v = 1/m_j \begin{bmatrix} \vdots & & & & & & & & & & & & & & \\ \cdots & 0 & 1 & 0 & \cdots & 0 & 0 & -2 & 0 & 0 & \cdots & 0 & 1 & 0 & 0 & \cdots \\ \cdots & 0 & 0 & 1 & 0 & \cdots & 0 & 0 & -2 & 0 & 0 & \cdots & 0 & 1 & 0 & \cdots \\ \vdots & & & & & & & & & & & & & & \end{bmatrix} \tag{4.20}$$

This system of equation is sparse and is solved using the LSQR variant of the conjugate gradient algorithm (*Paige and Saunders* 1982) which is an efficient technique to solve large, sparse matrices.

4.3.2 2D Modelling

Two dimensional (2D) velocity structure is obtained by the widely-used damped least square traveltime inversion algorithm of *Zelt and Smith* (1992). The advantage of this

method over grid-based methods is its ability to include reflection interfaces during model parametrization. Also, the velocity and interface node distribution can be adapted to suit variations in subsurface data coverage. The algorithm follows a minimum parameter approach and allows simultaneous determination of layer boundaries and velocities within the layers. Layer boundaries are defined by arbitrarily spaced boundary nodes with linear interpolation between them. Layer thickness can be reduced to zero to allow for modelling of pinchouts. Velocity within a layer can vary both laterally and vertically. Velocity values are calculated by linear interpolation of upper and lower velocity nodes tied to the upper and lower boundary of the layer. For velocity interpolation, each layer is divided laterally into several trapezoidal blocks and the velocity within each trapezoid is interpolated using the velocity values of the four corners. Ray tracing is based on the asymptotic ray theory of *Cervený* (1987). Rays are traced by numerically solving the initial value problem formulated by a pair of ordinary differential equations in terms of depth z and offset x. The incident angle is related to x and z with the following relation.

$$
\begin{aligned}
&45^o \leq \theta \leq 90^o \\
&\quad \frac{\partial z}{\partial x} = cot\theta \quad and \quad \frac{\partial \theta}{\partial x} = \frac{v_z - v_x cot\theta}{v} \\
&0^o \leq \theta \leq 45^o \\
&\quad \frac{\partial x}{\partial z} = tan\theta \quad and \quad \frac{\partial \theta}{\partial z} = \frac{v_z - v_x cot\theta}{v}
\end{aligned}
\tag{4.21}
$$

The inverse problem is solved using an iterative damped least square method with rays traced at each iteration. The process is repeated until the solution converges.

4.4 Summary

Seismic traveltime tomography is the most popular approach for imaging subsurface velocity structure. A wide range of schemes and algorithms are found in the literature that are suitable for different source-receiver geometry, data, and model dimensions.

However, limitations do exist. One of the major difficulties is associated with the forward computation of traveltime and ray path determination since these are based upon simple model parametrization. Most of the ray-based tomographic methods calculate ray paths for the first arrivals and it can be computationally expensive for calculating later arriving refracted and reflected phases particularly in 3D complex media. Combination of different data sets such as wide-angle and local earthquake data may partly overcome the above problem.

The inverse problem is often solved by using linearized inversion schemes, by assuming the starting model to be close to the true model. The solution thus obtained, depends on the starting model and may not represent the "true" subsurface structure. So global optimization schemes, which are independent of the starting model such as simulated annealing or genetic algorithms may be used, although they are computationally intensive. Error and resolution analysis may also be made in a more realistic way to promote a more robust interpretation of the results. Waveform tomography may be used for studying regions that require very high resolution.

Chapter 5

Upper crustal structure of Georgia Basin

In this chapter, tomographic analyses of the wide-angle seismic refraction datasets from the GBGI and SHIPS experiments are presented. The analyses result in a high-resolution three-dimensional (3D) seismic P-wave velocity model of Georgia Basin. The results are consistent with the previous studies in this area, but provide higher resolution for the shallow structures than mapped from previous studies. Shallow crustal faults within the basin and bounding the basin are identified and some faults are correlated with the areas of high seismicity. The main elements and results presented in this chapter have been published in *Dash et al.* (2007).

5.1 Modelling approach

The 3D seismic velocity model is obtained using the First Arrival Seismic Tomography (FAST) method of *Zelt and Barton* (1998), as described in Chapter 4. The method utilizes a regularized inversion approach to address the ill-posedness of the inverse problem. *Zelt and Barton* (1998)'s method can incorporate any combination of smallest, flattest and smoothest perturbations, the weights of each being variable with depth. The present

analysis applies only the smoothing regularization that minimizes the roughness (the second spatial derivatives) of the perturbation from the background model. Non-linearity is addressed by iteratively solving the linearized problem. Linearization requires a starting model that is close to the final model. The starting model was constructed by examining the trend of the first arrival travel times. A total of approximately 380,000 traveltime picks from 63 receivers around the Strait of Georgia were obtained, of which 38 receivers were from the GBGI experiment and 25 from the SHIPS experiment (Fig. 5.1). However, to reduce the computational time, the traveltime picks from the GBGI stations were decimated by taking one out of 5 picks. A simple one-dimensional (1D) velocity-depth model, estimated from the average time-distance plot, is used as a starting model (Fig. 5.2).

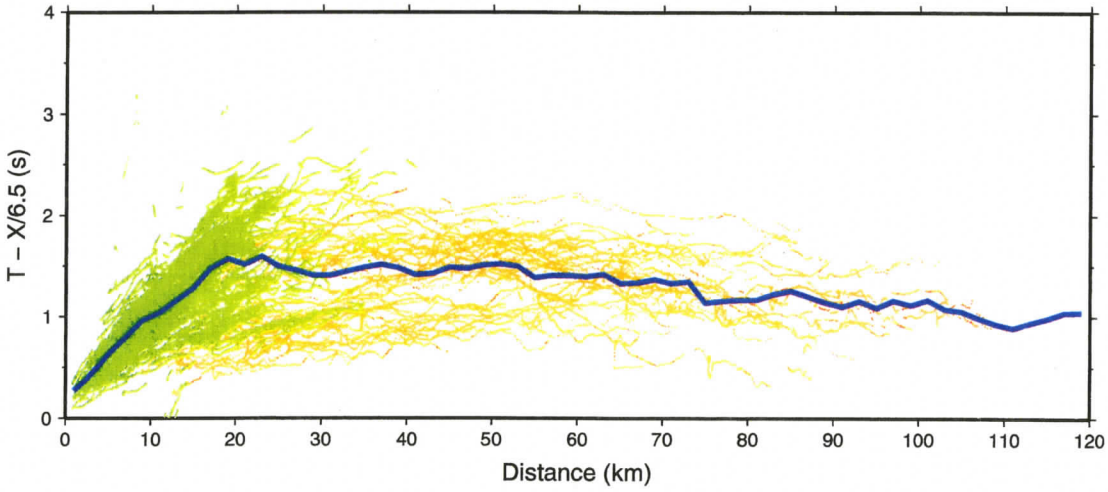

Figure 5.1: First arrival traveltimes from GBGI (green) and SHIPS (orange) stations around the Strait of Georgia reduced at 6.5 km/s. Apparent velocities from the GBGI experiment are smaller than those from SHIPS, because the shorter shot-receiver distance makes the seismic raypaths travel in only the shallower part of the basin. The solid blue line represents the average time in 2-km wide offset bins used to construct the starting model.

The 1D starting velocity model was extrapolated to a 3D model with model dimensions 139.2 km × 133.2 km × 20.4 km (Fig. 5.3). The top 1 km of the velocity model was kept above sea level (0 km) to account for the elevation of the receiver locations. For both

forward modeling and inversion, a node spacing (and cell size) of 600 m × 600 m × 600 m was used. In the forward modelling step, traveltimes at each equally spaced node were computed using *Vidale* (1990)'s finite-difference scheme. Ray paths were calculated at each iteration by tracing the gradient direction from the receiver to the source in the travel time grid.

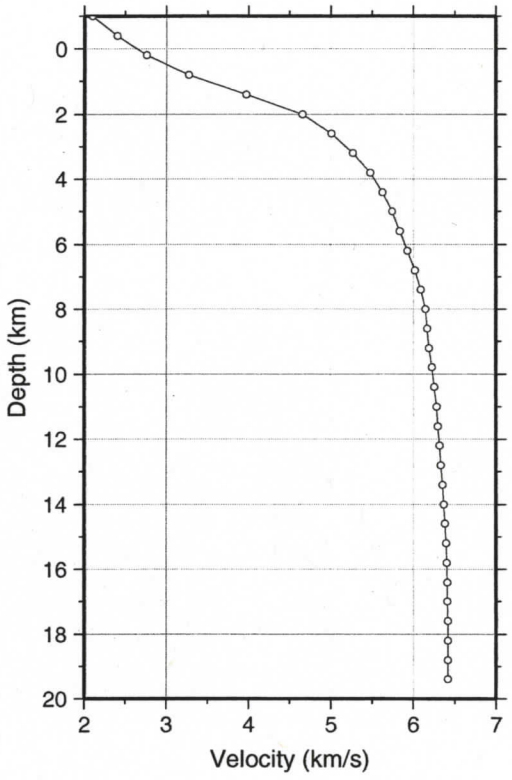

Figure 5.2: Starting 1D velocity model derived from the travel time picks. The circles represent the velocity values at every 600 m depth.

In the inverse step, smoothing regularization was applied with no variation along depth. The amount of regularization is determined automatically so that for the final model the normalized χ^2 data misfit equals 1. Approximately 121,000 picks were inverted for a minimum structure velocity model of the Georgia Basin. The initial normalized χ^2 misfit was 160 and the starting RMS traveltime residual was 650 ms (Fig. 5.4a). Due to

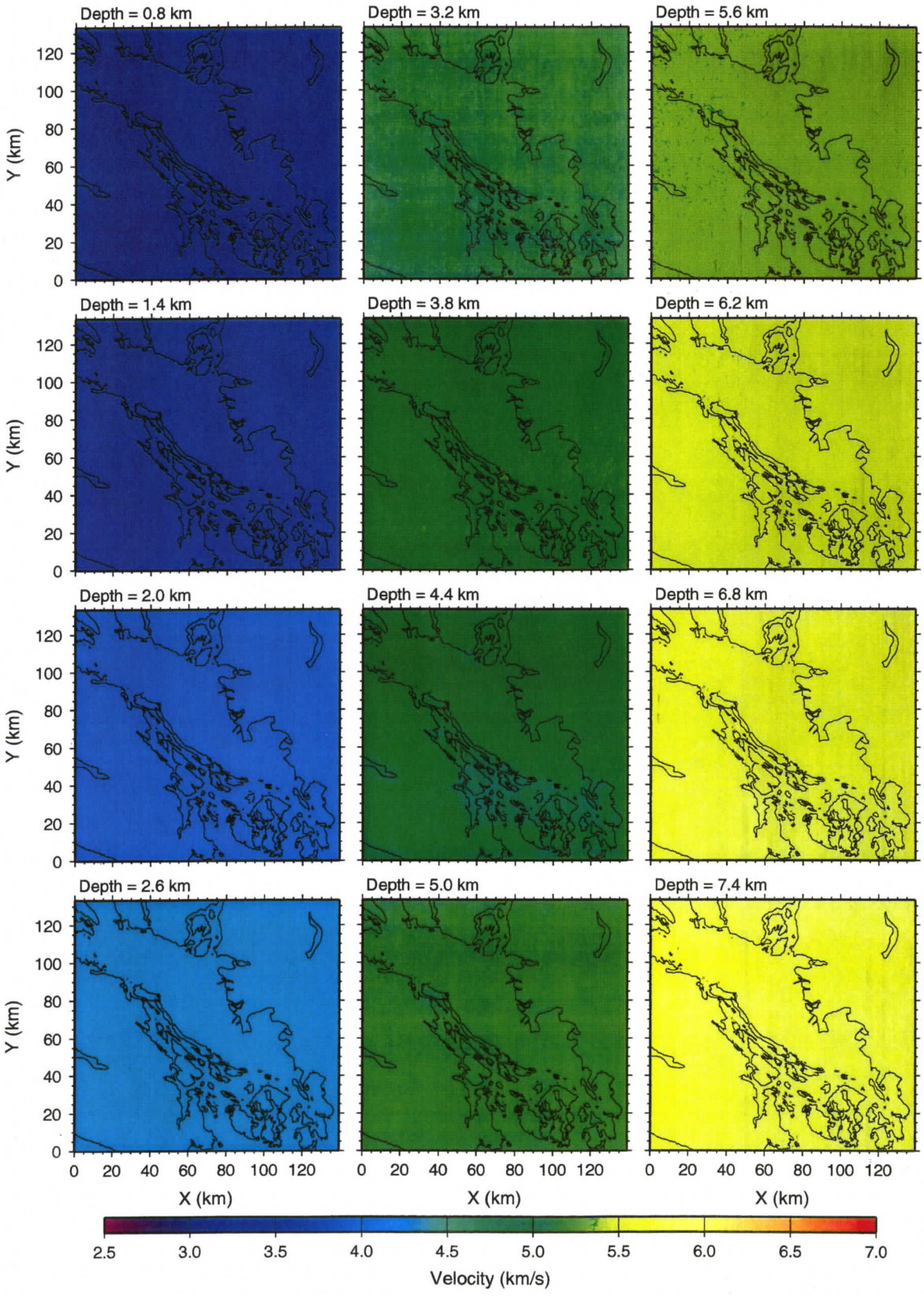

Figure 5.3: Horizontal slices through the starting model.

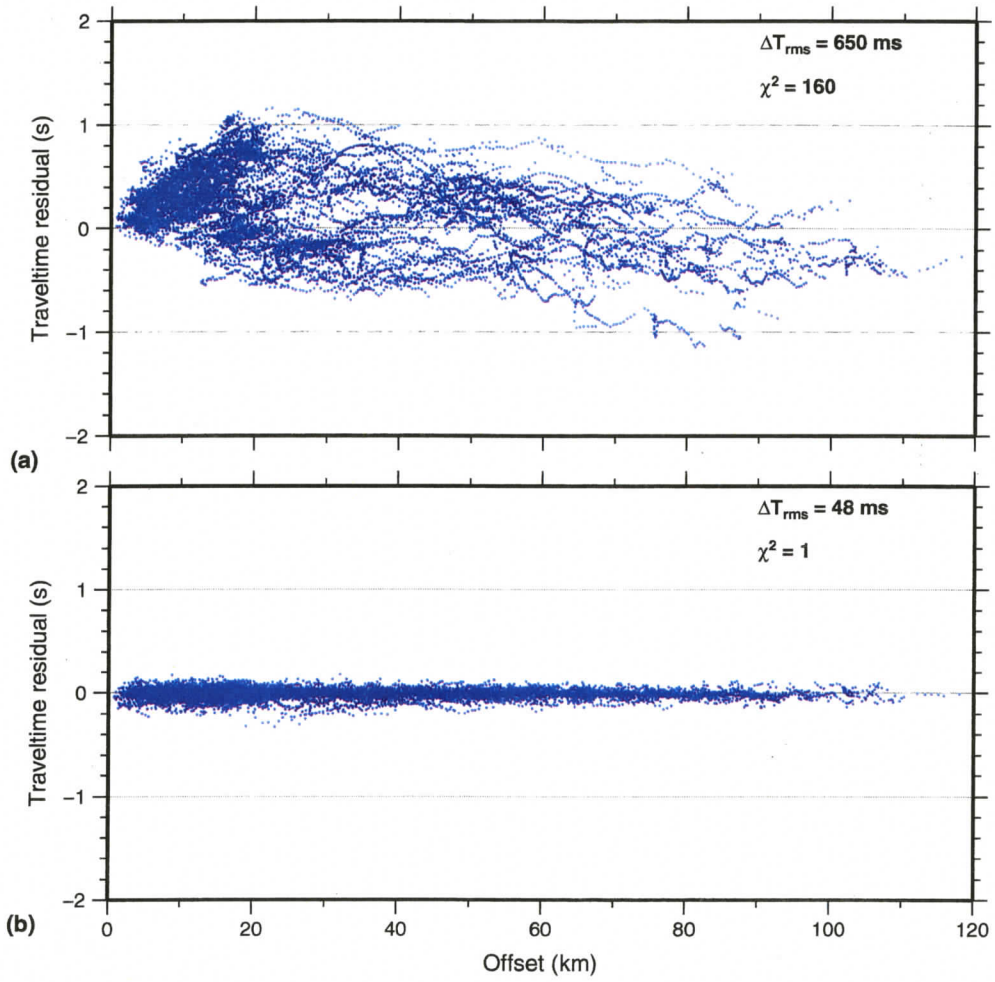

Figure 5.4: Traveltime residuals for the initial (a) and final model (b).

the asymmetric nature of the model (more than 130 km lateral dimension versus 20 km vertical dimension), vertical and horizontal roughnesses were assigned different weights. The inversion was initially run in test mode to determine the optimal value for the ratio of vertical to horizontal smoothness parameter s_z (from equation 4.17). The velocity models with different values of s_z were analyzed for smoothness and continuity in horizontal and vertical directions. For the final model, s_z was set to 0.25 and held fixed throughout the inversion. During the inversion, outliers that originated during manual picking of traveltimes (about 1% of the data) were identified and removed. The tradeoff parameter

λ between the regularization term and the data misfit term was initially set to 20. At each iteration, 5 λ values were tested and the value corresponding to the minimum χ^2 was passed to the next iteration. The process continued until convergence was achieved. The solution converged after 6 iterations. The final model had $\chi^2 = 1$ and an RMS traveltime residual of 48 ms (Fig. 5.4b), matching the accuracy of the traveltime picks.

5.1.1 Resolution Test

Two methods, ray hit counts and checkerboard tests, were used to determine the spatial resolution of the final model (*Humphreys and Clayton* 1988). In the ray hit count analysis, the number of rays penetrating each cell of the final velocity model was determined as an estimator of the resolution (*Toomey et al.* 1994). Figure 5.5 shows ray density at different depths through the final model. Ray coverage peaks at about 5 km. There are fewer deeper rays due to the short shot-receiver offset geometry of the GBGI experiment. At depths greater than 5 km, the ray coverage arises primarily from the sparser SHIPS data. Checkerboard tests were performed to determine the lateral resolution of the final model (*Zelt and Barton* 1998). For the lateral resolution tests, the final model was modified by adding velocity perturbations of $\pm 10\%$ in an alternating pattern of positive and negative squares (Fig. 5.6). Synthetic traveltimes were calculated through this modified model using the source-receiver geometry of the experiment. The new synthetic travel times were inverted after adding Gaussian noise that has a standard deviation equal to the estimated pick uncertainty in the traveltime data. The original final model was then subtracted to give a perturbation model. Regions of the recovered model perturbation that resembled the checkerboard pattern were considered to be well resolved at the length

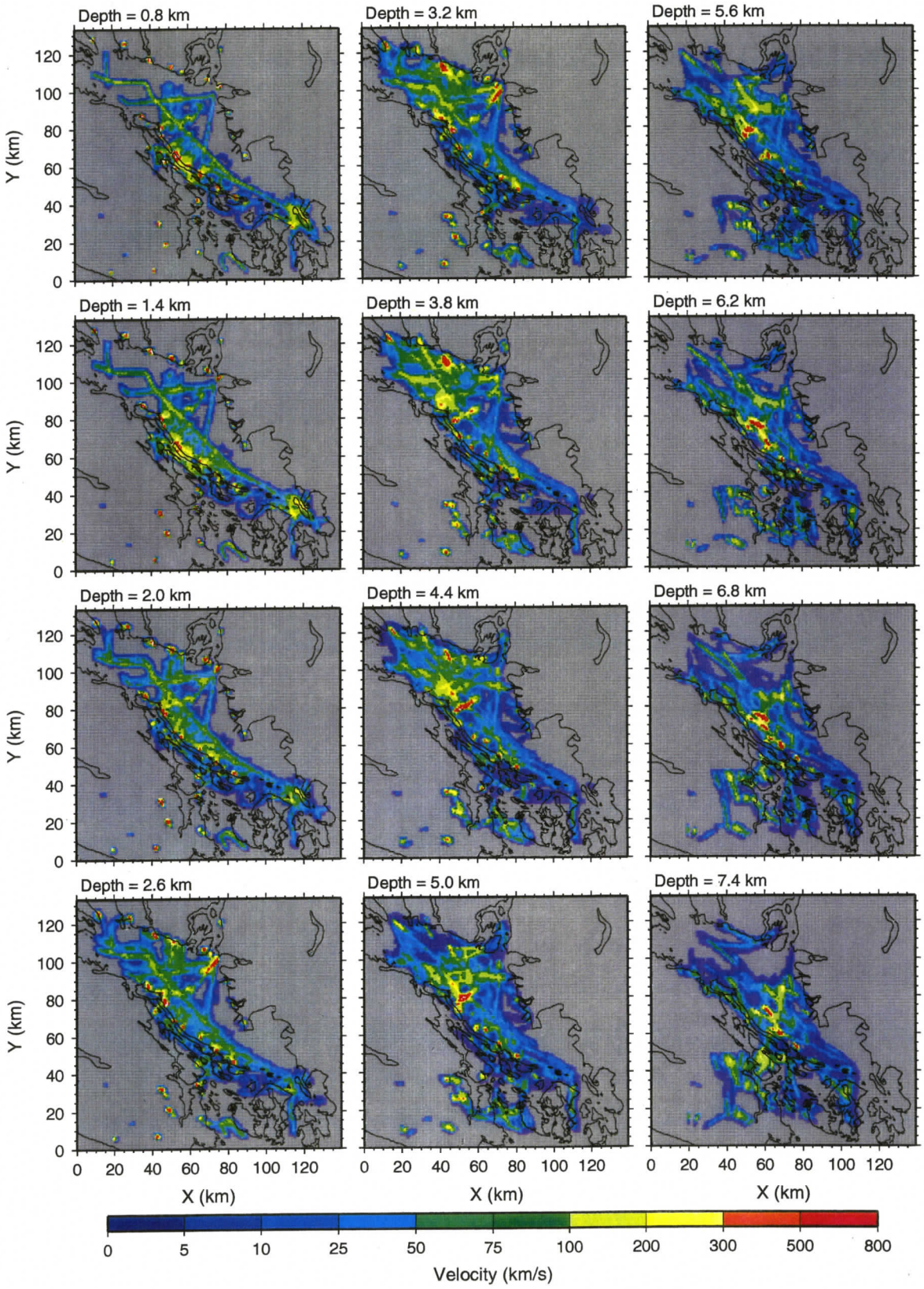

Figure 5.5: Ray density at different depths.

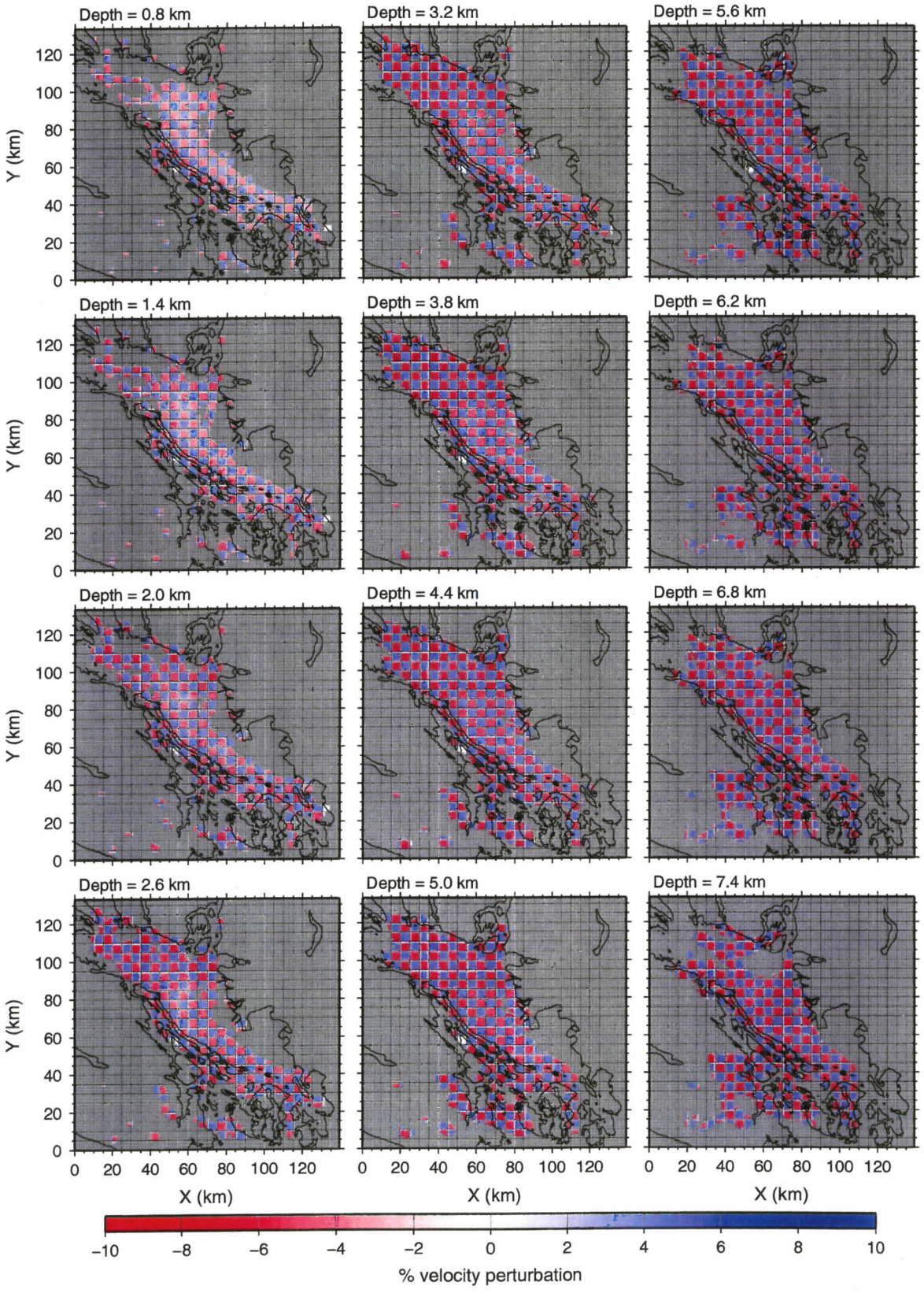

Figure 5.6: Input anomalies for checkerboard test with 5 km grid size.

scale of the checkerboard anomaly. Anomaly sizes of 5 km, 10 km and 20 km were tested. The recovered pattern for the 5 km anomaly size is shown in Figure 5.7. The lateral resolution is quite good down to 3.8 km. The recovered pattern for the 10 km anomaly size (Fig. 5.8) is well resolved over the depth range from 3 km to 5 km where there is dense ray coverage. Acceptable resolution for the 20 km anomaly pattern (Fig. 5.9) extends to 7 km depth, below which the resolution is poor due to the sparse ray coverage.

5.2 Tomography Results

The new final 3D velocity model is shown as horizontal slices (Fig. 5.10, Fig. 5.11 and Fig. 5.12), vertical slices (Figs. 5.13 and 5.14), and isovelocity surfaces (Fig. 5.15). For the location of geographic and geological features described in this section, the reader is referred to Figure 1.5. The perturbations from the starting model (Fig. 5.10) show areas that vary from the starting model. The most significant perturbation is to the east of Gabriola Island about 80-90 km north of the origin, particularly at depths from 2-5 km where velocities are up to 2 km/s higher than the uniform starting model. The final velocity model is well constrained to 6-7 km depth below which the ray coverage is poor. The results are consistent with the previous tomographic studies in this region (*Zelt et al.* 2001, *Ramachandran et al.* 2004), but have improved spatial resolution. For example, *Zelt et al.* (2001) used a cell size of 2.4 km $\times$ 2.4 km $\times$ 0.8 km for their 3D model and achieved a lateral resolution of 10 km at shallow depths and about 30 km at greater depths. A cell size of 1 km $\times$ 1 km $\times$ 1 km was used by *Ramachandran et al.* (2004), and their model had a lateral resolution of 20 km and above. The present model is obtained using a smaller cell size (0.6 km $\times$ 0.6 km $\times$ 0.6 km) and more data (from two experiments) leading to

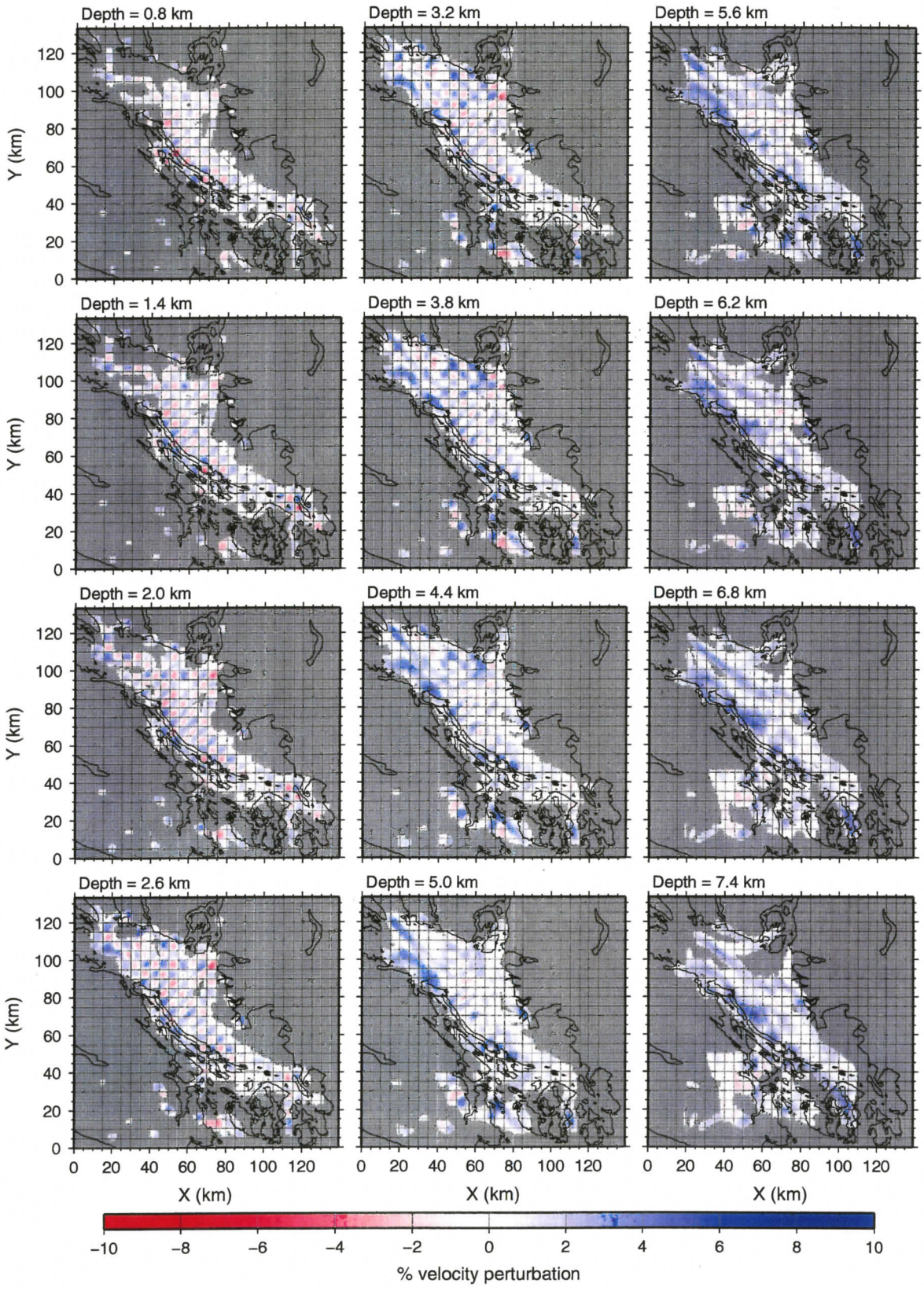

Figure 5.7: Recovered anomalies for checkerboard test with 5 km grid size.

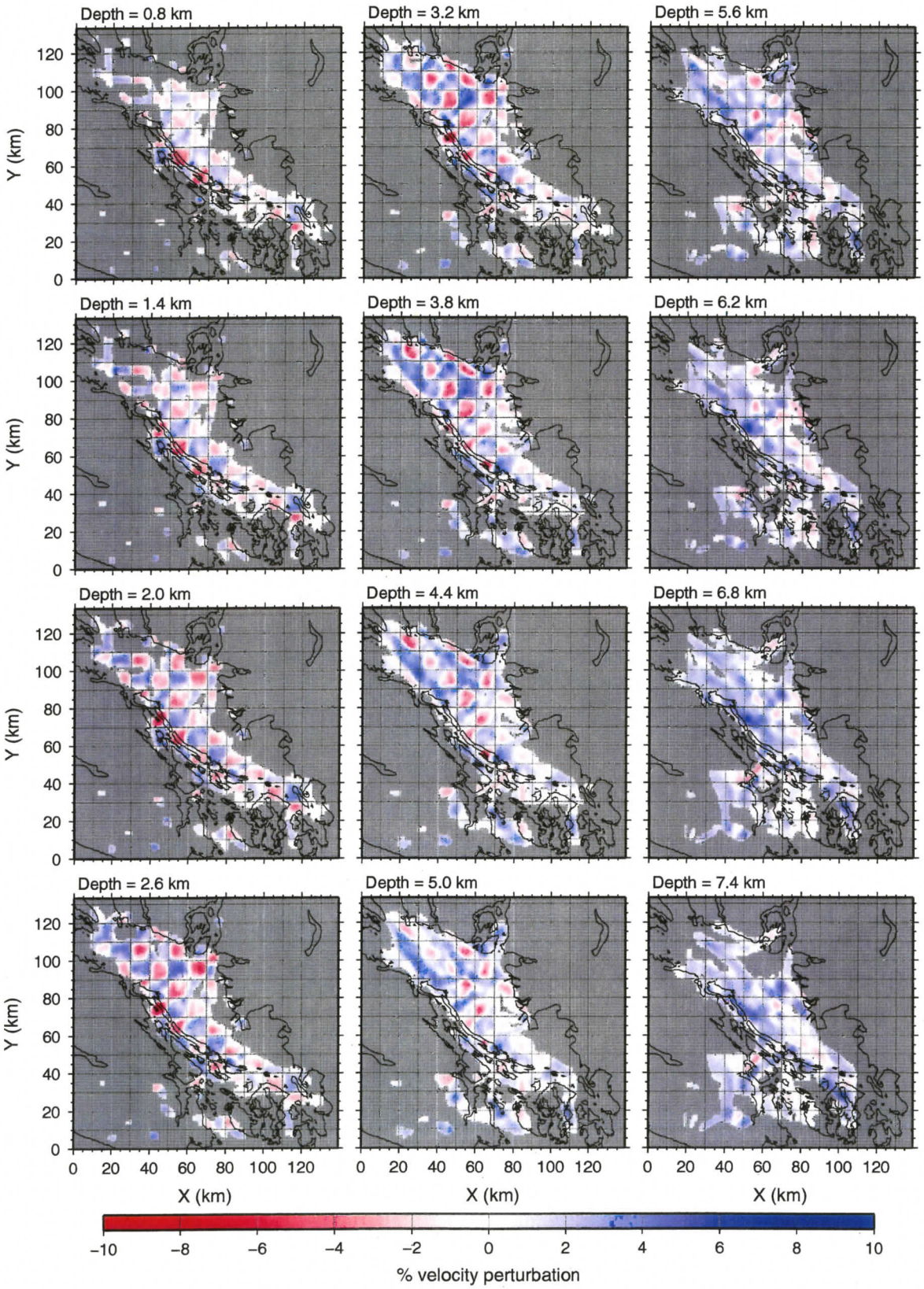

Figure 5.8: Recovered anomalies for checkerboard test with 10 km grid size.

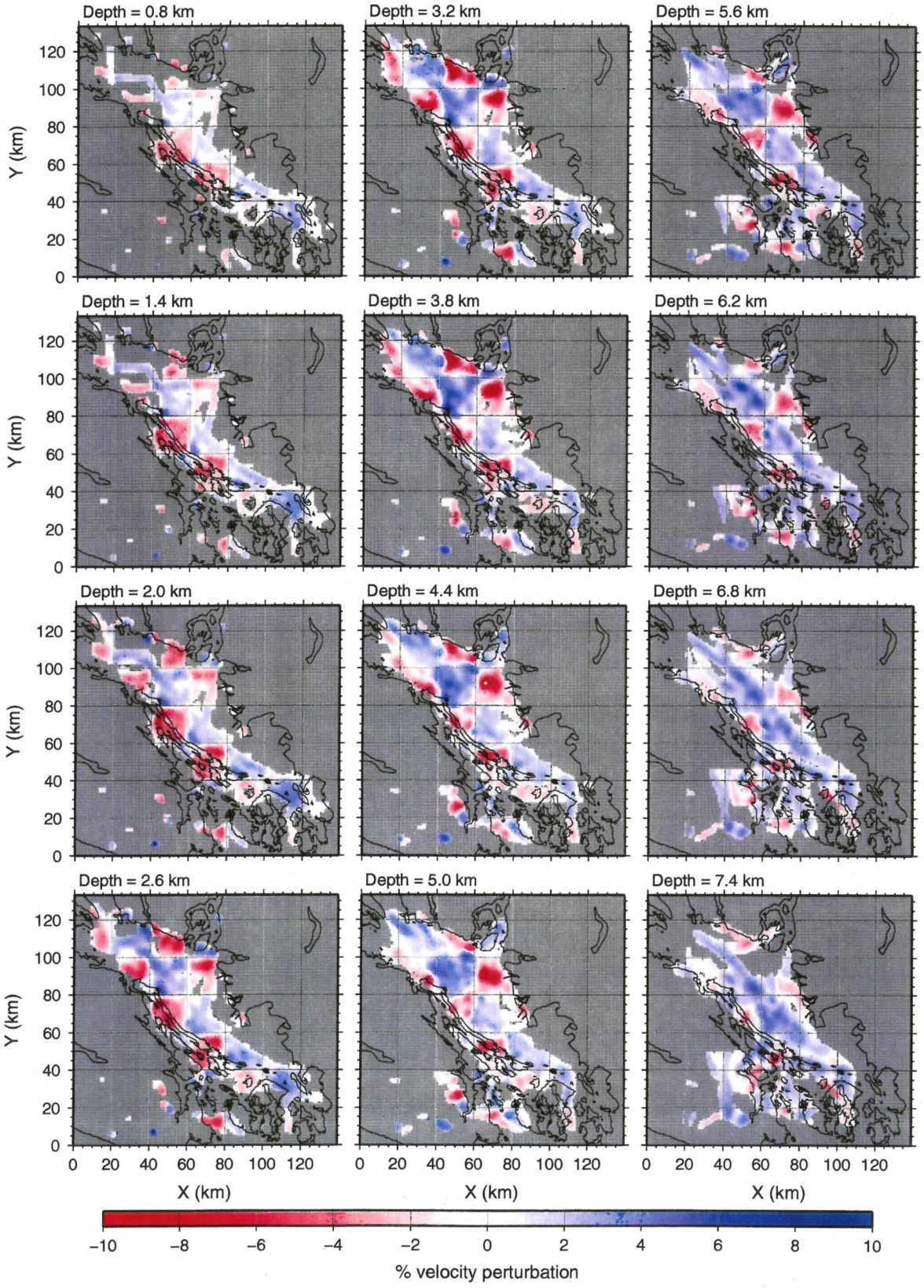

Figure 5.9: Recovered anomalies for checkerboard test with 20 km grid size.

an improved vertical and lateral resolution at shallow depths of 10 km or less. Also, the new model provides information for depths less than 2-3 km, which were not resolved in previous models (e.g., *Ramachandran et al.* 2004).

5.2.1 Definition of Georgia Basin

Horizontal slices through the final velocity model (Fig. 5.11) show velocity variations at different depths within Georgia Basin. At 0.8 km depth (Fig. 5.12a), velocities beneath Georgia Strait are typically 2.5 - 4.0 km/s and mostly correspond to the Cretaceous Nanaimo sedimentary rocks. Velocities above this depth are affected by regularization of the inversion and hence are not reported here.

Overall, the sedimentary rocks in the northwest of the strait have higher seismic velocity than the sedimentary rocks in the southeast at the same depth. *Zelt et al.* (2001) proposed that the lower velocities in the shallower portion of the basin in the south are associated with thicker layers of Tertiary and younger overlying sedimentary deposits. The higher velocity rocks ($\sim$ 6 km/s) at greater depth on the Vancouver Island side represent Wrangellia basement rocks (Fig. 5.11 and Fig. 5.12b). On the eastern side of the strait, the higher velocities possibly represent the basement rocks of the Coast Plutonic Complex (Fig. 5.14b). However, the new model does not define an identifiable velocity contrast representing the boundary between Wrangellia and the Coast Plutonic Complex.

Like previous tomographic studies in the region (*Ramachandran et al.* 2004, *Zelt et al.* 2001), the identification of the base of the Cretaceous sedimentary rocks is rather ambiguous. The maximum velocity for sedimentary rocks is normally 5.5 km/s (e.g., *Brocher* (2005) reported velocities between 5.5 km/s and 5.6 km/s at 8.5 km depth for the Cre-

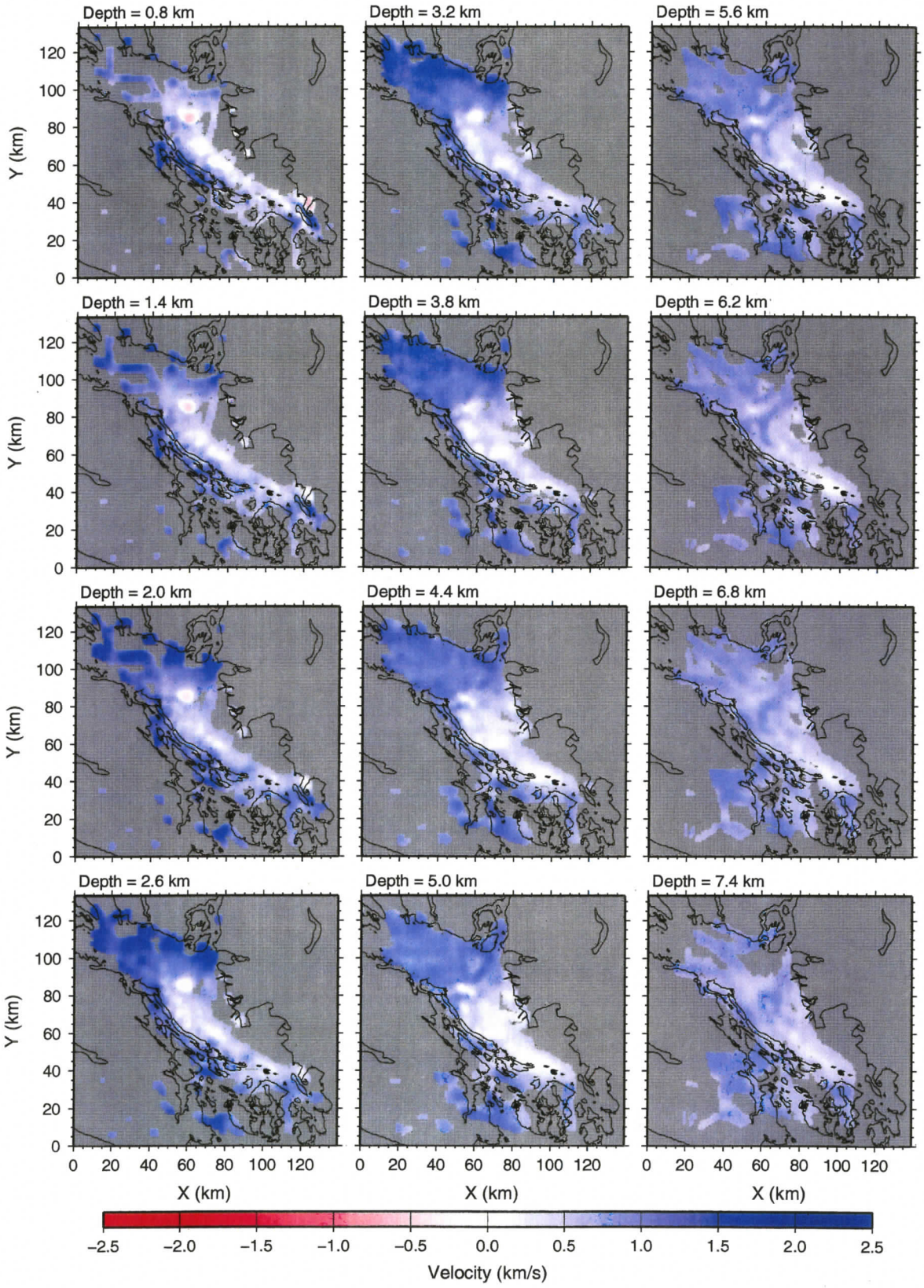

Figure 5.10: Horizontal slices through the final model, shown as perturbation from the starting model.

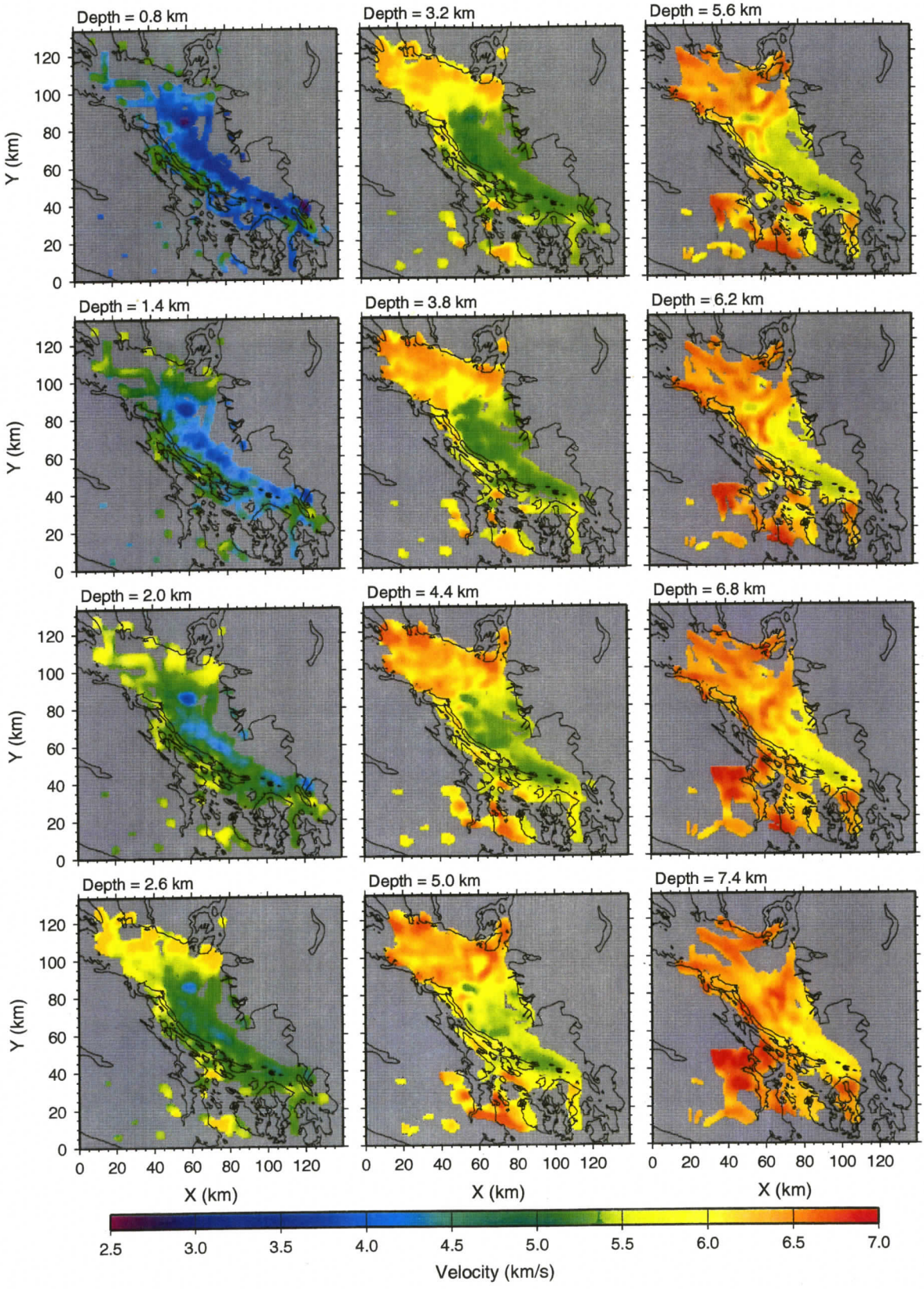

Figure 5.11: Horizontal slices through the final model.

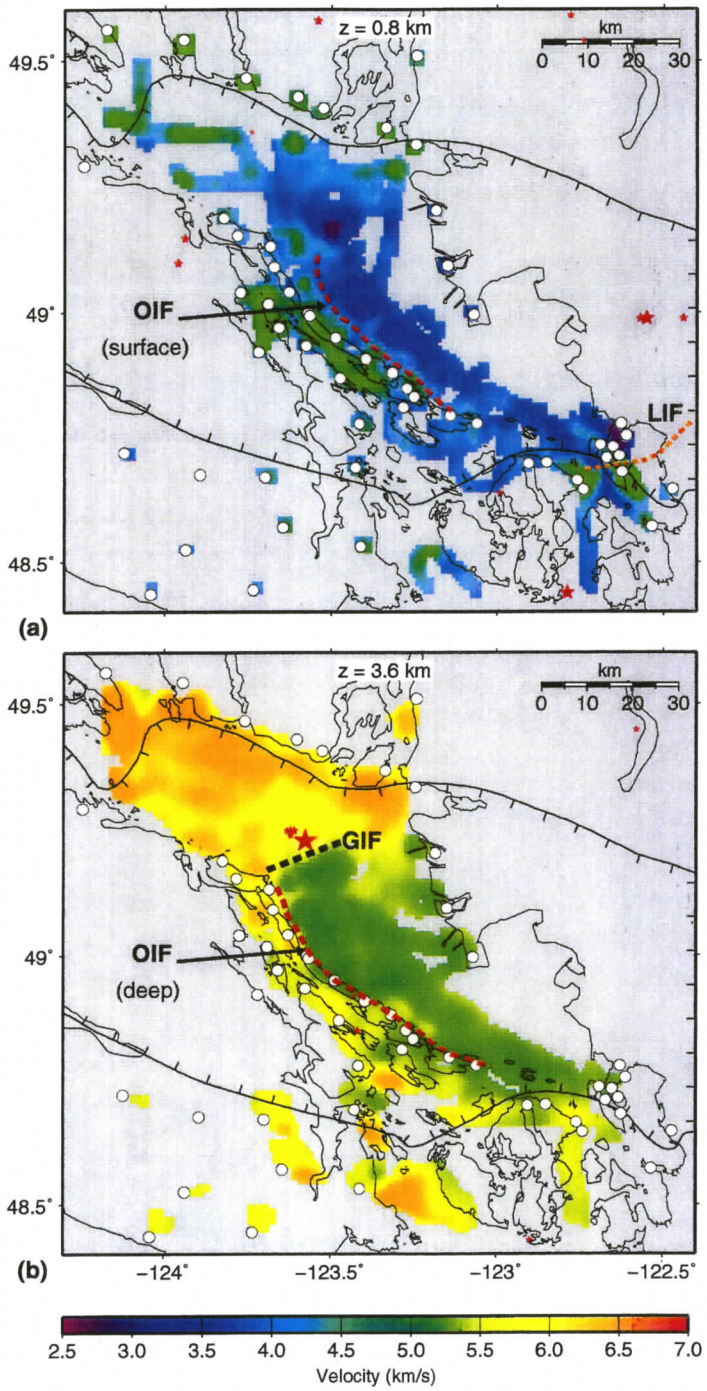

Figure 5.12: Horizontal slices through the final model at 0.8 km (a) and 3.6 km (b) depth. Receiver locations (circles) are shown for reference. The lateral velocity discontinuity within the Strait of Georgia at 0.8 km closely resembles the surface signature of the Outer Island fault (OIF) shown in the swath bathymetry map in Figure 1.6 (dashed line). At greater depth the OIF is observed farther to the west as seen in the 3.6 km depth slice. The velocity discontinuity representing the Lummi Island fault (LIF) is shown at the southeast end of the figure, where the velocity is higher to the south of the fault. The high velocity (greater than 6.0 km/s) represents the basement rocks of Wrangellia. Crustal earthquakes are shown as red stars. The 3.6 km depth slice shows the location of the 1997 earthquake. The velocity discontinuity in the vicinity of the 1997 earthquake (heavy dashed line) is interpreted as the Gabriola Island fault (GIF).

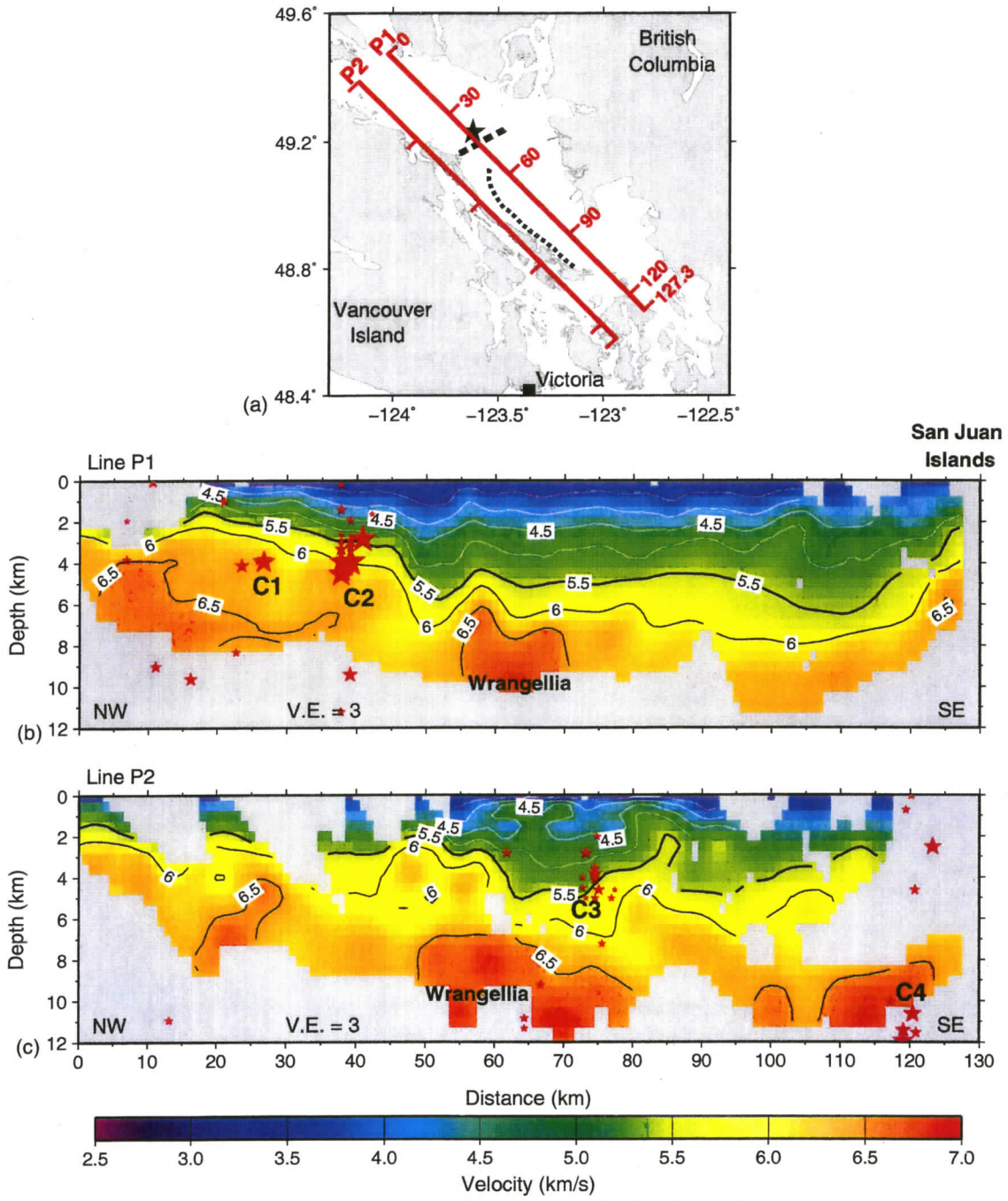

Figure 5.13: Vertical sections through the final velocity model showing velocity variations along the strait. Velocity contours are 0.5 km/s apart. The thick black line is the 5.5 km/s contour representing depth to the basement of Georgia Basin. Red stars indicate the location of the crustal earthquakes from 1985 to 2005, found within 2.5 km on either side of the profile. C1 - C4 are clusters of persistent earthquake occurrence. The location of 1997 earthquake lies in cluster C2.

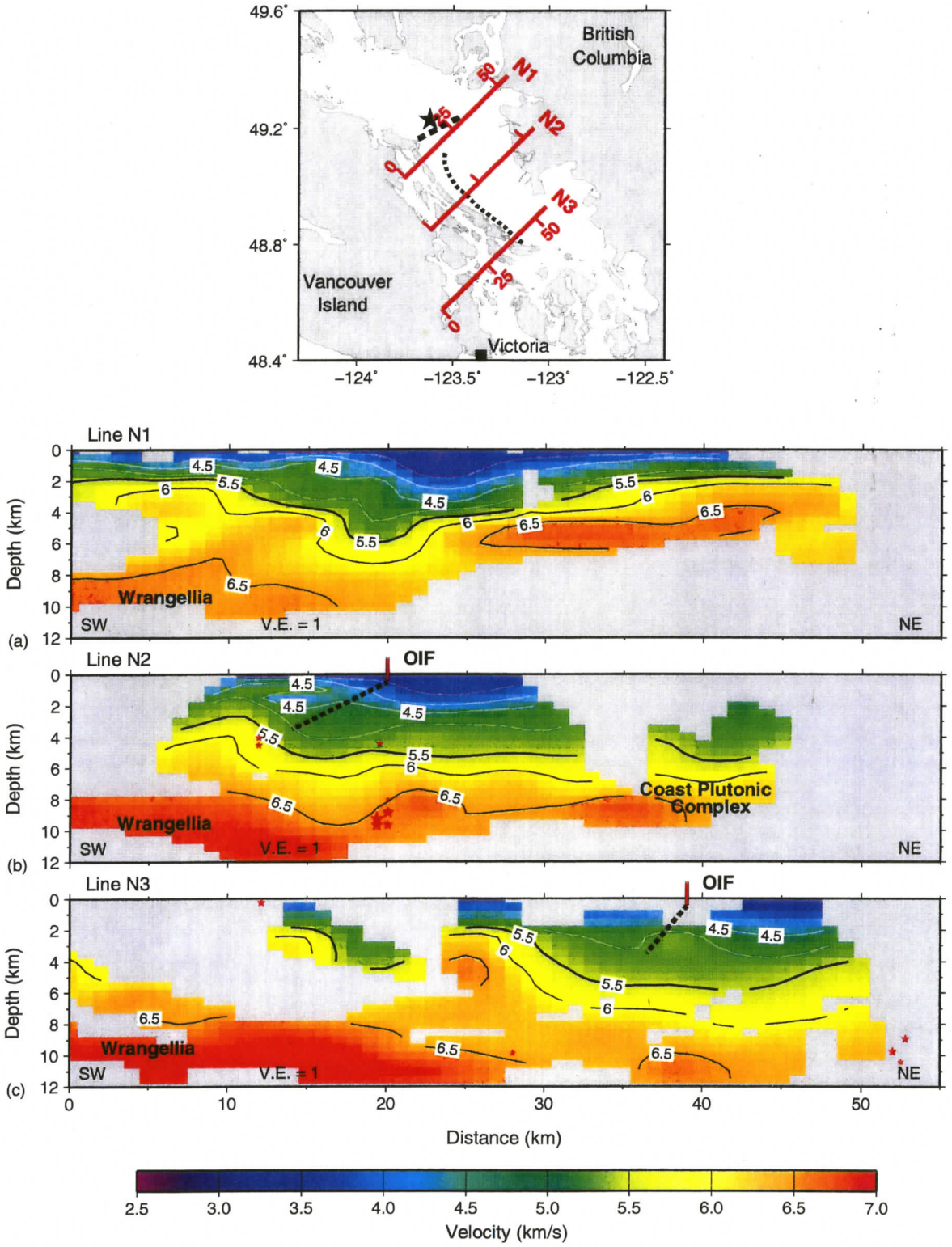

Figure 5.14: Vertical sections through the final velocity model showing velocity variations perpendicular to the strait. Velocity contours are 0.5 km/s apart. The thick black line is the 5.5 km/s contour representing depth to the basement of the Georgia Basin. The red bar indicates the surface location of the Outer Island fault. The dashed line indicates the approximate dip direction of the Outer Island fault. Crustal earthquakes found within 2.5 km of the profile are plotted as red stars.

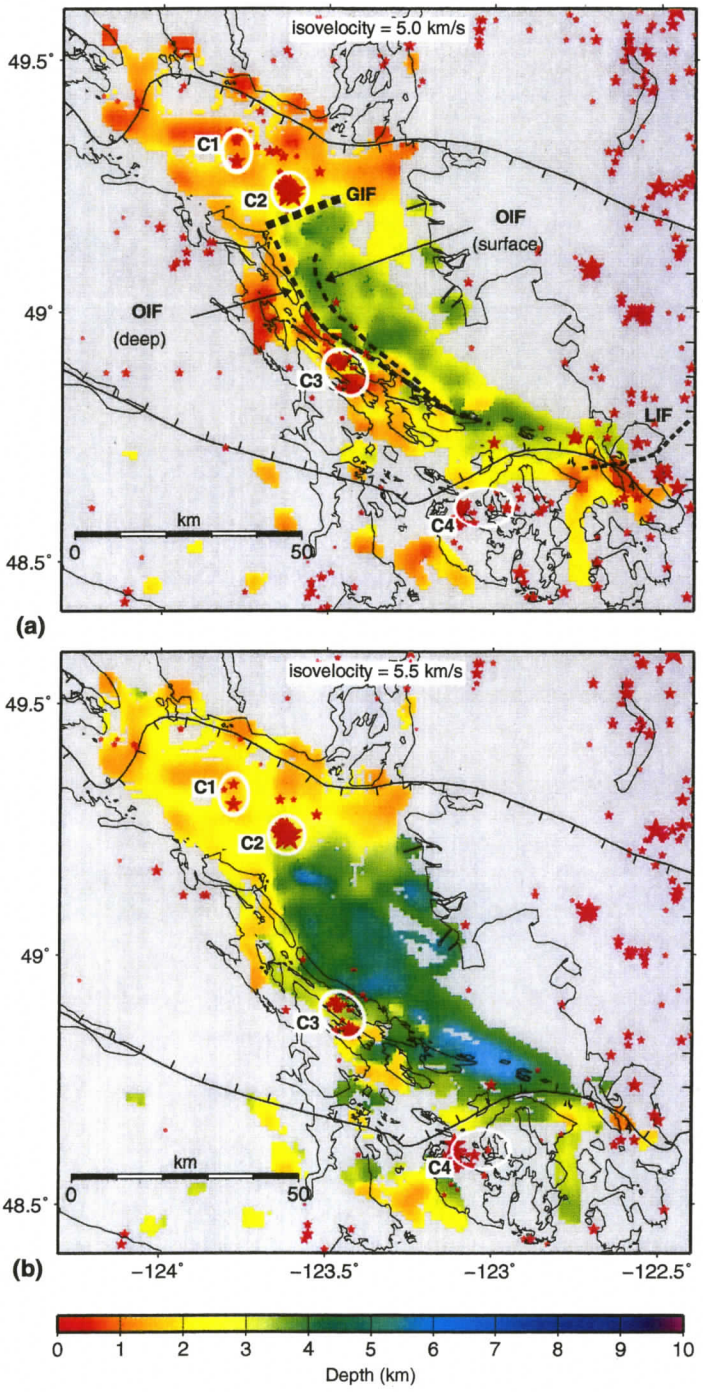

Figure 5.15: Isovelocity surface maps for velocities (a) 5.0 km/s, and (b) 5.5 km/s. Red stars indicate crustal earthquakes between 0.5 km and 5.5 km in (a) and between 2.5 km and 8.5 km in (b). The 5.5 km/s isovelocity surface has been interpreted to approximate the basement of the Georgia Basin. The basin depth is maximum at the southeast end of the strait, where it reaches 7 km depth. The surface trace of the Outer Island fault (OIF) and its occurrence at depth is shown in (a). The basement shallows to the south of the Lummi Island fault (LIF), particularly evident in (a). The basin depth increases considerably to the southeast of the earthquake cluster C2 (near the Gabriola Island fault (GIF)).

taceous sedimentary rocks in the San Francisco Bay Area). For basaltic basement rocks such as those in the Wrangellia terrane, velocities are normally greater than 6.0 km/s, but weathering and fracturing may reduce the velocity of shallow rocks to 5.5 km/s or lower. For example, just north of our study region, *Zelt et al.* (2001) interpreted velocities of 5.5-6.0 km/s down to 2 km depth as Wrangellia rocks. Furthermore, the smoothing constraints used in the tomographic method would smooth over velocity discontinuities even if there were a sharp velocity contrast between Nanaimo sedimentary rocks with velocity less than 5.5 km/s and mafic Wrangellia rocks with velocity 6.0 km/s. For our new tomographic velocity model and previous ones, the depth to basement in the area probably lies between the 5.5 km/s and 6.0 km/s contours. We thus feel that the depth to the 5.5 km/s velocity contour represents our best conservative estimate for basement depth (Fig. 5.15).

Georgia Basin exhibits considerable thickness variations along the strait. The basin thickness is much smaller in the northwest and increases towards the southeast with a maximum thickness of 6.0-8.0 km at the southeastern end of the strait (Fig. 5.15 and Line P1 of Fig. 5.13a). A sharp change in seismic velocity structure occurs near the site of the 1997 earthquake. The lower velocity sedimentary rocks (< 4.5 km/s) are only a few hundred meters thick northwest of model distance 30 km and they thicken rapidly to the southeast to a maximum of about 3 km over a distance of less than 20 km (Fig. 5.13a). The depth to the 5.0 km/s velocity contour also shows large lateral variations along the strait. Deeper basement rocks (having a Vp > 6.5 km/s) may also have significant lateral variations (e.g., near model distance 60 km along line P1, Fig. 5.13a), but our data provide only limited constraints on the deeper part of the model. The vertical section along

profile P2 (Fig. 5.13b) at the eastern edge of Vancouver Island shows more variability in structure at shallow depth compared to profile P1. This velocity variation may be due to the transition from Wrangellia rocks to the basin sedimentary rocks towards the east. This transition is more evident in the vertical sections across the strait (Fig. 5.14).

Basement ridges defined by velocity interfaces are seen most clearly in isovelocity surfaces (Fig. 5.15). The 5.5 km/s isovelocity contour reveals the most structure in the northern part of the basin with the presence of minor east-trending ridges. The San Juan Islands, another structural high, are associated with a shoaling in the velocity isocontours.

5.2.2 Identification of upper crustal faults

Abrupt velocity discontinuities within Georgia Basin appear to correlate with the inferred locations of shallow crustal faults. The most significant feature at shallow depth is the northwest-trending velocity discontinuity along the west side of the strait with higher velocity to the west than to the east. This feature correlates with the surface trace of the Outer Island fault (red-dashed line in Fig. 5.12a) as interpreted from the recent swath bathymetry data in Figure 1.6. At depth, there is an apparent westward shift of the northern part of the Outer Island fault, as evident in the 3.6 km depth velocity slice, suggesting a reverse fault dipping west-southwest. In vertical slices across the strait, the position of the Outer Island Fault at depth is indicated by the northeast-downward step in the 5 km/s contour, located at $\sim$ 15 km distance along profile N2 (Fig. 5.14b). The Outer Island fault steepens to the southeast, where the surface trace of the fault appears to coincide with the deep trace of the fault (Fig. 5.15a). The fault coincides with a major depth change in the basement, so the fault motion may also extend to the basement.

At the southeast end of the strait and to the east of the San Juan Islands, there is an east-trending velocity discontinuity possibly associated with the Lummi Island fault (e.g., Fig. 5.12a). The Outer Island fault curves eastward as it approaches the Lummi Island fault. It is possible that it directly intersects or merges with the Lummi Island fault. The apparent continuity of these two faults, within the limits of our resolution, suggests that they may represent a single, continuous, linked fault zone.

Another important discontinuity shown by the 3.6 km depth slice is a northeast-trending hinge line in the vicinity of the 1997 earthquake (Fig. 5.12b). The hinge line is identified by a rapid increase to the south in the thickness of the Nanaimo Group sedimentary rocks. Near the southern end of Gabriola Island, the hinge line correlates with the northern limit of a deformed zone in the Nanaimo sedimentary rocks mapped in swath bathymetry (Fig. 1.6). Given its association with instrumentally recorded seismicity and surface deformation of the seafloor, we infer that the hinge line region is cored by an active fault that we informally name the Gabriola Island fault.

The basin appears to be partially fault-bounded as defined by the uplifted regions of the San Juan Islands in the south and the region north of the hinge line in the north. A similar fault control pattern is also observed in the Seattle Basin further south (*Brocher et al.* 2001) and may be interpreted as the result of northeasterly compression produced by the clockwise rotation and northerly motion of the Oregon Coast block, with contraction accommodated by both thrust and strike slip faults (e.g., *Wells et al.* 1998, *Pratt et al.* 1997). The GPS (*Mazzotti et al.* 2002, 2003) and focal mechanism (*Mulder* 1995) data in Georgia Basin indicate horizontal compression along the north-northwest direction, with a small (0 - 3 mm/yr) northward motion of southern Vancouver Island with respect to

North America.

However, evidence for Holocene or Quaternary motion along the shallow crustal faults within Georgia Basin is inconclusive. The high-resolution seismic data within our study area are difficult to interpret. Near the Outer Island fault the complex basement structure produces numerous small isolated sediment "ponds", and so there are no uniform sediment packages within which subtle shifts might be identified (V. Barrie, *personal communication*, 2006). Particularly near our proposed Gabriola Island fault, the Holocene sediments are mainly Fraser-River-derived and contain large amounts of gas that often obscure reflections in shallow sediments. The focal mechanism solution of the 1997 earthquake indicated a north-dipping thrust fault (*Cassidy et al.* 2000) at this location. But in the multichannel seismic reflection data no north-dipping thrust fault could be identified. *Mosher et al.* (2000) proposed that the 1997 earthquake occurred within a zone of deformation and not on a single fault. It is possible that the Gabriola Island fault is a deep blind thrust that does not penetrate to the surface and is similar to the blind thrust in Seattle Basin (*ten Brink et al.* 2002).

5.2.3 Correlation of structure and seismicity

Shallow crustal earthquakes are mainly focused at four places within the area covered by the present model (Figs. 5.15 and 5.13). Selected earthquakes were relocated using the tomographic velocity model. Relative to locations based on the original model, these earthquakes were shifted by less than 2 km horizontally and 0.5 km vertically, distances that are smaller than the model resolution. Also, since most of the seismic energy from earthquakes travels below the sediment layers, the earthquake positions are not affected by

the shallow structures. Earthquake clusters C2 to C4 (Fig. 5.15) are comparable to those observed by *Ramachandran et al.* (2004). Cluster C1 indicates recent seismic activity in the region. *Ramachandran et al.* (2004) proposed that the earthquakes in Georgia Basin occur in regions of structural highs. Cluster C1 occurs where the top of basement rocks is highly irregular. Cluster C2, which includes the significant earthquakes of 1997 and 1975, lies near the Gabriola Island fault and the hinge line defined by a rapid increase in basin thickness to the southeast. The basement near cluster C3 shallows immediately to the southeast of the cluster (Fig. 5.13b). There are also significant velocity variations near the cluster due to the transition from Wrangellia rocks to basin sediments (Fig. 5.15). The region around cluster C4, beneath the San Juan Islands, is poorly constrained in our model. However, to the east of the cluster and beneath the San Juan Islands, basement is clearly uplifted.

5.3 Summary

To investigate the Georgia Basin we derived a new minimum structure 3D velocity model for the crust beneath the Strait of Georgia from tomographic inversion of first arrival traveltimes. The tomographic results provide a well-constrained upper crustal velocity structure to about 7 km depth. The thickness of Cretaceous to Tertiary sedimentary rocks within Georgia Basin is defined by the depth to basement velocities of 5.5 km/s. Along a hinge line trending northeast from Gabriola Island, sedimentary rocks thicken rapidly to the southeast from 2-3 km near the hinge line to a maximum of 6.0-8.0 km at the southeast edge of the strait. A 60-km-long northwest-trending, southwest-dipping discontinuity at shallow depth on the west side of Georgia Strait corresponds to the Outer

Island fault. An east-trending velocity discontinuity east of San Juan Island, 20 - 30 km in length, correlates with the mapped location of the Lummi Island fault. At its southeast end the Outer Island fault steepens as it curves eastward toward the Lummi Island fault. Fault motion probably involves basement, since the fault coincides with a major depth change in the basement and localized concentrations of seismicity occur in the regions of rapid change in basin thickness. The location of the M = 4.6 1997 earthquake lies close to the hinge line, suggesting that the hinge region is cored by a fault, which we informally name the Gabriola Island fault. Given the existence of the Outer Island, Lummi Island, and the inferred Gabriola Island faults, Georgia Basin is interpreted to be largely a fault-bounded structure similar to the Seattle Basin to the south.

Chapter 6

Seismic studies of northern Cascadia margin hydrates

6.1 Introduction

This chapter describes analysis of ocean bottom seismometer (OBS) and streamer data to image the velocity structure of the accretionary prism sediments containing gas hydrates. A two dimensional (2D) velocity model beneath multichannel seismic line 89-08 is constructed from simultaneous traveltime inversion of OBS and single channel data. The ray trace traveltime inversion algorithm of *Zelt and Smith* (1992) is used to obtain both compressional and shear wave velocity models from the OBS vertical and horizontal components, respectively. Log data from IODP drill hole site 1327 are correlated with the results from the seismic analysis to estimate the hydrate concentration in the pore space.

6.2 P-wave velocity modelling

Conventional seismic reflection data from single- and multichannel surveys are useful to reconstruct the compressional wave velocity field and to explore the detailed possible lateral variations in structure. However, regions with strong seismic attenuation (e.g., layers containing gas beneath the highly reflective BSR) are difficult to image using the above datasets. In those cases, wide angle seismic data from OBSs can provide better images for the structures deeper than the BSR by utilizing the refracted arrivals (if present) and/or the shear wave data.

The seismic reflection data provide a very good structural image of the subsurface, but the accuracy of velocities is limited by the source-receiver offset, particularly for deeper horizons. Along a vertical incidence ray path, an increase in both the interface depth and the velocity above the interface will produce the same traveltime in the seismic time section. On the other hand, wide angle data from OBSs provide accurate velocity information but a poorly-resolved structural image. Thus, combining both the normal incidence and the wide angle data sets can provide improved constraints on both the velocity and the interface depth.

6.2.1 Event identification

The 2005 seismic survey near IODP Site 1327 provided single channel reflection data coincident with wide-angle data recorded on an array of 10 closely-spaced OBSs. Reflection events that originated from the same interface in both single channel and OBS data were identified and picked. The selection of the events was based on their consistency

throughout the modelling area. Single channel seismic data from line 3 (location in Fig. 2.7) coincident with the line of OBS deployments were used for the velocity analysis. Three distinct events (two events from the upper slope sediments and the BSR) were identified below the seafloor (Fig. 6.1). The events were picked manually out to offsets of more than 4 km from the OBS locations. Uncertainties were assigned to the traveltime picks based on the signal-to-noise ratio. The seafloor arrivals were assigned an uncertainty of 2 ms. For shallow events, E1 and E2 (Fig. 6.1), pick uncertainties were 5 ms and 6 ms, respectively. For the BSR, a pick uncertainty of 4 ms was assigned.

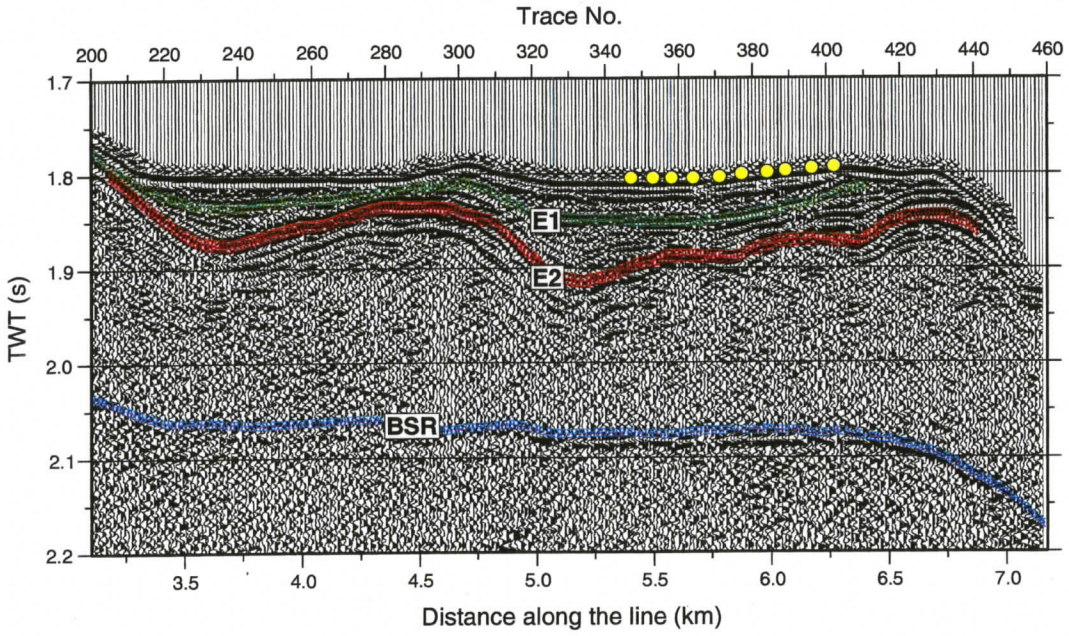

Figure 6.1: Reflection events selected for the traveltime inversion. OBS positions are indicated by yellow circles.

Wide-angle data from all ten OBSs were used in the velocity analysis. The OBS data in the mid-slope region contain only reflections and almost no refraction events, consistent with other OBS surveys in this area (*Hobro* 1999, *Zykov* 2006). Hydrophone (pressure) components were chosen for picking. To facilitate the event identification, the OBS and the SCS data were aligned side by side to match the seafloor and the BSR. Then the OBS

reflection events at zero offset corresponding to the single channel events were selected. An example is shown in Figure 6.2. Picks were obtained up to 2.5 km on either side of the OBS locations (Fig. 6.3). Beyond this distance, OBS arrivals are difficult to identify due to weak signal and interference with other arrivals. Pick uncertainties, similar to the uncertainties of the single channel events, were assigned to the OBS arrivals.

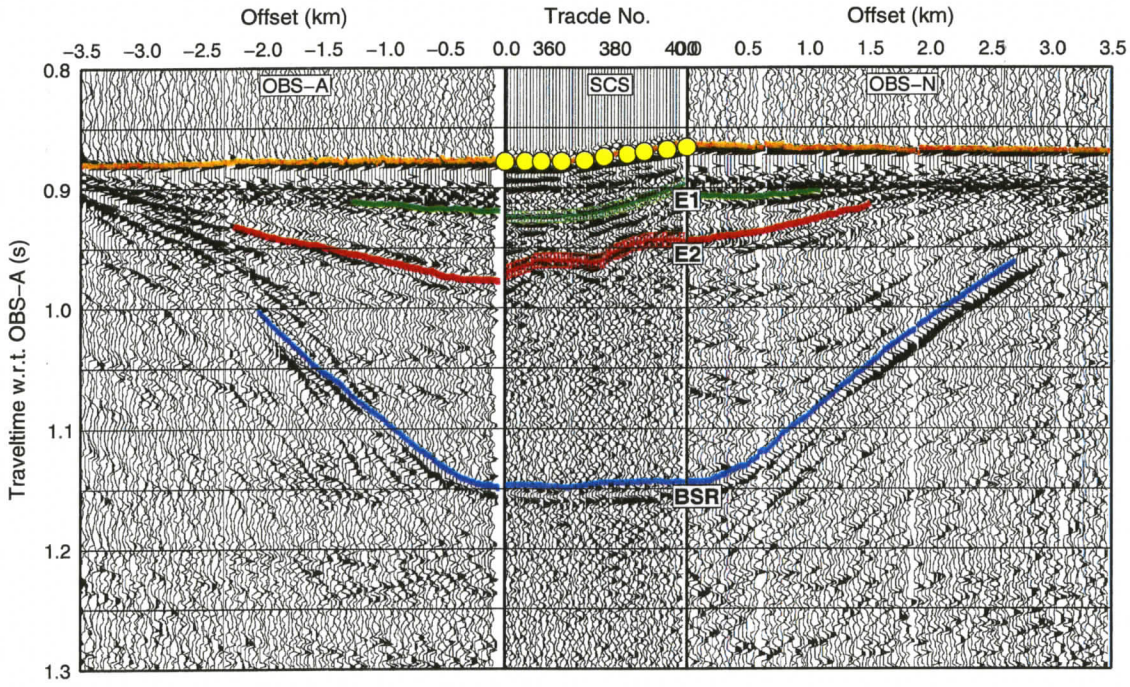

Figure 6.2: Event identification by aligning OBS and single channel data. The middle panel is single channel data.

6.2.2 Modelling

The velocity model was obtained using the traveltime inversion algorithm of *Zelt and Smith* (1992), which employs a forward ray-tracing step and a damped least square inversion step to modify the model parameters (velocity and depth) to minimize the difference between the observed and the predicted traveltimes. Since traveltime inversion is a non-linear problem, the algorithm first determines the ray paths in the initial model and then

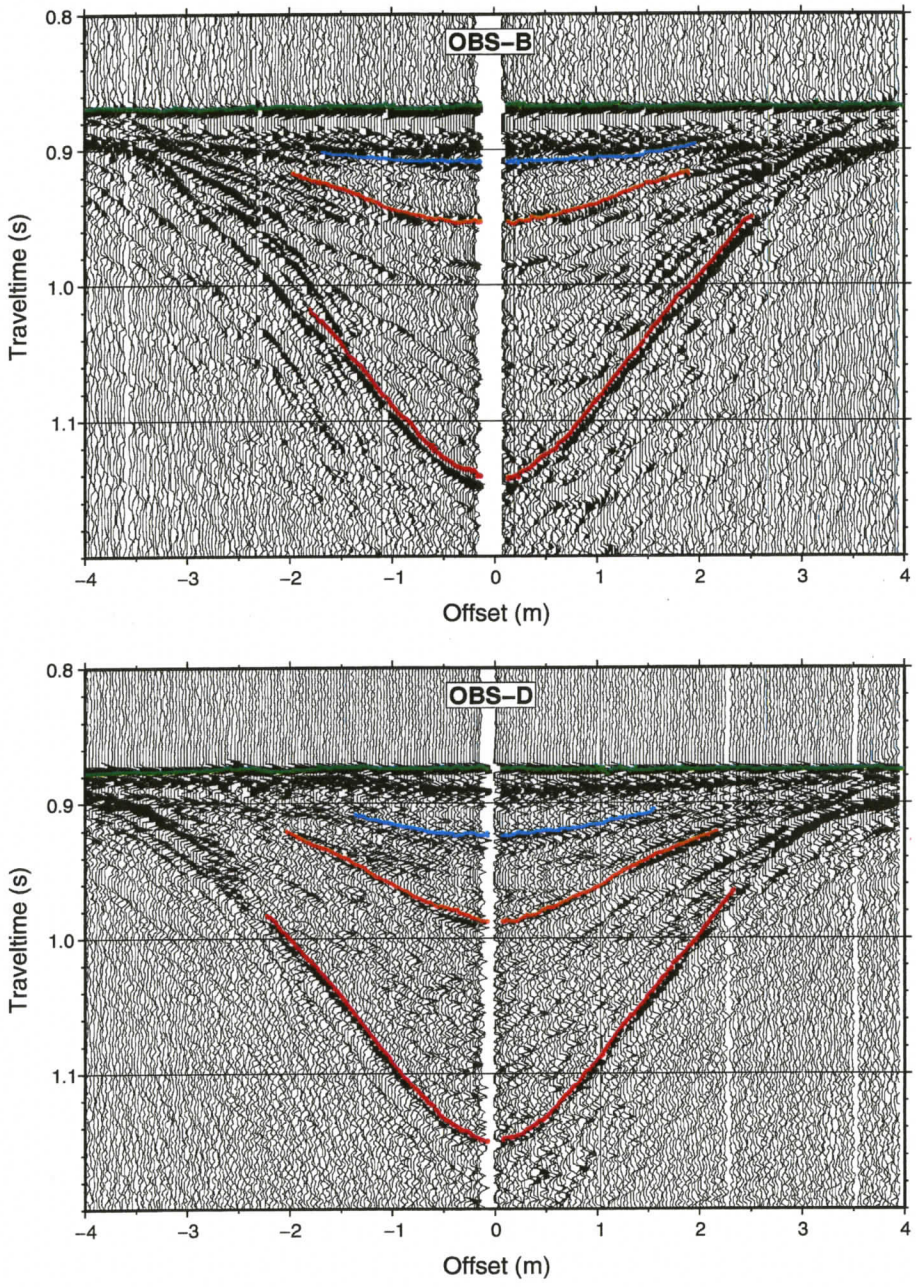

Figure 6.3: Examples of OBS (hydrophone) data showing traveltime picks for the reflection events used in velocity modelling.

updates the velocity model assuming stationary rays. The initial P-wave velocity model was constructed from the single channel seismic data. The traveltime picks were converted to depth using the velocity information from previous studies in the area. The

initial velocity gradients were 0.50 s^{-1} for layer 1, 0.80 s^{-1} for layer 2, and 1.3 s^{-1} for layer 3. After initial forward modelling, layer velocities and interface depths were adjusted in a linearized inversion scheme that minimized the difference between the observed and calculated traveltimes. All the OBSs were included in the inversion (Fig. 6.4). A layer stripping approach was followed where the top layer was modelled first and then held fixed. The ray-tracing and inversion steps were repeated until the solution converged, i.e., the root-mean-square (RMS) traveltime misfit fell to the order of the pick uncertainties and the normalized χ^2 misfit approached 1. For the final model, an RMS traveltime residual of 6 ms was achieved with a normalized χ^2 value of 1.6. The velocity gradients for the final model were 0.50 s^{-1} for layer 1, 0.88 s^{-1} for layer 2, and 1.62 s^{-1} for layer 3. Overall, the perturbation from the starting velocity model was very small.

The uncertainties in the velocity model from the traveltime inversion were estimated using the procedure of *Katzman et al.* (1994). Uncertainty of a particular model parameter was estimated by perturbing its value from that of the final model and holding it fixed while allowing the other parameters to vary during inversion. The parameters were perturbed until the traveltime residual and the normalized χ^2 increased significantly from the value of the final model. In particular, the BSR depth and the velocity above the BSR were examined. The velocity gradient for this layer was fixed at the final value while allowing lateral variations in velocity. From Figure 6.5, the velocity value for the hydrate layer can probably be accepted within 3 % uncertainty. For an average velocity of $\sim$ 1800 m/s in the $\sim$ 160-m-thick layer above the BSR, this results in an average velocity error of about $\pm$ 50 m/s and an average depth error of less than 5 m.

Following *Zelt and Smith* (1992), resolution of the model parameters was estimated

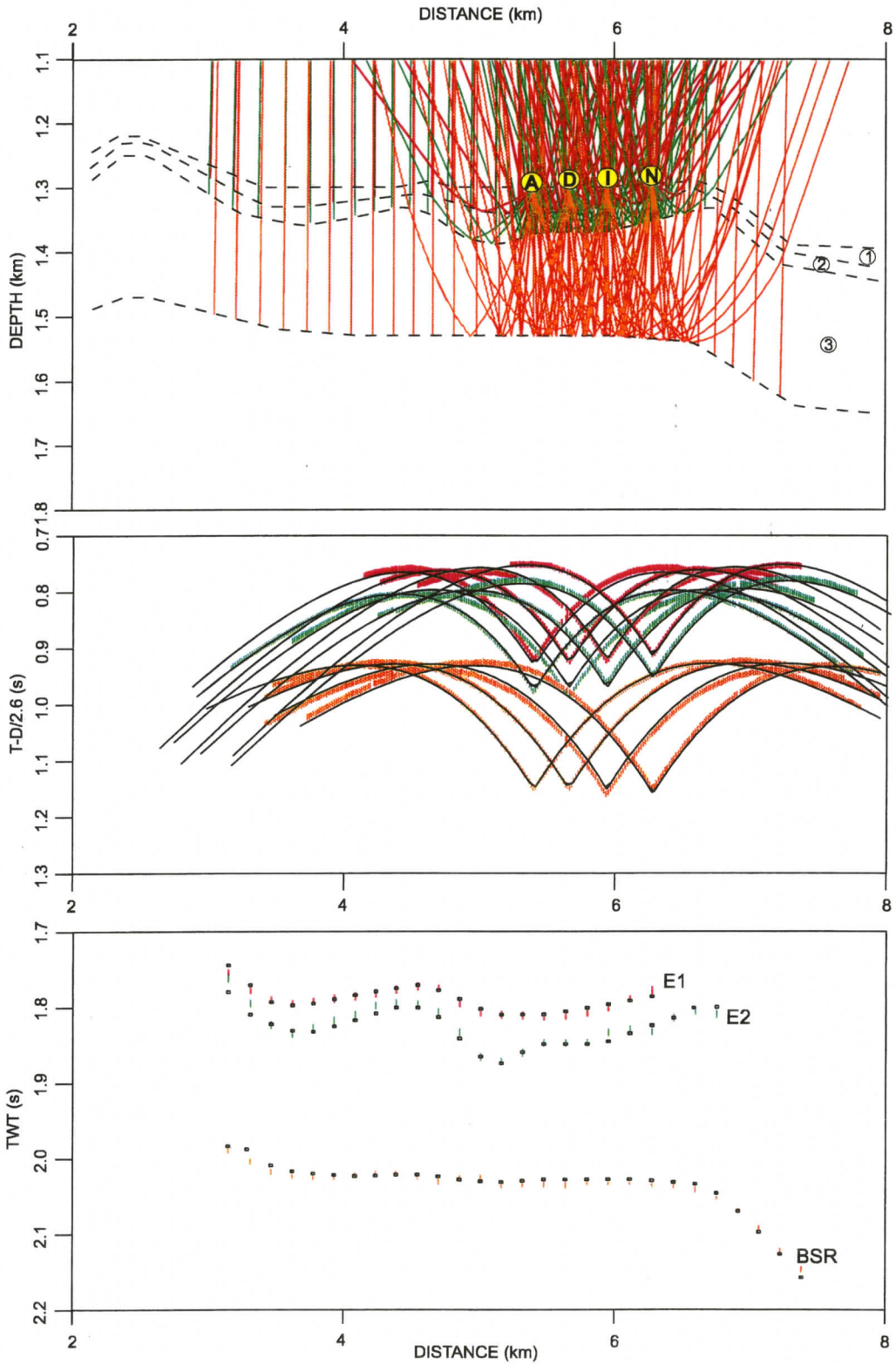

Figure 6.4: The final ray-tracing and traveltime fit for the P-wave velocity model. All the ten OBS were used simultaneously with the single channel seismic reflection data. For clarity, only 4 OBS are shown and the OBS (middle panel) and the single channel (bottom panel) times are plotted separately. The OBS times are reduced with a velocity of 2.6 km/s. The small vertical bars (coloured) indicate the picks and their uncertainty range. The final RMS residual was 6 ms with a normalized χ^2 value of 1.6.

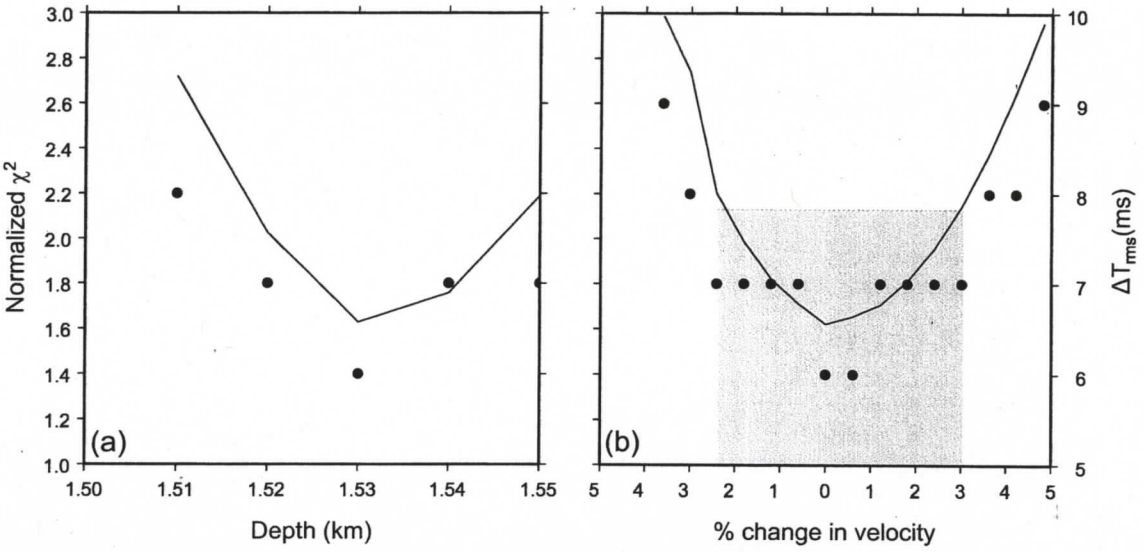

Figure 6.5: Normalized χ^2 misfit (line) and RMS traveltime residual (dots) with respect to change of BSR depth (a) and velocity above the BSR (b). For velocity, a conservative estimate of uncertainty is $\pm 3\%$, as indicated by the shaded box in (b).

by analyzing the diagonal elements of the resolution matrix. Ideally, a value of 1 implies perfect resolution and values less than 1 indicate a spatial averaging of the true earth structure by a linear combination of model parameters. According to *Zelt and Smith* (1992), a resolution value of greater than 0.5 indicates that the model parameter is well resolved. It should be noted that this method of estimating model resolution does not take into account the improvement in constraint due to crossing of ray paths. Figure 6.6 shows the resolution values of the depth and velocity nodes for the final velocity model. The depth nodes show a better resolution than the velocity nodes. Between 5 km to 6.5 km model distance (below the OBS locations), the depth nodes are very well resolved.

6.2.3 P-wave velocity model

The final P-wave velocity model includes three layers above the BSR (Fig. 6.7). The model is constrained over a distance range of about 4 km. The maximum thickness of the

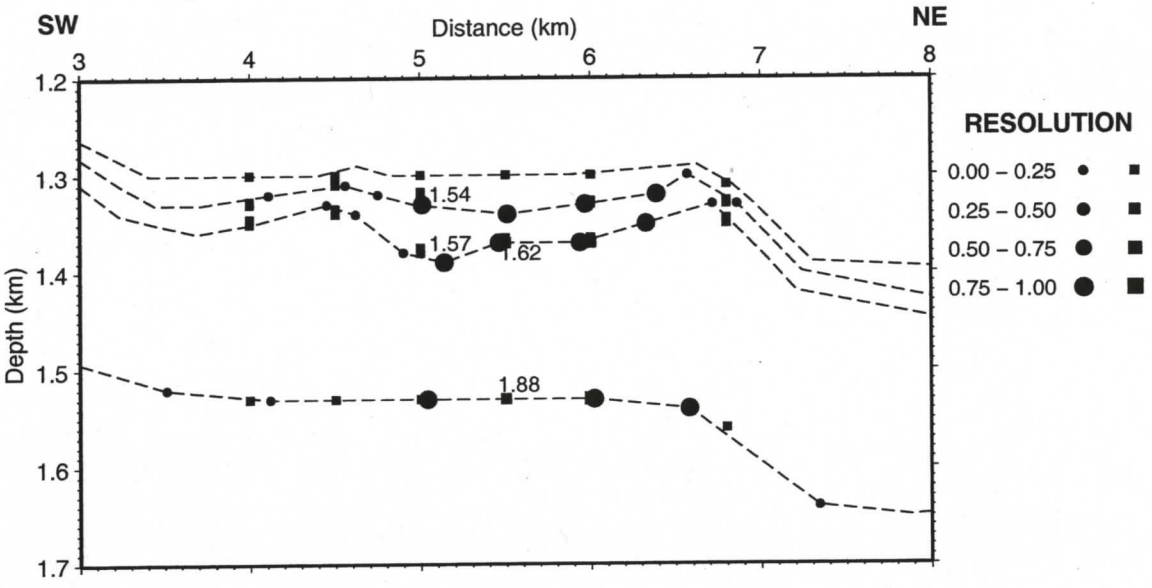

Figure 6.6: Resolution of depth (circle) and velocity (square) nodes for the final model. Dashed lines represent the model interfaces. Velocity values for selected nodes are given in km/s.

uppermost layer is about 40 m. It has very low velocities of 1.50 to 1.52 km/s representing very unconsolidated marine sediments (Fig. 6.8). The middle layer, also containing slope sediments, has a varying thickness with an average value of about 50 m and has slightly higher velocities (1.54 to 1.58 km/s) resulting from progressive sediment compaction with increasing depth. The bottommost layer has an average thickness of about 160 m. It constitutes consolidated sediments of the accretionary prism and has considerably higher velocities varying from 1.62 km/s at the top to 1.88 km/s at the BSR. The BSR depth is about 230 m. This value, which is well-constrained with an uncertainty of less than 5 m, agrees well with the BSR depth inferred from the VSP data at Site 889B and from the sonic data at Site U1327E (Fig. 6.7). However, the VSP data at Site U1327 implies that the BSR depth is at about 250 m; it seems likely that the disagreement is due to measurement error associated with the VSP data. The boundary between the slope and accreted sediments is not well defined in the seismic data. Based on core and downhole

log data from ODP Site 889 and IODP Site 1327, *Riedel et al.* (2006a) interpreted the boundary at about 90 m below seafloor.

However, the single channel reflection data along line 3 suggests that the boundary is slightly deeper. In Figure 6.8, it is interpreted to lie 30 - 40 m below the second layer. The layer below the BSR is believed to have a very low velocity due to the presence of free gas, but is unexplored by the P-wave data. The model provides higher resolution, especially at shallower depths, compared to the results from previous studies in this area (e.g., *Hobro* 1999, *Hobro et al.* 2005). Overall, this result matches well with the sonic log data from the ODP Site 889 and the IODP Site U1327.

6.3 S-wave velocity modelling

The primary objective of the S-wave study is to explore structures beneath the BSR, which are virtually absent in the single channel reflection and OBS vertical component data. The main reason for this is the strong attenuation below the BSR due to the presence of free gas. However, S-wave propagation is more dependent on the sediment rigidity provided by grain-to-grain contacts and less sensitive to the presence of gas within the sediment pore spaces. The horizontal components of the OBS data show strong arrivals at greater depths (Fig. 6.9), which are assumed to be produced by conversion of the downward going P-waves at reflection interfaces. These arrivals can potentially provide information on the structures below the BSR. Also, the S-wave velocity (V_s) contrast between pure methane hydrate (1890 m/s) and hydrate-free shallow marine sediments (100-600 m/s) is very high (*Waite et al.* 2000). Thus, any increase in V_s can be attributed to the presence of gas hydrates.

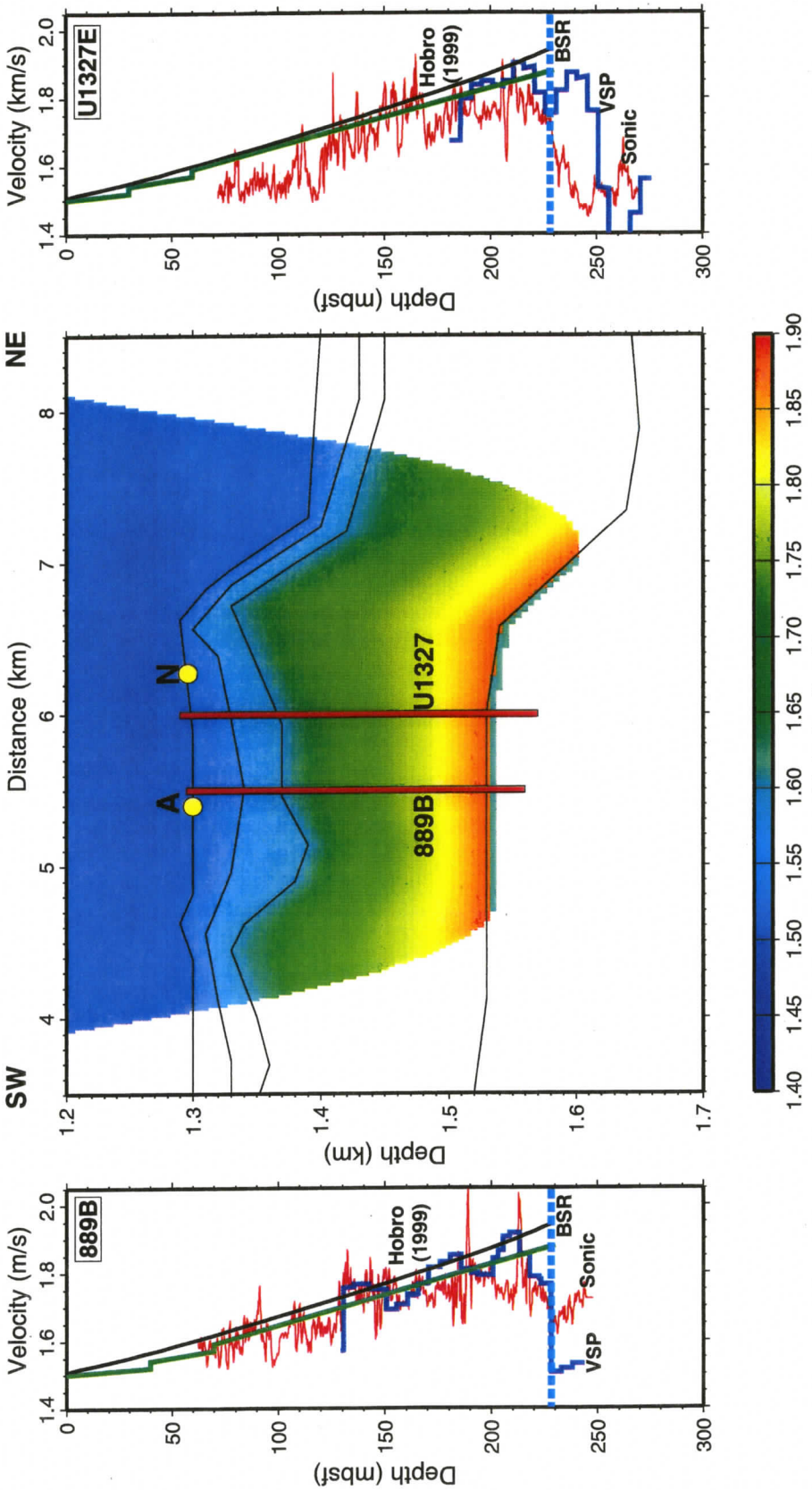

Figure 6.7: Final velocity model from traveltime modelling (centre) and the velocities from ODP/IODP drillholes (sonic and VSP). The velocity-depth profiles at the drillhole locations were extracted from the final velocity model and plotted (in green) with the drillhole data. A BSR depth of 230 m is inferred from the seismic velocity model, the VSP data at Site 889 and the sonic data at Site U1327; however, the BSR from the VSP data at Site U1327 is anomalously deep. Also shown is the previous study by *Hobro* (1999).

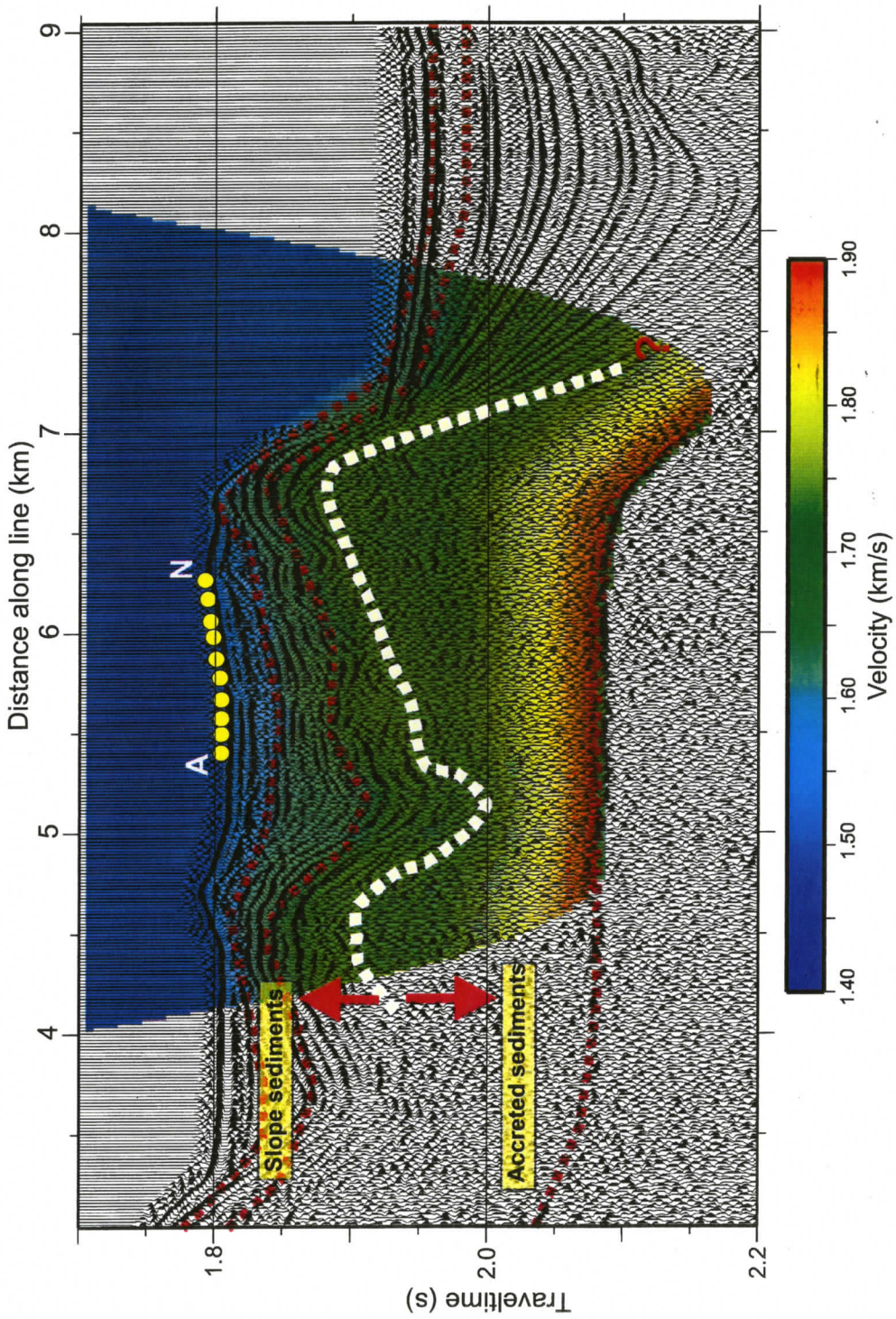

Figure 6.8: Time-migrated single channel seismic data plotted with the final velocity model. The red dashed lines are the interfaces (from the slope sediments and the BSR) used in the modelling. The white dashed line indicates the approximate interface between the slope and accreted sediments.

For the S-wave velocity model, only forward modelling was carried out as it is difficult to identify the exact converted phase in the OBS radial components. Also, the correlation of P-wave events on the OBS hydrophone/vertical component and the S-wave events on the radial components is difficult as they have different time scales and have different amplitude variations with offset. Seven S-wave arrivals were identified based on their consistency across different OBSs (Fig. 6.9). The three PS arrivals (E_s1, E_s2 and E_s4) that were assumed to be generated from the P-wave layer interfaces were identified at about 1.2, 1.38, and 1.7 s at minimum offset in the horizontal component data (Figs. 6.9). The event E_s4 is the PS arrival corresponding to the BSR. The fourth PS arrival (E_s3), whose corresponding P-wave arrival was unclear in the vertical component data, was identified at about 1.55 s at near offset. Below the BSR, three more PS arrivals were identified at minimum-offset times of 1.85, 2.0 and 2.2 s. Since the exact arrival times of the PS arrivals were uncertain, they were assigned large picking errors. For the first two events (E_s1, E_s2), an uncertainty of 20 ms was assigned. Events 3, 4 and 5 (E_s3, E_s4 and E_s5) were assigned a pick uncertainty of 30 ms each, while events 6 and 7 (E_s6, E_s7) were assigned 40 ms uncertainty.

To model S-waves, the ray-trace algorithm of *Zelt and Smith* (1992) requires a P-wave velocity model and Poisson's ratio for each layer. Thus, a preliminary S-wave velocity model was obtained from the P-wave velocity model. The Poisson's ratio for each layer was obtained from the P- and S-wave sonic log data from the IODP Site U1327 using the following relation:

$$\nu = \frac{(V_p/V_s)^2 - 2}{2\left[(V_p/V_s)^2 - 1\right]} \tag{6.1}$$

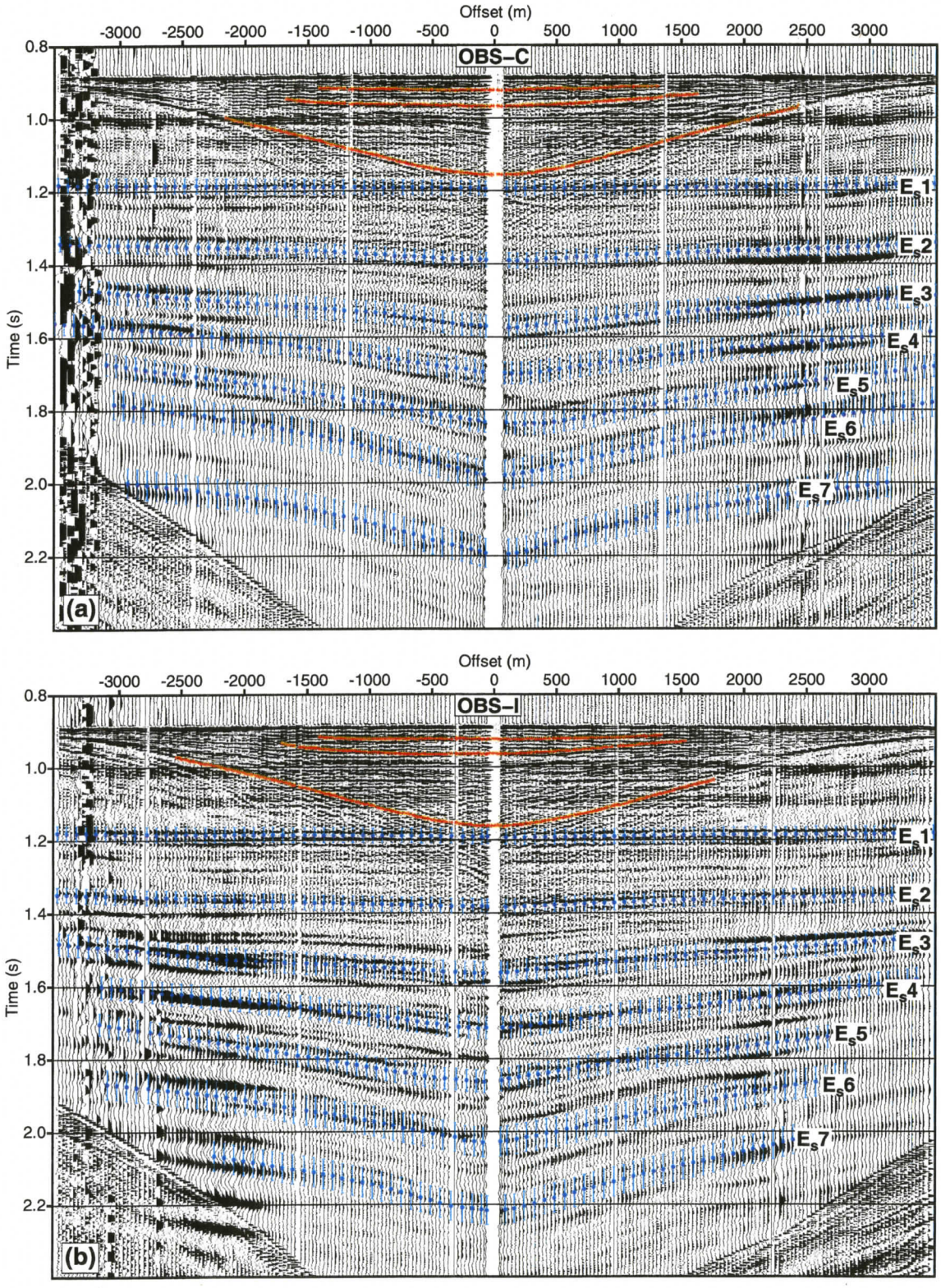

Figure 6.9: S-wave picks (blue dots) from horizontal components of OBS-C (a) and OBS-I (b) plotted with pick uncertainties (blue vertical bars). Also plotted are the P-wave arrivals from the respective vertical components (in orange).

where ν is the Poisson's ratio. For very shallow layers (less than 75 m depth), no drillhole data were available. Thus, Poisson's ratio values of 0.485 and 0.48 were assigned to the top two layers that correspond to unconsolidated water-saturated sediments.

A limitation of *Zelt and Smith* (1992)'s algorithm is that it requires constant Poisson's ratio within each layer. Thus the third layer in the P-wave velocity model, which has a large velocity gradient, was approximated by a number of thin layers. Since the number of S-wave arrivals at shallower depths (less than the assumed mode-converted BSR time at 1.7 s) is more than the number of P-wave arrivals, it was assumed that these thin layers also produced PS waves. During ray-tracing, the depths and Poisson's ratios for layers above the BSR were perturbed keeping the P-wave velocity model fixed until an acceptable fit was obtained with the observed arrivals in the horizontal component. For modelling below the BSR, both the layer depths and the Poisson's ratios were perturbed until a satisfactory fit was obtained. PS ray-trace modelling was done for OBS C, and I. Only the results from OBS-C are presented here (Fig. 6.10). The combined RMS traveltime residual for OBS C is 17 ms, with a a normalized χ^2 of 1.05. Ray-trace modelling for OBS-I using the same model as above produced equally satisfactory fit.

As expected, the S-wave velocity provides a good match with the drillhole data (Fig. 6.11). It increases more or less continuously with depth and reaches a value of about 530 m/s at the BSR. Compared to the P-wave velocity, which decreases sharply below the BSR (observed from the drillhole data), the decrease in S-wave below BSR is not significant. In the shallow slope sediments the V_p and V_s values match very well with the sediment velocity values predicted by *Hamilton* (1979), but the deviation from the *Hamilton* (1979) model is evident in the zone of 120 - 230 m below seafloor. The V_p/V_s ratio decreases

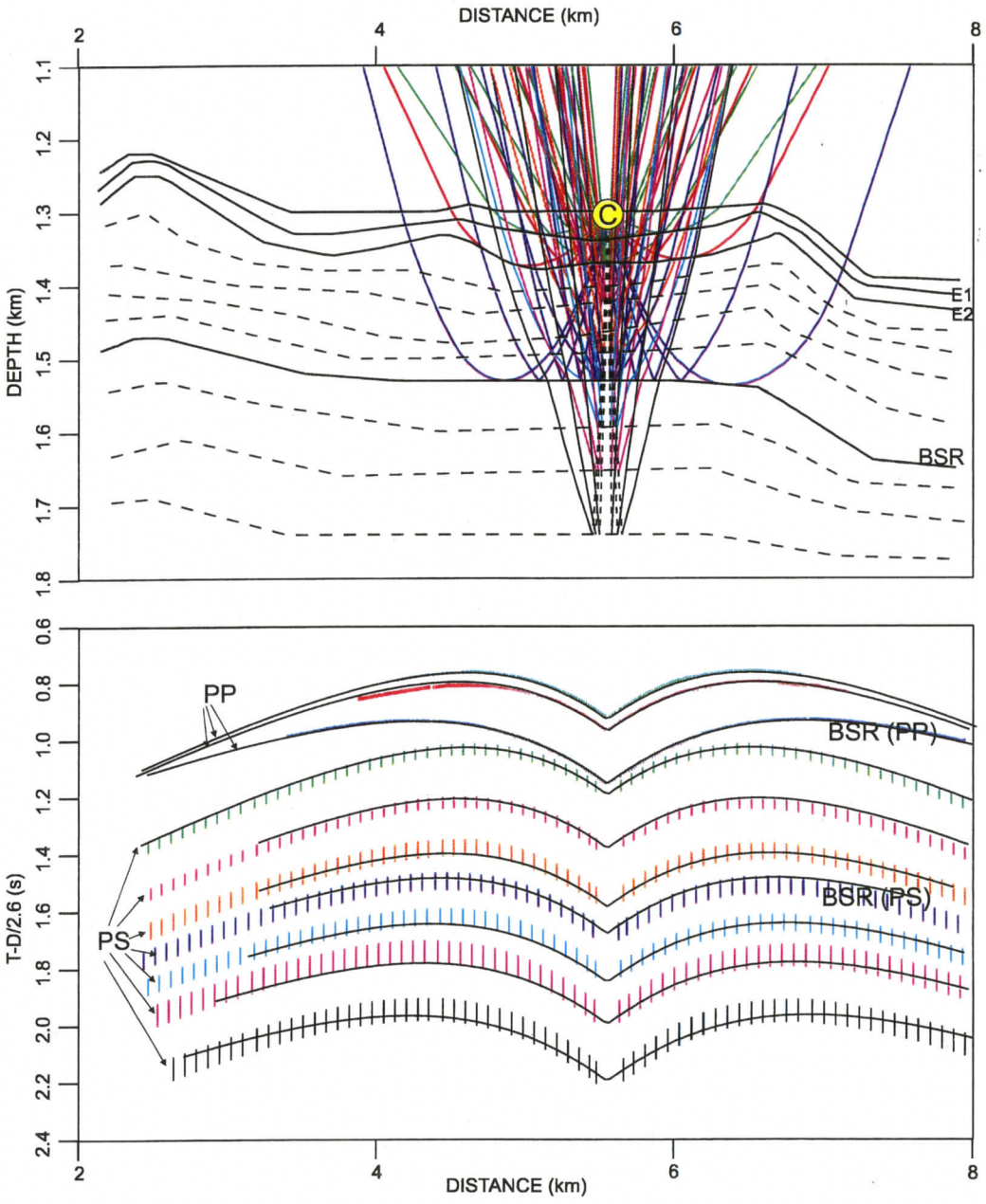

Figure 6.10: PS-wave ray tracing on the radial component of OBS-C showing PP (solid) and PS (dashed) ray paths. The PS arrivals are mode-converted after reflection from the layer boundaries. The dashed layer interfaces above the BSR were inserted to approximate a gradient in Poisson's ratio. Layer boundaries below the BSR are interfaces interpreted from PS waves.

continuously from the seafloor downwards, from a value of 6.5 to about 3.2 at the BSR. The final model from the S-wave ray tracing provides information to about 200 m below the BSR. However, due to large pick uncertainties, the velocity values below the BSR are only approximate (with errors up to ± 100 m/s).

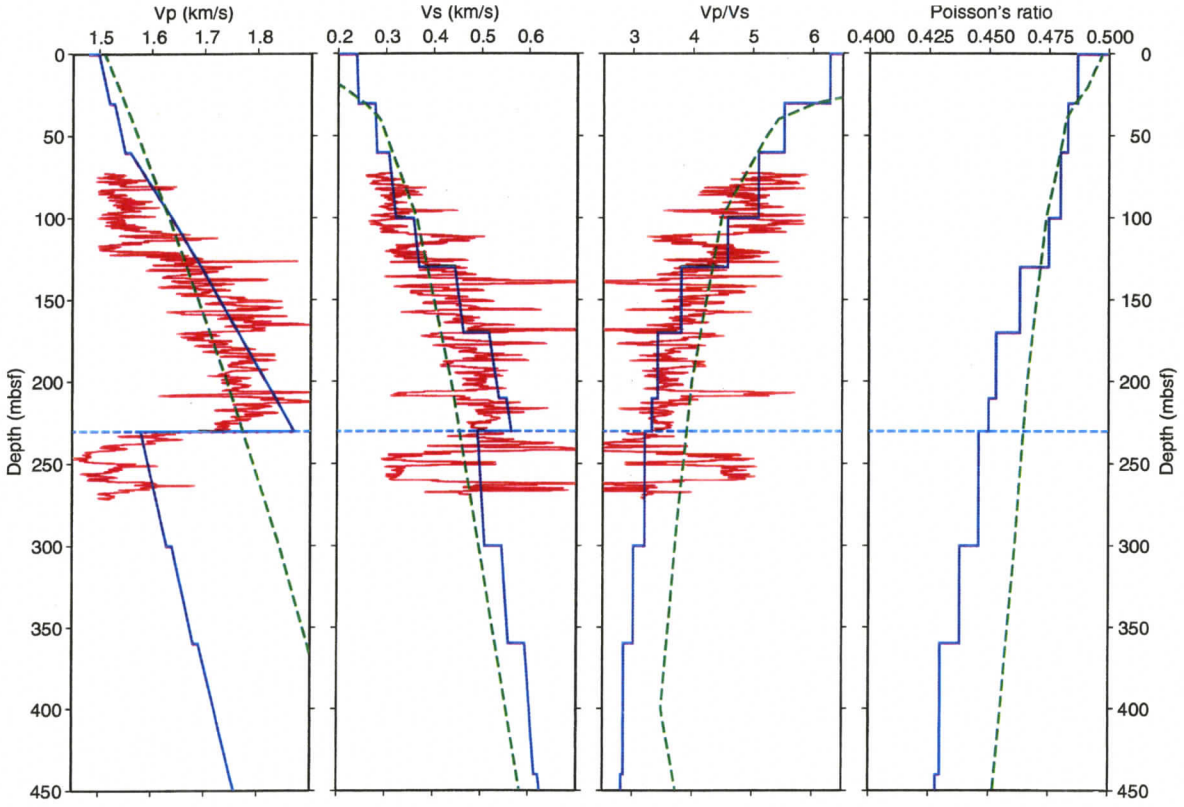

Figure 6.11: V_p and V_s values obtained from ray-trace modelling (in blue) plotted with the drillhole data from IODP Site U1327E (in red) and *Hamilton* (1979) models (in green). The Poisson's ratio values used for the S-wave modelling is plotted in the last panel. The dashed line (cyan) represent the approximate depth of the BSR.

Figure 6.12 shows the crossplot of V_p versus V_s along with the Hamilton velocity model and the mudrock line of *Castagna et al.* (1985). The mudrock line is an empirically derived relationship between V_p and V_S for water-saturated sediments (mostly silicates). However, in gas-charged sediments the mudrock equation underestimates V_s due to the decrease in V_p. The crossplot of V_p versus V_s can easily distinguish the hydrate-bearing

sediments above the BSR from the gas-charged sediments below. As evident in the figure, the $V_p \sim V_s$ trends for both the hydrate- and gas-bearing sediments differ significantly from the mudrock line. The hydrate bearing layer has a similar trend as the Hamilton line at intermediate depths, but the trend deviates near the base of the layer. A first-order linear trendline was calculated for the layers above the BSR, producing

$$V_p = 1.08V_s + 1253.3;\ V_p \text{ and } V_s \text{ are in m/s.} \tag{6.2}$$

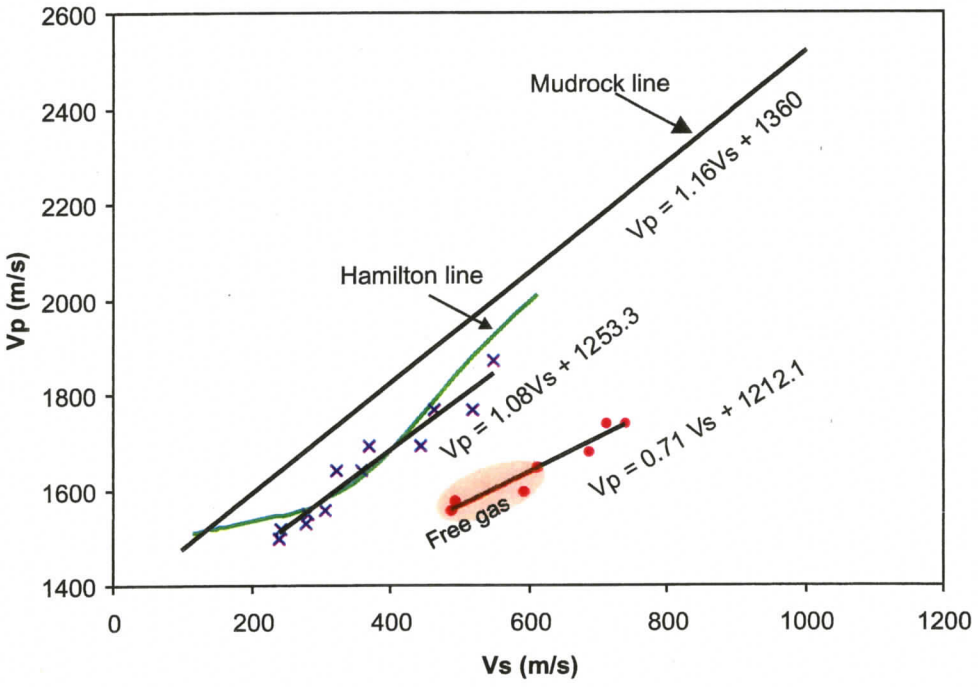

Figure 6.12: Crossplot of P- and S-wave velocities derived from the raytrace modelling plotted with *Castagna et al.* (1985)'s mudrock line and the Hamilton velocity model. Crosses and dots represent the velocity values above and below the BSR, respectively.

6.4 Hydrate concentration and distribution in pores

6.4.1 Concentration estimates based on P-wave velocities

Hydrate concentration was estimated from the final P-wave velocity model obtained from the traveltime inversion. Since the presence of hydrate in the sediment pore spaces increases the sediment velocity, the amount of hydrates can be estimated from the velocity difference relative to the background no-hydrate velocity. Numerous models have been proposed for estimating hydrate concentration from velocity data (*Spence et al.* 2007, *Yuan et al.* 1996, *Helgerud* 2001). In the rock-physics based models (*Carcione and Tinivella* 2000, *Ecker et al.* 1998, *Helgerud* 2001), hydrates can either occupy the pore spaces without appreciable grain contacts, or can act as solid sediment grains altering the properties of the mineral phase, or they can act as a cement between the sediment grains to increase the stiffness of the matrix. Estimates of hydrate concentration using the above assumptions can be very different from each other.

In the present study, hydrate concentration was estimated by using the simple effective porosity-reduction model (*Hyndman et al.* 1993). Replacement of pore fluid by hydrate results in the reduction of the effective sediment porosity and increase in the bulk sediment velocity since hydrate has similar velocity (about 3.8 km/s) as that of rock matrix. The amount of velocity increase (or porosity decrease) due to hydrate formation relative to a no-hydrate reference velocity can be translated to hydrate concentration. Several reference velocity-depth profiles exist for this area (*Yuan et al.* 1996, *Chen* 2006). *Chen* (2006) computed reference velocity profiles for this region from normal move out (NMO) analysis of multichannel seismic data, the time-average equation of *Lee et al.* (1993) and

rock-physics modelling of *Helgerud* (2001) and found that the velocity-depth profile from the multichannel velocity analysis was the most reliable. Therefore, the same reference velocity-depth profile was used to estimate the hydrate concentration. The sediment porosity values for both the reference and the hydrate-containing medium were calculated from the seismic velocity using the following relationship:

$$\Phi = -1.180 + \frac{8.607}{V} - \frac{17.89}{V^2} + \frac{13.94}{V^3} \tag{6.3}$$

where Φ is the porosity and velocity V is measured in km/s. The hydrate concentration was then estimated using the empirical relation

$$S_h = \frac{\Phi_{ref} - \Phi_{hyd}}{\Phi_{ref}} \tag{6.4}$$

where Φ_{ref} is the porosity of the reference medium and Φ_{hyd} is the porosity of the medium containing hydrate. An average hydrate concentration of about 15% was estimated from the velocity model, which matches well with the estimation from sonic data as calculated by *Chen* (2006) (22% in the interval of 150-225 m below seafloor) (Fig. 6.13). However, the hydrate concentration estimate is highly dependent on the reference velocity profile. *Riedel et al.* (2005b) used a different reference velocity profile and found that the hydrate concentration is much lower ($< 10\%$) over the 100 m thick interval above the BSR. Similarly, other estimates based on electrical resistivity and chlorinity data provide different estimates (*Hyndman et al.* 1999, 2001). *Hyndman et al.* (1999) by using core electrical resistivity and porosity data estimated hydrate concentrations between 25% and 35% of the pore volume over a 100-m thick interval just above the BSR, whereas their analysis of

acoustic velocity data from sonic log, MCS interval velocity, and VSP provided a relatively lower concentration of about 20%.

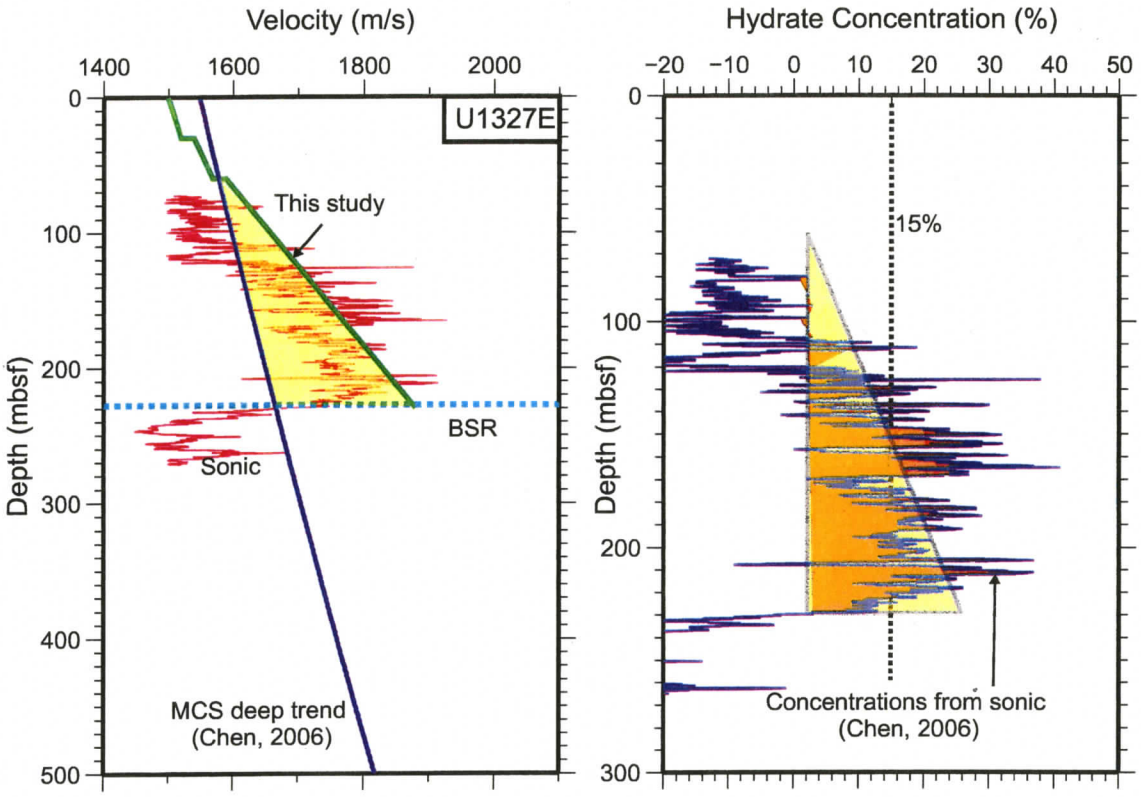

Figure 6.13: Hydrate concentration estimated from increase in seismic P-wave velocity above the background trend.

The P-wave velocity model provides a well-constrained estimate of hydrate concentration for a 5-km long profile centred near the IODP Site U1327 drillholes. Velocities increase uniformly with depth over the entire region. No evidence was found for layers with high hydrate concentrations at depths between 120-138 mbsf as detected in Hole U1327A (Fig. 6.14). Thus the occurrence detected in this hole must be very localized as it was not detected in the nearby Hole U1327E (at 70 m distance) or in the P-wave OBS models.

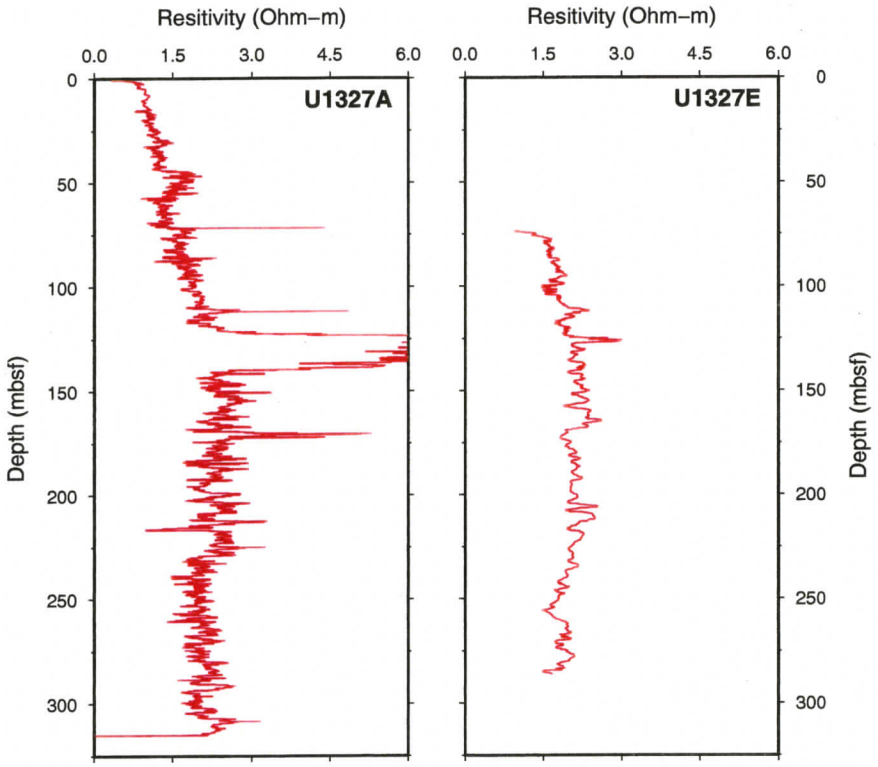

Figure 6.14: Resistivity logs from drillhole U1327A and U1327E.

6.4.2 Hydrate distribution in pores from S-wave velocities

While the presence of hydrate in the sediment pore space increases the P-wave velocity, its effect on S-wave velocity can be very different depending upon the type of hydrate distribution. S-waves are insensitive to hydrate occurrence when it is present in the sediment pore volume without grain contact. However, for the hydrate in-frame model, an increase in S-wave velocity occurs due to an increase in sediment stiffness. Thus the rock-physics models can be used to estimate hydrate concentration from S-wave data. In the present model, since both the P- and S-wave velocity models show an increase in velocities for the hydrate bearing layer, it is most likely that hydrates cement the sediment grains. However, the reference model for S-wave velocity in sediments without hydrate

is uncertain. In the absence of the reference velocity model, the global average model of *Hamilton* (1979) can be used, although it may vary with sediment type.

6.5 Summary

An average P-wave velocity model for the sediments containing gas hydrates was estimated from the ray-trace traveltime inversion. The P-wave velocity values are consistent with all the OBS stations and are well constrained above the BSR within 2-km offset of the OBS positions. The P-wave velocity model provides a higher resolution structure than previously obtained (*Hobro* 1999, *Hobro et al.* 2005). Using S-wave data from the OBS horizontal components, an estimate was made for the S-wave velocity structure and layers below the BSR were imaged. Overall, the P- and S-wave results are in good agreement with the sonic log data from the ODP Site 889 and IODP Site U1327. Agreement of model velocity with the drillhole data at different sites suggests that the velocity values can be extended from the drill sites on a kilometre scale. The depth of the BSR is very well constrained at 230 m depth (within an uncertainty of 5 m). Therefore, the mismatch between P-wave velocity-depth profile at U1327 and the Vertical Seismic Profile (VSP) data is most likely due to a problem with the VSP dataset.

The S-wave velocity values from sonic log data are about 75 m/s higher than the global estimates of V_s in poorly consolidated sediments as determined by *Hamilton* (1979). The S-wave velocities from PS ray-trace modelling are about 100 m/s higher than *Hamilton* (1979)'s model although this is comparable to estimated errors.

An average hydrate concentration of 15% was estimated from the P-wave velocity model. Like V_p, V_s increases with depth and also appears to increase with hydrate concen-

tration. The increase in V_s with hydrate concentration implies that the hydrate act as a cement between sediment grains to increase the rigidity of the rock matrix. But unlike V_p, the decrease in V_s is not significant in the presence of free gas below the BSR as S-wave is insensitive to the presence of gas.

Chapter 7

Summary and Conclusions

The primary focus of this dissertation was to image the shallow velocity structure of two regions near Vancouver Island. Non-linear tomographic inversion of seismic traveltimes yielded high-resolution velocity models for the shallow structures beneath the southern Strait of Georgia (Fig. 5.11) and for the hydrate-containing sediments in the continental slope offshore Vancouver Island (Fig. 6.7). The Strait of Georgia velocity model provides a better understanding of the local geology and earthquake hazard beneath this region. The velocity model offshore Vancouver Island provides the means to estimate gas hydrate concentration in the continental slope sediments.

In the southern Georgia Basin east of Vancouver Island, first arrival traveltimes from two wide-angle seismic experiments were utilized to obtain a 3D high-resolution velocity model down to about 7 km depth. The model agrees well with the previous studies from the region, but due to dense ray coverage, provides higher resolution for the shallower part with a lateral resolution of about 5 km down to 3.8 km depth. Interpretation of the final velocity model was aimed at mapping the depth of the Cenozoic sedimentary

basin, mapping the geometry of the shallow crustal faults and correlating the structures with recent seismicity. Assuming that the sedimentary rock velocities are less than 5.5 km/s, the depth of the basin was estimated to lie between 5 and 6 km depth. In the northwestern part of the basin, higher velocities are observed at shallower depths. The basin depth increases to the southeast with the maximum depth near the southeastern end of the basin. There is a sharp increase in basin depth near the location of the 1997 and 1975 earthquakes. The sudden change in depth and its association with seismicity is interpreted to be due to the presence of a fault that is informally named the Gabriola Island fault. The Outer Island fault was clearly imaged in the final velocity model as a 60-km long northwest-trending, southwest-dipping velocity discontinuity at shallow depth. The surface expression of the Outer Island fault as mapped in the swath bathymetry data matches well with the seismically-derived structure. The Lummi Island fault is interpreted from a east-trending velocity discontinuity east of the San Juan Islands at the southeastern end of the strait. The Outer Island fault steepens towards its eastern end as it approaches the Lummi Island fault. The basement ridges on the north, west and south define the outer limit of the southern Georgia Basin. The eastern side of the basin is not clearly imaged due to poor data quality and, hence, the eastern extent of Wrangellia and its boundary with the Coast Belt are not clear. The faults are associated with a rapid change in basin depth, which indicates that fault motion may involve basement. The locations of frequent recent seismicity are associated with rapid changes in seismic velocity.

In the mid-continental slope offshore Vancouver Island, seismic velocity structure was investigated along a 2D profile perpendicular to the continental margin using seismic single channel and ocean bottom seismometer data, and hydrate concentration in the sediment

pore space was estimated. The BSR is very well-defined in this region, as it lies within the seismically transparent accreted sediment sections. Ray-trace traveltime modelling of the P-wave arrivals from single channel and OBS data revealed three layers above the BSR. The upper two layers constitute the recently deposited continental slope sediments and have very low velocities (1.50 to 1.58 km/s). The third layer constitutes more consolidated sediments of the accretionary prism and has higher velocities increasing from 1.62 km/s at the top to 1.88 km/s at the BSR, which occurs at 230 m below seafloor. Ray trace modelling using S-wave data from OBS horizontal components provides information at depths below the BSR, which is otherwise difficult to obtain from P-wave data alone due to strong V_p attenuation. Both the P- and S-wave velocity models are in good agreement with with the sonic data from ODP Site 889 and IODP Site 1327. The increase in P-wave velocity in the layer above the BSR is interpreted to estimate the hydrate concentration in the pore space. Using a simple velocity-porosity relation, an average hydrate concentration of about 15% was estimated from the model velocity over a depth range of 100 m.

A new migration method, called mirror imaging, was applied to the OBS dataset to image the sediment structure along the 2D profile. The method uses the first order multiples through the water column and provides a very good image of the subsurface structure comparable to the image obtained from surface streamer data. The method shows considerable improvement in lateral coverage over the conventional migration methods, which use the upgoing wave fields or the primary reflections arriving at the OBS from below. The major advantage of mirror imaging is to provide detailed reflection structures including the shallow layers below the seafloor at large offsets from an OBS survey, particularly when the OBS coverage is sparse. However, the migration process needs an input velocity

model, which is a problem if prior velocity is not available. This difficulty can be partly overcome by obtaining velocity from normal move-out corrected data.

7.1 Suggestions for future work

The seismic tomographic studies of the Georgia Basin and the continental slope area provide high resolution velocity models for the shallow structures. However, there are several limitations on both the studies that could be overcome in future. The Georgia Basin model has limited information in the eastern edge of the strait and provides very little knowledge about the boundray between the Insular Belt and the Coast Belt. The primary reason for this is the sparse receiver distribution on the Fraser River delta area and very low signal-to-noise ratio of the wide-angle data. Also, the shot geometry was more focused on the Outer Island fault region. Thus a bigger airgun source and a denser source-receiver coverage on the eastern edge of the strait may provide additional information. Secondly, the tomographic inversion uses only the first arrival traveltimes and provides only a smooth velocity model for the structures. Combined study with other datasets such as multichannel seismic data or drill hole data (if available) may provide even a higher resolution structure.

The seismic experiment on the continental slope off Vancouver Island was initially planned to provide preliminary information to the IODP Expedition 311. The mirror imaging study of the OBS dataset proves that there is much more information in the OBS data than was previously thought. In particular, the multiples provide information far beyond the deployment position of the OBSs and can be exploited to investigate structures when information from other sources is not available. Mirror imaging works

well with sparse receiver coverage. Thus an OBS spacing of about 500 m and a longer shotline will provide wider coverage than obtained from the current study. In the absence of prior velocity information, combined velocity analysis of primary and multiples will provide velocity and structural information and can be used for the input model in OBS migration. Therefore, a longer trace length covering the second order multiples (6-7 s trace length for this area) would be better.

The airgun source used for this study was very small (45/45 cu. in. GI gun) to produce detectable refractions. Although the reflections from the OBS data constrain the velocity gradient to some degree, the refraction data will provide further constraints. Furthermore, structures below the BSR, which are absent in the P-wave reflection data, could be easily interpreted from refracted arrivals if they could be observed. Therefore a bigger airgun source would be helpful in future experiments to generate deeper refracted arrivals.

References

Aki, K., A. Christoffersson, and E. S. Huesbye (1977), Determination of the three-dimensional structure of the lithosphere, *J. Geophys. Res.*, *82*(2), 277–296.

Backus, M. L., P. E. Murray, B. A. Hardage, and R. J. Graebner (2006), High-resolution multicomponent seismic imaging of deepwater gas-hydrate systems, *The Leading Edge*, pp. 578–596.

Barr, F. J., and J. I. Sanders (1989), Attenuation of water-column multiples using pressure and velocity detectors in a water-bottom cable, in *59th Ann. Internat. Mtg.*, Expanded Abstracts, pp. 653–656, Soc. Expl. Geophys.

Barrie, J. V., and P. R. Hill (2004), Holocene faulting on a tectonic margin: Georgia basin, British Columbia, Canada, *GeoMarine Letters*, *24*, 86–96.

Bishop, T. N., K. P. Bube, R. T. Cutler, R. T. Langan, P. L. Love, J. R. Resnick, R. T. Shuey, D. A. Spindler, and H. W. Wyld (1985), Tomographic determination of velocity and depth in laterally varying media, *Geophysics*, *50*, 903–923.

Brandon, M. T., and A. R. Calderwood (1990), High-pressure metamorphism and uplift of the Olympic subduction complex, *Geology*, *18*, 1252–1255.

Brocher, T. M. (2005), Compressional and shear-wave velocity versus depth in the San Francisco Bay area, California: rules for USGS Bay area velocity model 05.0.0, *U.S. Geol. Surv. Open-File Report*, pp. 05–1317, 58 p, http://pubs.usgs.gov/of/2005/1317/.

Brocher, T. M., T. Parsons, R. J. Blakely, N. I. Christensen, M. A. Fisher, R. E. Wells, and the SHIPS Working Group (2001), Upper crustal structure in Puget Lowland, Washington: Results from the 1998 Seismic Hazards Investigation in Puget Sound, *J. Geophys. Res.*, *106, B7*, 13,541–13,564.

Brocher, T. M., T. L. Pratt, G. D. Spence, M. Riedel, and R. D. Hyndman (2003), Wide-angle seismic recordings from the 2002 Georgia Basin Geohazards Initiative, northwestern Washington and British Columbia, *U.S. Geol. Surv. Open-File Report*, pp. 03–160, 34 p, http://geopubs.wr.usgs.gov/open-file/of03-160/.

Brocher, T. M., et al. (1999), Wide-angle seismic recordings from the 1998 seismic hazards investigation of Puget Sound (SHIPS), western Washington and British Columbia, *U.S. Geol. Surv. Open-File Report*, pp. 99–314, 110 p, http://geopubs.wr.usgs.gov/open-file/of99-314/.

Caldwell, J. (1999), Marine multicomponent seismology, *The Leading Edge*, pp. 1274–1282.

Calvert, A. J. (1996), Seismic reection constraints on imbrication and underplating of the northern Cascadia convergent margin, *Can. J. Earth Sci.*, *33*, 1294–1307.

Calvert, A. J., and R. M. Clowes (1990), Deep, high amplitude reections from a shear zone above the subducting Juan de Fuca plate, *Geology*, *18*, 1091–1094.

Carcione, J. M., and U. Tinivella (2000), Bottom-simulating reflectors: Seismic velocities and AVO effects, *Geophysics*, *65*(1), 54–67.

Cassidy, J. F., G. C. Rogers, and F. Waldhauser (2000), Characterization of active faulting beneath the Strait of Georgia, British Columbia, *Bull. Seism. Soc. Am.*, *90*(5), 1188–1199.

Castagna, J. P., M. L. Batzle, and R. L. Eastwood (1985), Relationships between compressional-wave and shear-wave velocities in clastic silicate rocks, *Geophysics*, *50*(4), 571–581.

Cervený (1987), Ray tracing algoritms in three-dimensional laterally varying layered structures, in *Seismic Tomography: with applications in global seismology and exploration geophysics*, edited by G. Nolet, pp. 99–133, D. Reidel Publishing Co., Dordrecht, Holland.

Chapman, N. R., J. F. Gettrust, R. Walia, D. Hannay, G. D. Spence, W. T. Wood, and R. D. Hyndman (2002), High-resolution, deep-towed, multichannel seismic survey of deep-sea gas hydrates off western Canada, *Geophysics*, *67*(4), 1038–1047.

Chen, M. (2006), Northern Cascadia marine gas hydrate: constraints from resistivity, velocity, and AVO, Master's thesis, University of Victoria.

Clague, J. J., J. L. Luternauer, and R. J. Hebda (1983), Sedimentary environments and post-glacial history of the Fraser River Delta and lower Fraser valley, *Can. J. Earth Sci.*, *20*, 1314–1426.

Clowes, R. M., M. T. Brandon, A. G. Green, C. J. Yorath, A. S. Brown, E. R. Kanaswich, and C. Spencer (1987), LITHOPROBE-southern Vancouver Island: Cenozoic subduction complex imaged by deep seismic reflection, *Can. J. Earth Sci.*, *24*, 247–255.

Creager, K. C., , and L. M. Dorman (1982), Location of instruments on the sea floor by joint adjustment of instrument and ship positions, *J. Geophys. Res.*, *87*, 8379–8388.

Dash, R. K., G. D. Spence, M. Riedel, R. D. Hyndman, and T. M. Brocher (2007), Upper-crustal structure beneath the Strait of Georgia, Southwest British Columbia, *Geophy. J. Int.*, *170*(2), 800–812, doi:10.1111/j.1365-246X.2007.03455.x.

Davie, M., and B. A. Buffet (2001), A numerical model for the formation of gas hydrates below the seafloor, *J. Geophys. Res.*, *106*(B1), 497–514.

Davis, E. E., and R. D. Hyndman (1989), Accretion and recent deformation of sediments along the northern Cascadia subduction zone, *101*, 1465–1480.

Davis, E. E., R. D. Hyndman, and H. Villinger (1990), Rates of fluid expulsion across the northern Cascadia accretionary prism: constraints from new heat flow and multichannel seismic reflection data, *J. Geophys. Res.*, *95*, 8869–8889.

DeMets, C., R. G. Gordon, D. F. Argus, and S. Stein (1990), Current plate motions, *Geophy. J. Int.*, *101*, 425–478.

Dickens, G. (2001), On the fate of past gas: What happens to methane released from a bacterially mediated gas hydrate capacitor ?, *Geochem. Geophys. Geosyst.*, *2*(1), doi:10.1029/2000GC000131.

Ecker, C., J. Dvorkin, and A. Nur (1998), Sediments with gas hydrates: Internal structure from seismic AVO, *Geophysics*, *63*(5), 1659–1669.

Edwards, R. N. (1997), On the resource evaluation of marine gas hydrate deposits using sea-floor transient electric dipole-dipole methods, *Geophysics*, *62*(1), 63–74.

Engebreston, D. C., K. P. Kelly, H. J. Cashman, and M. A. Richards (1992), 180 million years of subduction, *GSA Today*, *2*(100), 93–95.

England, T. D. J., and R. M. Bustin (1998), Architecture of the Georgia Basin, southwestern British Columbia, *Bull. Can. Petro. Geol.*, *46*, 288–320.

England, T. D. J., and T. J. Calon (1991), The Cowichan fold and thrust system, Vancouver Island, southwestern British Columbia, *Geol. Soc. Am. Bull.*, *103*, 336–362.

Fink, C. R., and G. D. Spence (1999), Hydrate distribution off Vancouver Island from multi-frequency single channel seismic reflection data, *J. Geophys. Res.*, *104*(B2), 2909–2922, doi:10.1029/98JB02641.

Godfrey, R. J., P. Kristiansen, B. Armstrong, M. Cooper, and E. Thorogood (1998), Imaging the foinaven ghost, in *68th Ann. Internat. Mtg.*, Expanded Abstracts, pp. 1333–1335, Soc. Expl. Geophys.

Graindorge, D., G. Spence, P. Charvis, J. Y. Collot, R. Hyndman, and A. M. Trehu (2003), Crustal structure beneath Strait of Juan de Fuca and southern Vancouver Island from seismic and gravity analyses, *J. Geophys. Res.*, *108*(B10), 2484, doi:10.1029/2002JB001823.

Grand, S. P., R. D. van der Hilst, and S. Widiyantoro (1997), Global seismic tomography: A snapshot of convection in the earth, *GSA Today*, *7*, 1–7.

Grion, S., R. Exley, M. Manin, X. Miao, A. Pica, Y. Wang, P. Granger, and S. Ronen (2007), Mirror imaging of OBS data, *First Break*, *25*, 37–42.

Hamilton, E. L. (1979), V_p/V_s and Poisson's ratios in marine sediments and rocks, *J. Acoust. Soc. Am.*, *66*(4).

Helgerud, M. B. (2001), Wave speeds in gas hydrate and sediments containing gas hydrate: a laboratory and modeling study, Ph.D. thesis, Stanford University.

Hobro, J. W. D. (1999), Three-dimensional tomographic inversion of combined reflection and refraction seismic travel-time data, Ph.D. thesis, University of Cambridge.

Hobro, J. W. D., T. A. Minshull, S. C. Singh, and S. Chand (2005), A three-dimensional seismic tomographic study of the gas hydrate stability zone, offshore Vancouver Island, *J. Geophys. Res.*, *110*(B09102), doi:10.1029/2004JB003477.

Hoffe, B. H., and P. W. Cary (2000), Application of OBC recording, *The Leading Edge*, *19*, 382–391.

Hole, J. A. (1992), Nonlinear high-resolution three-dimensional seismic travel time tomography, *J. Geophys. Res.*, *97*, 6553–6562.

Hole, J. A., and B. C. Zelt (1995), 3-D finite-difference reflection traveltimes, *Geophy. J. Int.*, *121*, 427–434.

Humphreys, E., and R. W. Clayton (1988), Adaption of back projection tomography to seismic travel time problems, *J. Geophys. Res.*, *93*, 1073–1085.

Hyndman, R. D. (1988), Dipping reectors, electrically conductive zones and free water beneath a subduction zone, *J. Geophys. Res.*, *93*, 13,391–13,405.

Hyndman, R. D., and E. E. Davis (1992), A Mechanism for the Formation of Methane Hydrate and Seafloor Bottom-Simulating Reflectors by Vertical Fluid Expulsion, *J. Geophys. Res.*, *97*(B5), 7025–7041.

Hyndman, R. D., and G. D. Spence (1992), A seismic study of methane hydrate marine bottom simulating reflectors, *J. Geophys. Res.*, *97*(B5), 6683–6698.

Hyndman, R. D., C. J. Yorath, R. M. Clowes, and E. E. Davis (1990), The northern Cascadia Subduction Zone At Vancouver Island: Seismic Structure and Tectonic History, *Can. J. Earth Sci.*, *27*(3), 313–329.

Hyndman, R. D., G. F. Moore, , and K. Moran (1993), Velocity, porosity, and pore-fluid loss from the Nankai subduction zone accretionary prism, in *Proceedings of the Ocean Drilling Program, Scientific Results*, pp. 211–220.

Hyndman, R. D., K. Moran, and T. Yuan (1999), The concentration of deep sea gas hydrates from downhole resistivity logs and laboratory data, *Earth Planet. Sci. Lett.*, *172*(1-2), 167–177, doi:10.1016/S0012-821X(99)00192-2.

Hyndman, R. D., G. D. Spence, R. Chapman, M. Riedel, and R. N. Edwards (2001), Geophysical studies of marine gas hydrate in northern Cascadia, in *Natural gas hydrates: occurrence, distribution, and detection*, *Geophysical Monograph*, vol. 124, edited by C. K. Paull and W. P. Dillon, pp. 273–295, American Geophysical Union.

Jiang, Z., J. Yu, G. T. Schuster, and B. E. Hornby (2005), Migration of multiples, *The Leading Edge*, *24*, 315–318.

Johnson, S. Y. (1984), Stratigraphy, age and paleogeography of the eocene chukanut formation, northwest washington, *Can. J. Earth Sci.*, *21*, 92–106.

Johnson, S. Y. (1985), Eocene strike-slip faulting and nonmarine basin formation in Washington, in *Strike-Slip Deformation, Basin Formation and Sedimentation*, vol. 37, edited by K. T. Biddle and N. Christie-Blick, pp. 283–302, SEPM, Spec. Publ.

Journeay, J. M., and R. M. Friedman (1993), The Coast Belt thrust system: Evidence of Late Cretaceous shortening in southwest British Columbia, *Tectonics*, *12*, 756–775.

Katzman, R., W. S. Holbrook, and C. K. Paull (1994), Combined vertical-incidence and wide-angle seismic study of a gas hydrate zone, Blake Ridge, *J. Geophys. Res.*, *99*(B9), 17,975–17,996, doi:10.1029/94JB00662.

Kennett, J. P., K. G. Cannariato, I. L. Hendy, and R. J. Behl (2000), Carbon isotopic evidence for methane hydrate instability during quarternary interstadials, *Science*, *288*, 128–133.

Kvenvolden, K. A. (1994), Natural gas hydrate occurrence and issue, in *International Conference on Natural Gas Hydrates*, vol. 715, edited by E. D. Sloan, J. Happel, and M. A. Hnatow, pp. 232–246, Ann. N. Y. Acad. Sci.

Lee, M. W., D. R. Hutchinson, W. P. Dillon, J. J. Miller, W. F. Agena, and B. A. Swift (1993), Method of estimating the amount of in situ gas hydrates in deep marine sediments, *Marine and Petroleum Geology, 10*, 496–506.

Lee, W. H. K., and V. Pereyra (1993), Mathematical introduction to seismic tomography, in *Seismic Tomography*, edited by H. M. Iyer and K. Hirahara, pp. 9–22, Chapman and Hall, London.

Li, J., and S. Ronen (2005), Estimating and correcting of tilted multicomponent receivers, in 67^{th} *Conference & Exhibition*, Madrid, Spain.

Li, J., S. Jin, and S. Ronen (2004), Data-driven tilt angle estimation of multi-component receivers, in 74^{th} *Ann. Internat. Mtg.*, Expanded Abstracts, Soc. Expl. Geophys, MC 3.5.

Liu, X., and P. B. Flemings (2007), Dynamic multiphase flow model of hydrate formation in marine sediments, *J. Geophys. Res., 112*(B03101), doi:10.1029/2005JB004227.

Lopez, C. D., G. D. Spence, and R. D. Hyndman (2006), Seismic velocity structure associated with gas hydrate at the frontal ridge of the northern Cascadia margin, *AGU Fall Meeting.*

Lowe, C., S. A. Dehler, and B. C. Zelt (2003), Basin architecture and density structure beneath the Strait of Georgia, British Columbia, *Can. J. Earth Sci., 40*, 965–981.

MacKay, M. E., R. D. Jarrard, G. K. Westbrook, and R. D. Hyndman (1994), Origin of bottom-simulating reflectors; geophysical evidence from the Cascadia accretionary prism, *Geology, 22*(5), 459–462.

Mazzotti, S., H. Dragert, R. D. Hyndman, M. M. Miller, and J. A. Henton (2002), GPS deformation in a region of high crustal seismicity: N. Cascadia forearc, *198*, 41–48.

Mazzotti, S., H. Dragert, J. Henton, M. Schmidt, R. Hyndman, T. James, Y. Lu, and M. Craymer (2003), Current tectonics of northen Cascadia from a decade of GPS mesurements, *J. Geophys. Res., 108*, B12, doi:10.1029/2003JB002653.

Monger, J. W. H. (1990), Georgia Basin: Regional setting and adjacent Coast Mountains geology, British Columbia, *Geol. Survey of Canada, Current Research, 90-1F*, 95–107.

Monger, J. W. H., R. A. Price, and D. J. Templeman-Kluit (1982), Tectonic accretion and the origin of the two major metamorphic and plutonic welts in the Canadian Cordillera, *Geology, 10*, 7075.

Mosher, D. C., and T. S. Hamilton (1998), Morphology, structure and stratigraphy of the offshore Fraser delta and adjacent Straitof Georgia, in *Geology and Natural Hazards of the Fraser River Delta, British Columbia*, vol. 525, edited by J. J. Clague, J. L. Luternauer, and D. C. Mosher, pp. 147–160, Geol. Surv. Can. Bull.

Mosher, D. C., J. F. Cassidy, C. Lowe, Y. Mi, R. D. Hyndman, G. C. Rogers, , and M. Fisher (2000), Neotectonics in the Strait of Georgia: First tentative correlation of seismicity with shallow geological structure in southwestern British Columbia, *Geol. Survey of Canada, Current Research, 2000-A22*, 1–9.

Mulder, T. L. (1995), Small earthquakes in southwestern british columbia (1975-1991), Master's thesis, University of Victoria.

Mulder, T. L., and G. C. Rogers (1998), Poisson's ratio in southwestern British Columbia, in *Programs and abstracts*, p. A131, Can. Geophys. Un., Quebec City, Canada.

Mustard, P. S. (1994), The upper Cretaceous Nanaimo Group, Georgia Basin, in *Geology and geological hazards of the Vancouver region, southwestern British Columbia*, vol. 481, edited by J. W. H. Monger, pp. 27–95, Geol. Surv. Can. Bull.

Mustard, P. S., and G. E. Rouse (1994), Stratigraphy and evolution of Tertiary Georgia Basin and subjacent Upper Cretaceous sedimentary rocks, southwestern British Columbia and northwestern Washington State, in *Geology and geological hazards of the Vancouver region, southwestern British Columbia*, vol. 481, edited by J. W. H. Monger, pp. 97–140, Geol. Surv. Can. Bull.

Novosel, I. (2002), Physical properties of gas hydrate related sediments, offshore Vancouver Island, Master's thesis, University of Victoria.

Paige, C. C., and M. A. Saunders (1982), LSQR: An algorithm for sparse linear equations and sparse least squares, *Assoc. Comput. Mach. Trans. Math. Software, 8*, 43–71.

Paull, C. K., and W. Ussler (1997), Are low salinity anomalies below BSRs a consequence of interstitial gas bubble barrier ?, *EOS, 78*, 339.

Phillips, W. S., and M. C. Fehler (1991), Traveltime tomography: A comparison of popular methods, *Geophysics, 56*(10).

Pica, A., M. Manin, P. Y. Granger, D. Marin, E. Suaudeau, B. David, G. Poulain, and P. Herrmann (2006), 3D SRME on OBS data using waveform multiple modeling, in *76th Ann. Internat. Mtg.*, Expanded Abstracts, pp. 2659–2663, Soc. Expl. Geophys.

Podvin, P., and I. Lecomte (1997), Finite difference computation of traveltimes in very contrasted velocity models: a massively parallel approach and its associated tools, *Geophy. J. Int.*, *105*, 271–284.

Pratt, T. L., S. Y. Johnson, C. J. Potter, W. J. Stephenson, , and C. A. Finn (1997), Seismic reflection images beneath Puget Sound, western Washington State: The Puget Lowland thrust sheet hypothesis, *J. Geophys. Res.*, *102*, 27,469–27,489.

Qin, F., Y. Luo, K. B. Olsen, W. Cai, and G. T. Schuster (1992), Finite-difference solution of the eikonal equation along expanding wavefronts, *Geophysics*, *57*, 478–487.

Ramachandran, K. (2001), Velocity structure of south west British Columbia and north west Washington, from 3-D non-linear seismic tomography, Ph.D. thesis, University of Victoria.

Ramachandran, K., S. E. Dosso, C. A. Zelt, G. D. Spence, R. D. Hyndman, and T. M. Brocher (2004), Upper crustal structure of southwestern British Columbia from the 1998 Seismic Hazards Investigation in Puget Sound, *J. Geophys. Res.*, *109*, B09,303, doi:10.1029/2003JB002826.

Riddihough, R. P. (1982), One hundred million years of plate tectonics in western Canada, *Geosci. Can.*, *9*, 28–34.

Riddihough, R. P. (1984), Recent movements of the Juan de Fuca Plate system, *J. Geophys. Res.*, *89*, 6980–6994.

Riddihough, R. P., and R. D. Hyndman (1991), Modern plate tectonic regime of the continental margin of western Canada, in *Geology of the Cordilleran orogen in Canada*, vol. 4, edited by H. Gabrielse and C. J. Yorath, pp. 435–455, Geological Survey of Canada.

Riedel, M. (2002), Georgia Basin Geohazards Initiative mapping of near surface active faults : A report on Cruise PGC2002 on C.G.G. J.P. Tully, May 13-27, 2002, *Tech. rep.*, Geological Survey of Canada.

Riedel, M., G. D. Spence, N. R. Chapman, and R. D. Hyndman (2002), Seismic investigations of a vent field associated with gas hydrates, offshore Vancouver Island, *J. Geophys. Res.*, *107*(B9), 2200, doi:10.1029/2001JB000269.

Riedel, M., T. S. Collett, and Expedition 311 Scientists (2005a), Cascadia margin gas hydrates, *IODP Prel. Rept. 311.*

Riedel, M., T. S. Collett, and R. D. Hyndman (2005b), Gas hydrate concentration estimates from chlorinity, electrical resistivity, and seismic velocity, *Geol. Surv. Can. Open-File Rep.*, 4934.

Riedel, M., T. S. Collett, M. J. Malone, and the Expedition 311 Scientists (2006a), Proceedings of the Integrated Ocean Drilling Program, Volume 311, *Tech. rep.*, Integrated Ocean Drilling Program Management International Inc., Washington, DC, doi:10.2204/iodp.proc.311.2006.

Riedel, M., I. Novosel, G. D. Spence, R. D. Hyndman, N. R. Chapman, R. C. Solem, and T. Lewis (2006b), Geophysical and geochemical signatures associated with gas hydraterelated venting in the northern Cascadia margin, *Geol. Soc. Am. Bull.*, *118*(1-2), 23–38.

Rogers, G. C. (1988), An assessment of the megathrust earthquake potential of the Cascadia subduction zone, *Can. J. Earth Sci.*, *25*, 844–852.

Rogers, G. C. (1994), Earthquakes in the Vancouver area, in *Geology and geological hazards of the Vancouver region, southwestern British Columbia*, vol. 481, edited by J. W. H. Monger, pp. 221–229, Geol. Surv. Can. Bull.

Rogers, G. C. (1998), Earthquakes and earthquake hazard in the Vancouver area, in *Recent Geological, Geophysical, Geotechnical, and Geochemical Research, Fraser River Delta, British Columbia*, vol. 525, edited by J. Clague, J. Luternauer, and D. Mosher, pp. 19–25, Geol. Surv. Can. Bull.

Ronen, S., L. Comeaux, and J. G. Miao (2005), Imaging downgoing waves from ocean bottom stations, in 75^{th} *Ann. Internat. Mtg.*, Expanded Abstracts, Soc. Expl. Geophys.

Scales, J. A., P. Docherty, and A. Gersztenkorn (1990), Regularization of nonlinear inverse problems: imaging the near surface weathering layer, *Inverse Problems*, *6*, 115–131.

Schalkwijk, K. M. (2001), Decomposition of multicomponent ocean-bottom data into P- and S-waves, Ph.D. thesis, Delft University of Technology.

Schalkwijk, K. M., D. J. Verschuur, and C. P. A. Wapenaar (2001), A decomposition and multiple removal strategy for multicomponent obc data, in 71^{st} *Ann. Internat. Mtg.*, Expanded Abstracts, pp. 813–816, Soc. Expl. Geophys.

Schneider, W. A., P. J. Farrell, , and R. E. Brannian (1964), Collection and analysis of Pacific ocean-bottom seismic data, *Geophysics*, *29*, 745–771.

Shaw, P. R., and J. A. Orcutt (1985), Waveform inversion of seismic refraction data and application to young Pacific crust, *Geophys. J. R. Astr. Soc.*, *82*, 375–414.

Shiobara, H., A. Nakanishi, H. Shimamura, R. Mjelde, T. Kanazawa, and E. W. Berg (1997), Precise positioning of ocean bottom seismometer by using acoustic transponder and ctd, *Marine Geophysical Researches*, *19*, 199–209.

Solem, R. C., G. D. Spence, D. Vukajlovich, M. R. R. D. Hyndman and, I. Novosel, and M. Kastner (2002), Methane advection and gas hydrate formation within an active vent field offshore Vancouver Island, in *Fourth Int. Conf. Gas Hydrates*, p. 19023.

Spence, G., E. Willoughby, and T. He (2005), Single-channel seismic, compliance and electromagnetic measurements offshore vancouver island, ceor report: 2005-3, *Tech. rep.*, CEOR, University of Victoria.

Spence, G. D., T. A. Minshull, and C. Fink (1995), Seismic studies of methane gas hydrate, offshore Vancouver Island, in *Proc. ODP, Sci. Results, Ocean Drilling Program*, vol. 146, College Station, TX.

Spence, G. D., R. R. Haacke, and R. D. Hyndman (2007), Seismic indicators of natural gas hydrate and underlying free gas, *(submitted to SEG hydrate volume)*.

ten Brink, U. S., P. C. Molzer, M. A. Fisher, R. J. Blakely, R. C. Bucknam, T. P. R. S. Crosson, and K. C. Creager (2002), Subsurface geometry and evolution of the Seattle fault zone and the Seattle Basin, Washington, *Bull. Seism. Soc. Am.*, *92*, 1737–1753.

Thurber, C. H. (1983), Earthquake locations and three-dimensional crustal structure in the Coyote Lake area, central California, *J. Geophys. Res.*, *88*, 8226–8236.

Tolstoy, M., A. J. Harding, and J. A. Orcutt (1993), Crustal thickness on the MidAtlantic Ridge: Bullseye gravity anomalies and focused accretion, *Science*, *262*, 726–729.

Toomey, D. R., S. C. Solomon, and G. M. Purdy (1994), Tomographic imaging of the shallow crustal structure of the East Pacific Rise at $9^0$30' N, *J. Geophys. Res.*, *99*(B12), 24,135–24,158.

Um, J., and C. H. Thurber (1987), A fast algorithm for two-point seismic ray tracing, *Bull. Seism. Soc. Am.*, *77*, 972–986.

van der Hilst, R. D., S. Widiyantoro, and E. R. Engdahl (1997), Evidence for deep mantle circulation from global tomography, *Nature*, *386*, 578–584.

van Trier, J., and W. W. Symes (1991), Upwind finite-difference calculation of traveltimes, *Geophysics*, *56*(6), 812–821.

Vidale, J. E. (1988), Finite-difference calculation of travel times, *Bull. Seism. Soc. Am.*, *78*, 2062–2076.

Vidale, J. E. (1990), Finite-difference calculation of travel times in three dimensions, *Geophysics*, *55*, 521–526.

Waite, W. F., M. B. Helgerud, A. Nur, J. Pinkston, L. A. Stern, S. H. Kirby, and W. B. Durham (2000), First laboratory measurements of compressional and shear wave speeds through pure methane hydrate at in situ conditions, in *Gas Hydrates: Challenges for the Future*, vol. 912, edited by G. D. Holder and P. R. Bishnoi, pp. 1003–1010, Ann. N. Y. Acad. Sci.

Wang, K., T. Mulder, G. C. Rogers, and R. D. Hyndman (1995), Case for very low coupling stress on the Cascadia subduction fault, *J. Geophys. Res.*, *100*, 12,907–12,918.

Wells, R. E., C. S. Weaver, , and R. J. Blakely (1998), Forearc migration in Cascadia and its neotectonic significance, *Geology*, *26*, 759–762.

West, M. E. (2001), The deep structure of Axial Volcano, Ph.D. thesis, Columbia University.

Westbrook, G. K., B. arson, R. J. Musgrave, and S. Scientists (1994), *Proc. Ocean Drill. Program, Initial Rep.*, *146*, 611p.

White, D. J. (1989), Two-dimensional seismic refraction tomography, *Geophy. J. Int.*, *97*, 223–245.

Williamson, P. R. (1990), Tomographic inversion in reflection seismology, *Geophy. J. Int.*, *100*(2), 255–274.

Willoughby, E. C., and R. N. Edwards (2000), Shear velocities in Cascadia from seafloor compliance measurements, *Geophys. Res. Lett.*, *27*(7), 1021–1024, 10.1029/1999GL010481.

Wilson, D. S. (1993), Confidence intervals for motion and deformation of the Juan de Fuca plate, *J. Geophys. Res.*, *98*, 16,053–16,071.

Xu, W., and C. Ruppel (1999), Predicting the occurrence, distribution, and evolution of methane gas hydrate in porous marine sediments, *J. Geophys. Res.*, *104*, 5081–5095.

Yuan, J., and R. N. Edwards (2000), The assessment of marine gas hydrates through electrical remote sounding: Hydrate without a BSR?, *Geophys. Res. Lett.*, *27*(16), 2397–2400, 10.1029/2000GL011585.

Yuan, T., R. D. Hyndman, G. D. Spence, and B. Desmons (1996), Seismic velocity increase and deep-sea gas hydrate concentration above a bottom-simulating reflector on the northern Cascadia continental slope, *J. Geophys. Res.*, *101*(B6), 13,655–13,672.

Yuan, T., G. D. Spence, R. D. Hyndman, T. A. Minshull, and S. C. Singh (1999), Seismic velocity studies of a gas hydrate bottom-simulating reflector on the northern Cascadia continental margin: Amplitude modeling and full waveform inversion, *J. Geophys. Res.*, *104*(B1), 1179–1192.

Zelt, B. C., R. M. Ellis, R. M. Clowes, and J. A. Hole (1996), Inversion of three-dimensional wide angle seimic data from the southwestern Canadian Cordillera, *J. Geophys. Res.*, *286*, 209–221.

Zelt, B. C., R. M. Ellis, C. A. Zelt, R. D. Hyndman, C. Lowe, G. D. Spence, and M. A. Fisher (2001), Three-dimensional crustal velocity structure beneath the Strait of Georgia, British Columbia, *Geophy. J. Int.*, *144*, 695–712.

Zelt, C. A., and P. J. Barton (1998), Three-dimensional seismic refraction tomography: A comparison of two methods applied to data from the Faeroe Basin, *J. Geophys. Res.*, *103*, 7187–7210.

Zelt, C. A., and R. B. Smith (1992), Seismic traveltime inversion for 2-D crustal velocity structure, *Geophy. J. Int.*, *108*, 16–34.

Zhao, D., K. Wang, G. C. Rogers, and S. M. Peacock (2001), Tomographic image of low P velocity anomalies above slab in northern Cascadia subduction zone, *Earth Planets Space*, *53*, 285–293.

Zühlsdorff, L., V. Spiess, C. Hübscher, and M. Breitzke (1999), Seismic reflectivity anomalies in sediments at the eastern flank of the Juan de Fuca Ridge: Evidence for fluid migration?, *J. Geophys. Res.*, *104*(B7), 15,351–15,364, doi:10.1029/1999JB900061.

Zykov, M. M. (2006), 3-D traveltime tomography of the gas hydrate area offshore Vancouver Island based on OBS data, Ph.D. thesis, University of Victoria.